Statistical Estimation of Phase Response Curves

Ken Nakae

DOCTOR OF PHILOSOPHY

Department of Statistical Science
School of Multidisciplinary Science
The Graduate University for Advanced Studies

2010 (School Year)

Abstract

Phase response curve (PRC) describes the response of an oscillator to external perturbation; it is useful to predict and understand synchronized dynamics of oscillators. In recent years, neuroscientists have focused on neurons' PRCs, and measured them experimentally. This originates from the leading hypotheses that the synchronization of neurons has a functional meaning in the brain.

In this thesis, we propose two statistical methods for estimating PRCs from data; it allows for the correlation of errors in explanatory and response variables of the PRC. This correlation is neglected in previous studies.

The first method is implemented with a replica exchange Monte Carlo technique; this avoids local minima and enables efficient calculation of posterior averages. A test with artificial data generated by noisy Morris-Lecar equations shows that, in terms of accuracy, this method outperforms conventional regression that ignores errors in the explanatory variable. Experimental data from the pyramidal cells in the rat motor cortex is also analyzed; a case is found where the result with the first method is considerably different from that obtained by conventional regression.

The second method is developed using a transformation that mixes the variables; it effectively removes the correlation. The computation time of this method is considerably less than that of the first method. The same test using the noisy Morris-Lecar equations shows that the second method also outperforms than convectional regression in terms of accuracy.

Acknowledgment

I am deeply grateful to my supervisor Associate Professor Yukito Iba. I would like to express my gratitude to Associate Professor Toshio Aoyagi, who was my supervisor of my master course in Kyoto University.

I am indebt to Professor Tomoyuki Higuchi and Professor Kenji Fukumizu whose comments made enormous contribution to this thesis. Professor Tomoki Fukai in RIKEN gave insightful comments, and encouraged me to apply the method in this thesis to experimental data. Dr. Tsubo Yasuhiro in RIKEN provided the experimental data. Discussion with him has been interesting for me.

I have had the encouragement of Professor Takashi Tsuchiya in National Graduate Institute for Policy Studies, Professor Satoshi Kuriki, Professor Hiroe Tsubaki and Associate Professor Genta Ueno in the Institute of Statistical Mathematics. Special thanks to Professor Nobuhisa Kashiwagi in the Institute of Statistical Mathematics and Assistant Professor Hayato Chiba in Kyushu University, who give important comments in my research.

I would like to express my gratitude to President Genshiro Kitagawa in the Research Organization of Information and Systems, Associate Professor Toshio Ohnishi in Kyushu University, Dr. Hai-Yen Siew in Meiji University, Professor Emeritus Yoshiaki Itoh, Associate Professor Yoichi Nishiyama, Assistant Professor Shogo Kato, Dr. Xiaoling Dou and Dr. Ushio Tanaka in the Institute of Statistical Mathematics. We had a talk in Indian Statistical Institute; this made me decide to be a researcher.

I want to thank my colleagues in Kyoto University and in the Graduate University for Advanced Studies. I especially thank my friends Dr. Keisuke Ota and Mr. Kaiichiro Ota, who and I often discuss my research. My heartfelt appreciation goes to my family, who support me in the doctor course.

This research was supported by an allocation of computing resources of HP XC4000 and Fujitsu PRIMERGY RX200S5 from the Institute of Statistical Mathematics.

Overview of this thesis

This thesis is divided into 3 parts and consists of 10 chapters. Part I (Chap. 1–4) provides the background and motivation of this thesis. In part II (Chap. 5–7), we propose a Bayesian method for estimating PRCs, where we consider a correlation between the explanatory and response variables. This method is implemented with replica exchange Monte Carlo methods. In part III (Chap. 8–10), we propose another statistical method, which also consider the correlation. A transformation that removes the correlation plays an essential role in this part. In Chap. 10, we summarize this thesis and discuss future problems.

The details of each part are as follows:

Part I In Chap. 1, we briefly discuss motivations of this thesis and concepts of synchronization and phase response curve. The detail of the concept is discussed in Chap. 2. In Chap. 3, we review methods for estimating PRCs including that proposed in my master thesis. We discuss drawbacks of these methods, and discuss our approach of this thesis. In Chap. 4, we briefly discuss a Bayesian framework used in this thesis, and introduce Metropolis-Hastings methods and replica exchange Monte Carlo methods used in part II.

Part II In Chap. 5, we derive a Bayesian model, which describes a correlation between errors in PRC explanatory and response variables. In Chap. 6, we propose a Bayesian method for estimating PRCs using replica exchange Monte Carlo methods. In Chap. 7, this proposed method is tested with artificial data generated by noisy Morris-Lecar equations. We compare the method with conventional regression in terms of accuracy for the data. We also analyze experimental data from the pyramidal cells in the rat motor cortex.

Part III In Chap. 8, we propose a statistical method using a data transformation that mixes the PRC explanatory and response variables. This method is based on a modification of the model in part II. In Chap. 9, the method in part III is compared with the method in II and conventional regression in terms of accuracy and computation time. In Chap. 10, summary and future problems are presented.

Contents

I Background and motivation **13**

1 Introduction **15**

1.1 Synchronization . . . 15
1.2 Phase response curves and coupled phase oscillators . . . 17
1.3 Phase response curves in neuroscience . . . 23
1.4 Motivation of this thesis . . . 25

2 Theory of synchronization **29**

2.1 Coupled phase oscillators . . . 29
  2.1.1 Phase reduction and averaging of interacting nonlinear oscillators . 29
  2.1.2 Analysis of two coupled phase oscillators . . . 31
2.2 Application in neuroscience . . . 32
  2.2.1 Mathematical model of neuron and synaptic transmission . . . 32
  2.2.2 Coupling function between neurons . . . 34
  2.2.3 Type-I and Type-II phase response curves . . . 36
  2.2.4 Usages of phase response curves in neuroscience . . . 37

3 Estimation of phase response curves **39**

3.1 Measurement of phase response curves . . . 39
3.2 Previous studies . . . 40
3.3 Measurement error model . . . 43
3.4 Characteristics of errors in the data . . . 43
3.5 Our Approach . . . 44

4 Bayesian estimation and Markov chain Monte Carlo methods 47

4.1 Bayesian framework 47

4.2 Markov chain Monte Carlo methods 48

4.2.1 Metropolis-Hastings method 48

4.2.2 Replica exchange Monte Carlo method 49

II Bayesian estimation of phase response curves using replica exchange Monte Carlo methods 53

5 Bayesian model of phase response curves 55

5.1 Introduction 55

5.2 Derivation of the model 56

5.3 Bayesian model in part II 59

6 Estimation of the model using MCMC methods 67

6.1 Basic Markov chain Monte Carlo method 67

6.2 Extension to replica exchange methods 70

6.3 Estimation of hyperparameters 74

7 Numerical experiments and analysis of experimental data 77

7.1 Numerical experiments 77

7.1.1 Examples 77

7.1.2 Statistical comparison using average L^2 error 82

7.1.3 Detail analysis with L^2 errors 83

7.2 Analysis of experimental data 87

7.2.1 Experimental data 87

7.2.2 Analysis of synchronization property 91

III Statistical estimation of phase response curves using data transformation 95

8 Estimation using data transformation 97

8.1 Introduction 97

8.2 Statistical model in part III 98
8.3 Rough sketch of the estimation using data transformation 99
8.4 Details of the estimation using the data transformation 100
8.5 Estimation of the transformed phase response curve 101
8.6 Choice of the tuning parameters λ,$\bar{\tau}$ and ζ 102

9 Numerical experiment 103
9.1 Examples 103
9.2 Statistical comparison using average L^2 error 107
9.3 Detail analysis with L^2 errors 107
    9.3.1 Comparison to conventional regressions 107
    9.3.2 Comparison to method in part II 112
9.4 Computation time 115
9.5 On the choice of hyperparameters 116

10 Summary and future problems 119
10.1 Summary 119
10.2 Future problems 120

A Bayesian regression with a boundary condition 123

B Conductance based neuron models 127
B.1 Morris-Lecar equations 127
B.2 Hodgkin-Huxley equations 128

Part I

Background and motivation

Chapter 1

Introduction

1.1 Synchronization

Synchronization is observed everywhere in nature [Pikovsky et al., 2002, Strogatz, 2004]. For example, beating of the heart is a result of the synchronization of the cell activities of the heart muscles [Reemtsen and Rueckmann, 1983]. Fireflies in an area of Southeast Asia flash periodically and simultaneously [Smith, 1935, Buck and Buck, 1968, Ermentrout and Rinzel, 1984], which is first reported by E. Kaempfer in 18-th century. Synchronizations are also observed in chirps of the snowy tree crickets [Walker, 1969] and in croaking of the neighboring two tree frogs [Aihara et al., 2007, Aihara, 2009]. We encounter synchronization phenomena in biology [Aschoff et al., 1982, Dano et al., 1999, Elowitz and Leibler, 2000], in chemistry [Toth et al., 2006, Mikhailov and Showalter, 2006], and in physics [Simonet et al., 1994, Pantaleone, 2002, Eckhardt et al., 2007, Kitahata et al., 2009].

In the brain, we also observe synchronization between neurons and its result [Salinas and Sejnowski, 2001, Varela et al., 2001]. For example, gamma frequency oscillations observed in the local field potential of the mammalian olfactory bulbs is considered to be the result of synchronous activities of the neurons [Adrian, 1950, Freeman, 1972, Schoppa, 2006]. A periodic activity of electroencephalogram is also the result of the synchronization [Eccles, 1951, Singer, 1999, Whittingstall and Logothetis, 2009]. Epilepsy is caused by an abnormal synchronization between neurons [Engel et al., 2007, Lehnertz et al., 2009]. In these examples, oscillatory phenomena are often observed as the result of the synchronization of neurons.

In recent years, we have directly observed the synchronization between neurons because of the developments of systems for recoding the neural population [Nicolelis et al., 1999]. For example, activities of neurons are measured by multi electrodes systems [Thomas et al., 1972, Taketani et al., 2006], calcium imaging [Grynkiewicz et al., 1985, Stosiek et al., 2003], and voltage sensitive dye imaging [Cohen and Salzberg, 1978, Zochowski et al., 2000] of the neurons. Using them, the synchronization are experimentally detected in various areas of the brain: for example, motor cortex [Riehle et al., 1997, Baker et al., 2001], somatosensory cortex [Steinmetz et al., 2000, Roy et al., 2001], visual cortex [Fries et al., 2001, Freiwald et al., 2001] and basal ganglia [Goldberg et al., 2004].

Neuroscientists have been focusing functions of synchronization in the brain [Buzsáki, 2006]. This is because some hypotheses are proposed that the synchronization is essential for understanding information processing of the brain [Malsburg and Schneider, 1986, Gray and Singer, 1989, Fries, 2005, Engel et al., 2001, Hopfield and Brody, 2001, Aoki and Aoyagi, 2007]. These hypotheses argue that coherence in neural activities induced by synchronization is not a side effect but essential for understanding brain functions.

Here, we briefly explain one of the hypotheses proposed by Malsburg and Schneider [1986] that the synchronization is closely related to the "binding problem" of cognitive neuroscience. To understand the binding problem and the hypothesis, we present an example where a person looks a brown disc as shown in Fig. 1.1. According to the studies in neuroscience [Gazzaniga, 2004], it is known that the information of the shape and the color of the disc is distributed in different regions in visual cortex of the brain. Through an unknown information processing, the person bind the information of the shape and the color, and recognize "This is a brown disc". In this example, the binding problem is a question: What is the unknown information processing? Gray and Singer [1989] try to answer the question through the hypothesis that binding of information occurs because of the synchronizations between the spikes of neurons in the corresponding areas. Many researchers have tried to investigate the binding problem and this hypothesis from various aspects [Revonsuo and Newman, 1999, Thiele and Stoner, 2003, Bartels and Zeki, 2006, Dong et al., 2008].

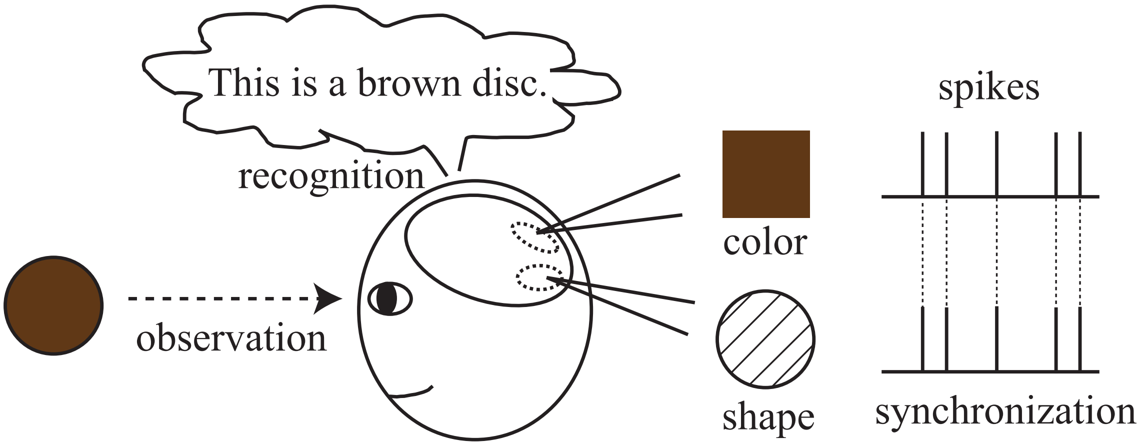

Figure 1.1: A example of the binding problem and the hypothesis proposed by Malsburg and Schneider [1986].

1.2 Phase response curves and coupled phase oscillators

Phase response curves

To deal with synchronization from the theoretical viewpoint, Kuramoto [1984] developed a theory based on phase reduction from interacting nonlinear oscillators to "coupled phase oscillators"; see also [Malkin, 1949, 1959, Winfree, 1967, 2001, Kopell and Ermentrout, 1990, Hansel et al., 1995, Ermentrout, 1996, Izhikevich, 2007, Kuramoto and Kawamura, 2010] and recent surveys [Strogatz, 2000, Acebron et al., 2005]. A key concept of this theory is a phase response curve (PRC), which describes the response of an isolated oscillator to external perturbations. The PRCs are usually defined from the viewpoint of the dynamical systems; here, we assume that the oscillator has a stable limit cycle. This means that no closed orbit exists near the limit cycle, and it attracts all neighboring trajectories.

Here, we explain an definition of the PRCs, where we assume a d-dimensional dynamical system $\mathbf{u}(t)$ has a stable limit cycle C as shown in the upper-left panel of Fig. 1.2. The procedure consists of the following three steps:

1. We define a smooth and bijective function on the limit cycle $\psi : C \to S^1$, which corresponds to a phase variable from 0 to 2π of the oscillator, as shown in the upper-left panel.

2. Under regularity conditions [Coddington and Levinson, 1955, Guckenheimer, 1975], the domain of ψ is appropriately [1] extended to a neighborhood $N(C)$ of the limit cycle; i.e. the extended function $\psi^e : N(C) \to S^1$ satisfies $\psi^e|_C = \psi$. The $d-1$ dimensional manifold $I(\phi) = \{\mathbf{u} \in N(C) | \psi^e(\mathbf{u}) = \phi\}$ is called an isochron, which is shown as the curve of the upper-right panel.

3. Finally, we obtain the phase response curves (PRCs) $\mathbf{Z}(\phi) = \mathrm{grad}_{\mathbf{u}(\phi)\in C}\psi^e(\mathbf{u})$, which is a d-dimensional periodic vector function. The right side of this equation means a normal vector at $\mathbf{u}(\phi) := \psi^{-1}(\phi)$ on the isochron $I(\phi)$. The red arrows in the lower panel show the normal vectors.

The d-dimensional dynamics of the oscillator can be reduced to a one-dimensional dynamics of the phase variable ϕ where phase shifts by external perturbations are described by the PRCs. In this thesis, we call this reduction "phase reduction of the oscillator".

Another definition of phase response curves

Here, we explain an operational definition of the PRCs, which is more intuitive and useful for understanding experiments. Its correspondence to the definition based on phase description of the dynamical systems is explained in the next section.

We define PRC $\mathbf{Z}(\phi)$ of a nonlinear oscillator from an operational viewpoint. PRC $\mathbf{Z}(\phi) = (Z^{(1)}(\phi), \ldots, Z^{(d)}(\phi))$ is a periodic d-dimensional vector function in the domain $[0, 2\pi)$, when the dynamical system of the oscillator has d-dimensional state.

As an example of the nonlinear oscillator, we consider a neuron, whose activity is periodic. The state of the neuron has various components, which correspond to the activities of the voltage, the potassium channel, the sodium channel and so on. Here, we operationally define the voltage component of PRC $\mathbf{Z}(\phi)$; it is denoted by $Z(\phi)$. This is because other components of PRC can be defined in the same manner, and the voltage component of the PRC gives sufficient information to analyze the synchronization of neurons. The latter reason will be explained in Sec. 2.2

We assume that the activity of a neuron is periodic and the period is T. The solid curve in the left panel of Fig. 1.3 represents a time-series of the voltage for the neuron. We

---

[1] In an asymptotic sense ($t \to \infty$), we can identify a point $\mathbf{u}'$ on the limit cycle as points at which values of ψ^e are equal to the phase of the point $\mathbf{u}'$; the set of the identifiable points is an $d-1$-dimensional manifold "isochron", which is shown as the curves in the upper-right panel.

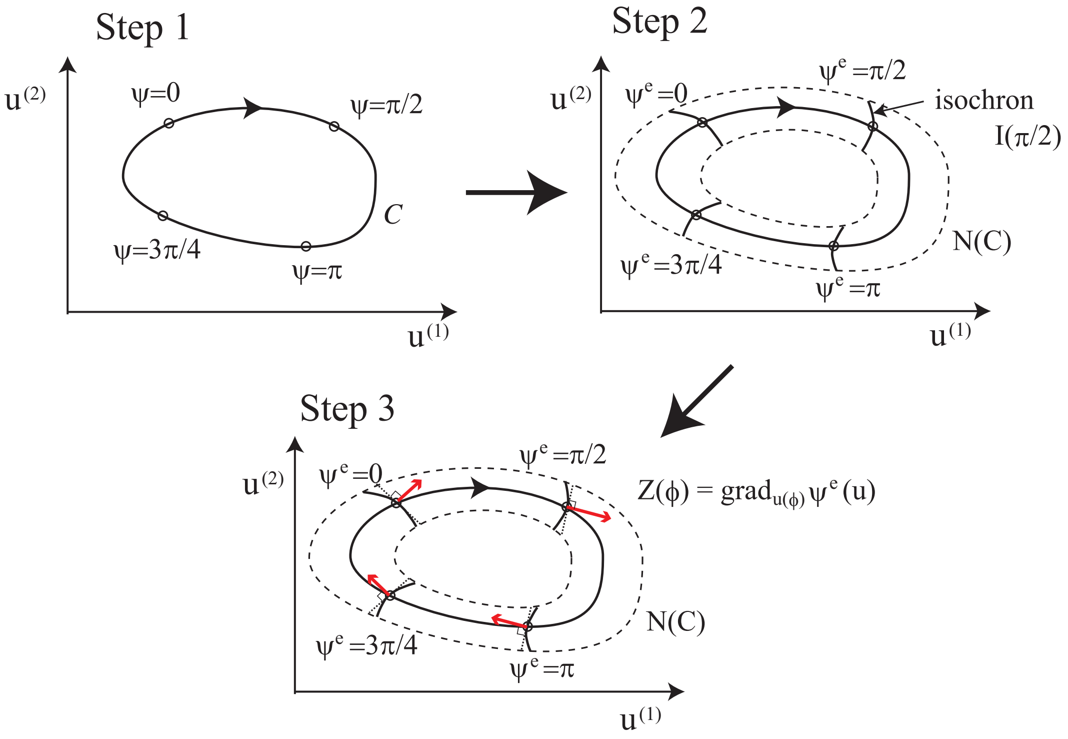
Step 1
u(2)
u(1)
ψ=0
ψ=π/2
ψ=3π/4
ψ=π
C
Step 2
u(2)
u(1)
ψe=0
ψe=π/2
isochron
I(π/2)
ψe=3π/4
ψe=π
N(C)
Step 3
u(2)
u(1)
ψe=0
ψe=π/2
Z(ϕ) = grad_u(ϕ) ψe(u)
ψe=3π/4
ψe=π
N(C)

Figure 1.2: Three steps of defining the PRCs of $d = 2$ dimensional dynamical system.

consider a set of trials indexed by i. The neuron is assumed to fire at the origin $t = 0$. For the ith trial, a perturbation is added at time $t = t_i$. The neuron then fires again at time $t = T'_i$ as shown by the dotted curve in the Fig. 1.3. We repeat this procedure a number of times and plot the points (ϕ_i, Z_i), $i = 1, \cdots, n$, defined by

$$\phi_i = 2\pi\frac{t_i}{T}, \qquad Z_i = 2\pi\frac{T - T'_i}{T}. \tag{1.1}$$

A smooth and periodic curve $Z(\phi)$ interpolating these points in the domain $[0, 2\pi)$ is the voltage component of the PRC of the neuron. The example of the curve is shown by the solid curve in the right panel of Fig. 1.3.

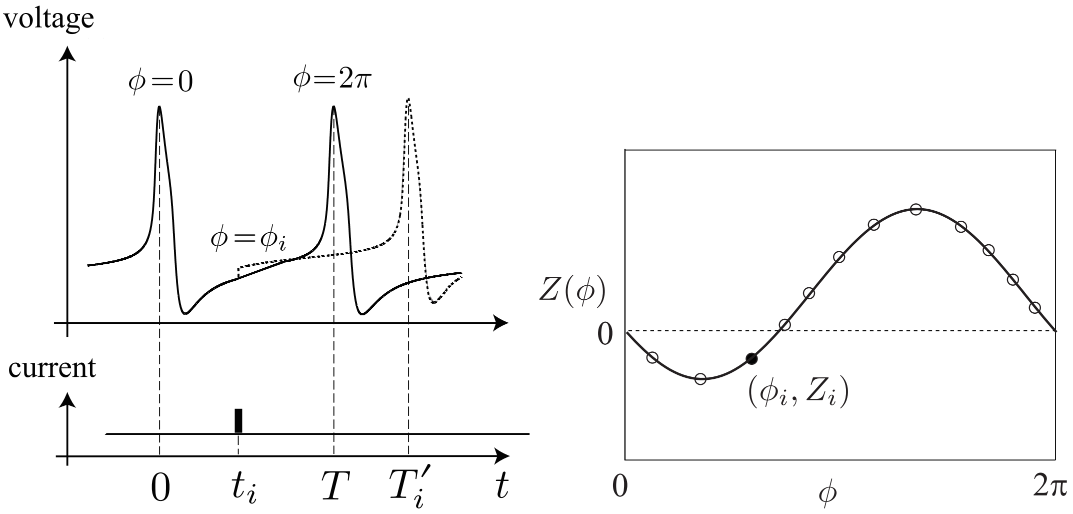

Figure 1.3: Measurement of a phase response curve. A trial with a perturbation at $t = t_i$ is illustrated in the left panel. The solid curve indicates the voltage for the neuron without perturbation, while the dotted curve indicates that with perturbation. Each point (ϕ_i, Z_i) in the right panel corresponds to a trial with timing t_i. PRC is defined by interpolating these points.

Connection to the definition through dynamical systems

In the previous section, we explain an operational definition of PRC of a nonlinear oscillator. Conventionally, the PRC is defined through phase reduction of the dynamical system of the oscillator. Here, we discuss a correspondence between two definitions of the PRC. Details of the phase reduction can be found in the book [Kuramoto, 1984].

Here, we revisit the phase reduction of the oscillator from the viewpoint of dynamical system. Let us represent the state of the oscillator by the vector $\mathbf{u} = (u^{(1)}, \ldots, u^{(d)}) \in \mathbb{R}^m$. An equation that describes dynamics of the oscillator is assumed as

$$\frac{d\mathbf{u}}{dt} = \mathbf{f}(\mathbf{u}) + \mathbf{p}(t), \tag{1.2}$$

where the vector field $\mathbf{f}(\mathbf{u})$ has a stable limit cycle C as shown in the left panel of Fig. 1.4. The vector $\mathbf{p}(t) = (p^{(1)}(t), \cdots, p^{(d)}(t))$ represents an external perturbation. When $\mathbf{f}(u)$ satisfies regular conditions [Coddington and Levinson, 1955, Guckenheimer, 1975] and

$\mathbf{p}(t)$ is sufficiently small, Eq. (1.2) is reduced to the dynamics

$$\frac{d\phi}{dt} = \omega + \mathbf{Z}(\phi) \cdot \mathbf{p}(t), \tag{1.3}$$

where the natural frequency ω is $2\pi/T$ and a point on C is indicated by the phase variable $\phi \in [0, 2\pi)$ [Kuramoto, 1984]. The smooth and periodic vector function $\mathbf{Z}(\phi) = (Z^{(1)}(\phi), \ldots, Z^{(d)}(\phi))$ represents a response of the oscillator to the perturbation $\mathbf{p}(t)$. As shown in Fig. 1.4, the dynamics of the state $\mathbf{u}(t)$ on the limit cycle C is reduced to the dynamics of the angle $\phi(t)$ of the unit circle. This reduction from Eq.(1.2) to Eq.(1.3) is called the phase reduction of the oscillator.

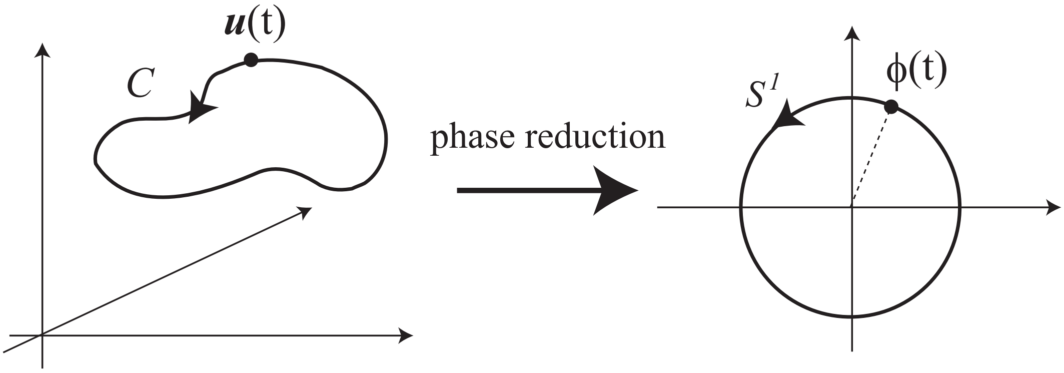

Figure 1.4: Phase reduction of a dynamical system that has a limit cycle C.

To show a correspondence to the operational definition, we assume that the first component $u^{(1)}$ of the state is the voltage of the neuron discussed in the previous section. When the perturbation $\mathbf{p}(t)$ is added to the first component $u^{(1)}$ only and the functional form of $p^{(1)}(t)$ is the Dirac's delta function $\delta(t - t_i)$, Eqs. (1.2) and (1.3) correspond to the experiment defining PRC $Z(\phi)$ from the operational viewpoint. Thus, we can identify the function $Z^{(1)}(\phi)$ in Eq. (1.3) with a PRC $Z(\phi)$ defined operationally. This can be seen by integrating Eq. (1.3) in the regions $[0, t_i)$ and $[0, T_i)$. As a result, we derive the two equations

$$\phi(t_i) = 2\pi\frac{t_i}{T}, \qquad Z^{(1)}(\phi(t_i)) = 2\pi\frac{T - T_i'}{T}, \tag{1.4}$$

which correspond the left and right equations in Eq. (1.1) respectively.

Coupled phase oscillators

In the theory developed by Kuramoto [1984], we deal with synchronization of the dynamics of N interacting nonlinear oscillators. Phase reduction of each oscillator reduces the $N \times d$-dimensional dynamics of all oscillators to that of N-dimensional dynamics of their phase variables as shown in the left and middle panels of Fig. 1.5.

Coupled phase oscillators are defined through averaging of the interactions and the PRCs in this N-dimensional dynamical system; the average is considered as an effective interaction called a coupling function. Coupled phase oscillators provide a concise description of the original interacting nonlinear oscillators. In Fig. 1.5, we illustrate the above procedure that derives the coupled phase oscillators. Details of the procedure are explained in Chap. 2.

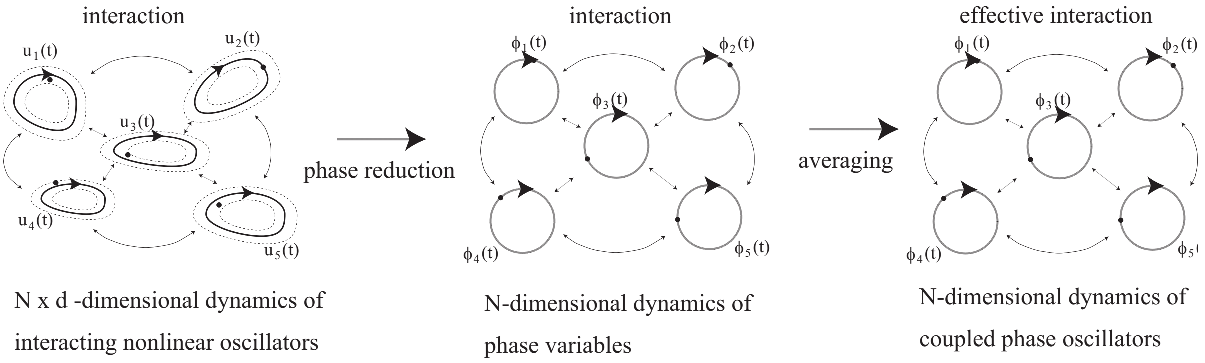
interaction
u1(t)
u2(t)
u3(t)
u4(t)
u5(t)
phase reduction
interaction
ϕ1(t)
ϕ2(t)
ϕ3(t)
ϕ4(t)
ϕ5(t)
averaging
effective interaction
ϕ1(t)
ϕ2(t)
ϕ3(t)
ϕ4(t)
ϕ5
N x d -dimensional dynamics of interacting nonlinear oscillators
N-dimensional dynamics of phase variables
N-dimensional dynamics of coupled phase oscillators

Figure 1.5: Phase reduction from interacting nonlinear oscillators to coupled phase oscillators.

From a viewpoint of statistical physics, Kuramoto [1975] studied coupled phase oscillators (Kuramoto model) where all coupling functions are the same sine function, and natural frequencies of the oscillators follow a Cauchy distribution. Using an analytical technique, he found a transition from synchrony to asynchrony state of the coupled phase oscillators when $N \to \infty$. Being motivated by this study, many researcher investigate synchronization properties of various types of coupled phase oscillators and dynamics of coupled phase oscillators [Hansel et al., 1993, Kori and Kuramoto, 2001, Strogatz and Mirollo, 1991, Daido, 1994, 1996, Crawford, 1995, Sakaguchi et al., 1987, Hong et al., 2005, Ichinomiya, 2004, Kuramoto and Battogtokh, 2002].

These theoretical results refresh scientists for studying synchronization phenomena in biology [Aihara et al., 2007, Aihara, 2009], chemistry [Kiss et al., 2002, Zhai et al., 2004] and physics [Wiesenfeld et al., 1996, Strogatz et al., 2005]. They apply this theory to these phenomena and obtain successful results.

1.3 Phase response curves in neuroscience

Theoretical results

Here, we briefly discuss theoretical results about PRCs of neurons in this section, and show experimental data of the PRCs in the next section.

The PRCs $\mathbf{Z}(\phi)$ of a neuron have many components. For example, Hodgkin-Huxley equations [Hodgkin and Huxley, 1952], which is widely used for a mathematical neuron model, are described as a four-dimensional dynamical system; the components of the state are denoted by the activities of the voltage v, the potassium channel n, and the sodium channel m, h (the details are explained in Appendix. B). Thus, the PRCs has four corresponding components $Z_v(\phi), Z_n(\phi), Z_m(\phi)$ and $Z_h(\phi)$ as shown in the upper-left, upper-right, lower-left and lower-right panels of Fig. 1.6, respectively.

Many neuroscientists discuss only a voltage component of the PRCs of a neuron. This is because the voltage component $Z_v(\phi)$ of the PRCs gives sufficient information to analyze the synchronization of neurons, as we discuss in Sec. 2.2. This means that the component $Z_v(\phi)$ is an essential representation of the dynamics of the neuron; hereafter, we call it the PRC $Z(\phi)$ of the neuron.

From theoretical viewpoints, synchronization properties of neurons can be predicted using their PRCs $Z(\phi)$. According to the study by Hansel et al. [1995], two types of PRCs of neurons are classified:

1. For *all* phases $\phi \in [0, 2\pi)$, the value of the PRC $Z(\phi)$ is positive as shown in the left panel of Fig. 1.7; it is called a type-I PRC.

2. For *a* phase $\phi \in [0, 2\pi)$, the value of the PRC is negative as shown in the right panel of Fig. 1.7; it is called a type-II PRC.

They conclude that neurons which have type-II PRCs are easier to synchronize than neurons which have type-I PRCs. This result is supported by these successive studies [Nomura and

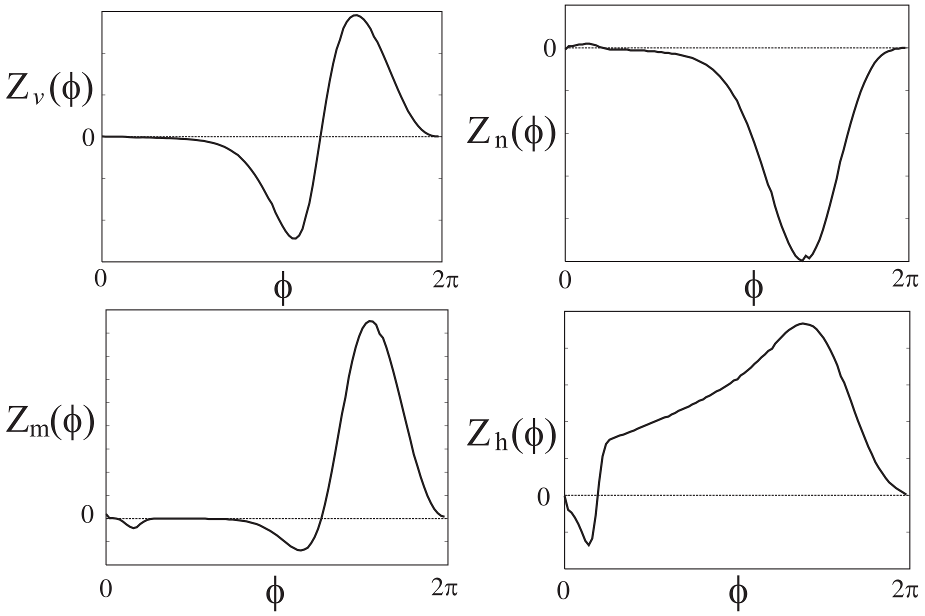

Figure 1.6: PRCs of Hodgkin-Huxley equations.

Aoyagi, 2005, Galán et al., 2007a,b, Marella and Ermentrout, 2008, Abouzeid and Ermentrout, 2009]. Based on the classification Tsubo et al. [2007b] predict the synchronization properties of neurons in rat motor cortex using the PRCs estimated from experimental data. This analysis shows that activities of neurons in the layer II/III of the cortex are easier to synchronize than that in the layer V.

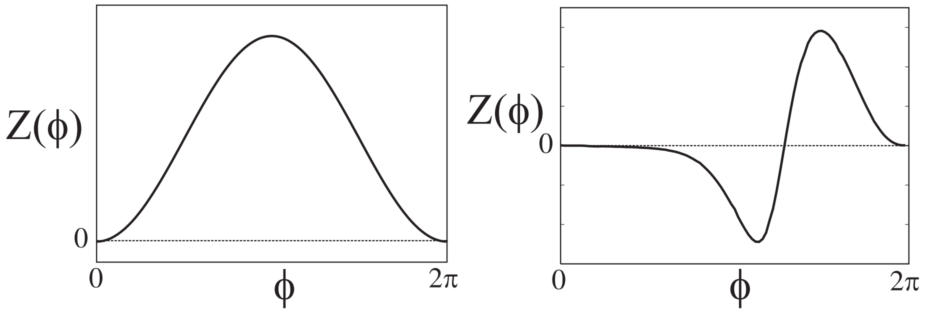

Figure 1.7: Type-I and Type-II PRCs.

PRCs are useful for not only predicting but also understanding synchronization phenomena in neural populations. For example, experimental results by Mainen and Sejnowski [1995] indicates that neurons synchronize when common noises input to them. Such a “noise induced synchronization” can be explained by the dynamical system based on the PRCs of neurons [Teramae and Fukai, 2008, Lin et al., 2009, García-Álvarez et al., 2009].

Experimental data

Many researchers have recently tried to estimate neuron’s PRC $Z(\phi)$ from experimental data in various areas of the brain [Reyes and Fetz, 1993a,b, Dorval et al., 2001, Oprisan et al., 2003, 2004, Galán et al., 2005, Gutkin et al., 2005, Lengyel et al., 2005, Netoff et al., 2005a,b, Preyer and Butera, 2005, Ermentrout and Saunders, 2006, Ermentrout et al., 2007, Goldberg et al., 2007, Mancilla et al., 2007, Tateno and Robinson, 2007, Tsubo et al., 2007a, Ota et al., 2009a, Ota, 2010, Phoka et al., 2010]. In Fig. 1.8, we present some examples of the data (the black or colored points) and the estimated PRCs (the black or colored curve). The data in the upper-left and upper-right panels are measured by neurons in rat somatosensory cortex [Tateno and Robinson, 2007] and in the abdominal ganglia of Aplysia californica [Preyer and Butera, 2005], respectively. The data in the lower-left and lower-right panels are measured by neurons in rat neocortex [Goldberg et al., 2007] and in rat motor cortex [Tsubo et al., 2007a], respectively.

In these examples, a sample (x, y) is obtained by adding an external perturbation to a neuron. The explanatory variable x correspond to timing of the perturbation. The response variable y corresponds the difference between neuron’s period and the inter-spike interval when adding the perturbation. Details of the experiments are explained in Chap. 3. Note that all PRCs of Fig. 1.8 are estimated using regression analysis where errors in the response variable are only considered.

1.4 Motivation of this thesis

As shown in these examples, noise in the PRC measurements is often very large, and sophisticated statistical techniques are necessary for efficient estimation. In Chap. 3, we discuss the following two facts:

- A data point (x, y) whose value $x \geq 2\pi$ can exist in experiments.

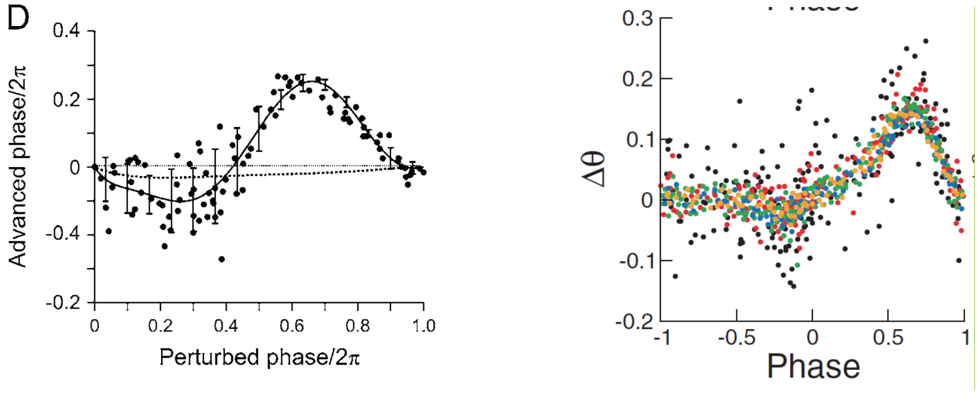

1) Tateno, et. al., 2007

2) Preyers, et. al., 2005

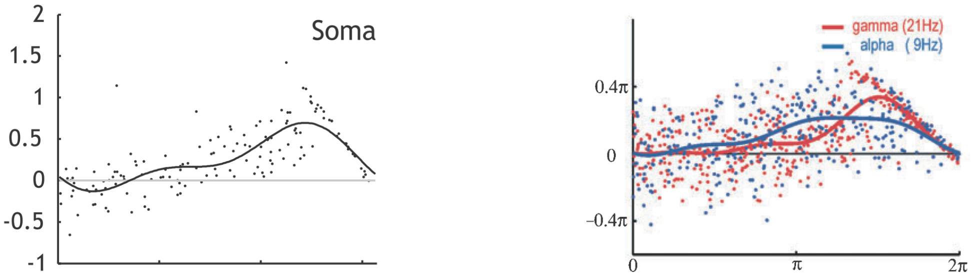

3) J.A. Goldberg, et. al., 2007.

4) Y. Tsubo, et. al., 2007

Figure 1.8: Experimental data (black or colored points) and estimated PRCs (black or colored curves).

- All data points are in the region $K = \{(x, y) \in \mathbb{R}^2 | x \geq 0, x + y \leq 2\pi\}$.

To see these facts, we present experimental data measured in rat motor cortex, which are shown as the points of Fig. 1.9; the data are provided by my coworkers Yasuhiro Tsubo. Actually, a data point (x, y) whose value $x \geq 2\pi$ exists, and all data points are in the region K shown as the mesh region of Fig. 1.9. In the conventional regression analysis, the data point whose value $x \geq 2\pi$ are neglected, because PRC is a periodic in the region $[0, 2\pi)$.

These facts can be explained by existences of the errors in the PRC explanatory variables and the correlation between errors in the explanatory and response variables, which are discussed in Chap. 3. The role of errors in explanatory variables for regression has been considered in the literature on statistics [Amari and Kawanabe, 1997, Cheng and Ness,

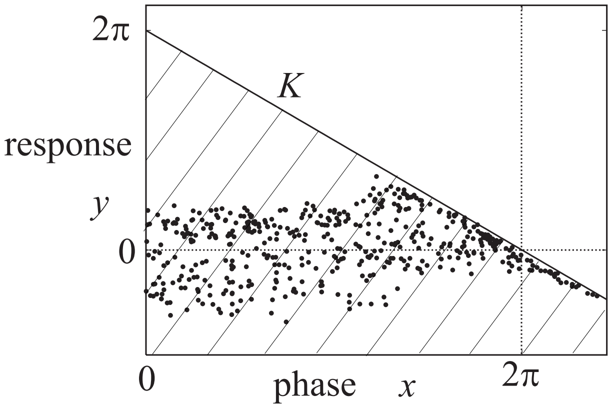

Figure 1.9: Experimental data and the region $K = \{(x, y) \in \mathbb{R}^2 | x \geq 0, x + y \leq 2\pi\}$.

1999, Berry et al., 2002, Fuller, 2006, Caroll et al., 2006]. The correlation between errors in the explanatory and response variables is also treated in some textbooks, for example, [Cheng and Ness, 1999], but it seems a less known subject; its appearance in the present problem of estimating PRCs will be interesting in terms of statistical science.

This study is devoted to developing two new methods that can deal with these errors and the correlation. In part II, we propose a Bayesian model accounting for them, and estimate PRCs using replica exchange Monte Carlo methods [Hukushima and Nemoto, 1996, Geyer and Thompson, 1995, Iba, 2001]. In part III, the correlation is effectively removed using a transformation that mixes the explanatory and response variables.

Using the proposed methods, we successfully improved the estimation precision for PRCs in examples of simulated data. The method proposed in part II is also applied to experimental data from the pyramidal cells in rat motor cortex.

The proposed methods for PRC estimation are useful for any kind of nonlinear oscillator that permits the phase description. Although our current interest is in applications for brain science, the method can also be used in other fields of biology, chemistry, and physics.

Chapter 2

Theory of synchronization

Kuramoto [1984] developed a theory based on collective dynamics of interacting nonlinear oscillators; it explains various examples of the synchronization phenomena. In this chapter, we explain this theory and its application in neuroscience. We first explain dynamics of coupled phase oscillators and analyze the synchronicity of two coupled phase oscillators in Sec. 2.1. An application of the theory to neuroscience discussed in Sec. 2.2.

2.1 Coupled phase oscillators

2.1.1 Phase reduction and averaging of interacting nonlinear oscillators

Coupled phase oscillators are derived from interacting nonlinear oscillators by applying the phase reduction and an averaging technique. Here, the dynamics of the N interacting nonlinear oscillators are given by

$$\frac{d\mathbf{u}_k}{dt} = \mathbf{f}_0(\mathbf{u}_k) + \delta\mathbf{f}_k(\mathbf{u}_k) + \sum_{l=1}^{N} \mathbf{V}_{kl}(\mathbf{u}_k, \mathbf{u}_l), \qquad k = 1, \dots, N, \tag{2.1}$$

where the d-dimensional state of the k-th oscillator is represented by the vector $\mathbf{u}_k = (u_k^{(1)}, \dots, u_k^{(d)})$. The vector filed of the k-th oscillator is represented by $\mathbf{f}_0(\mathbf{u}_k) + \delta\mathbf{f}_k(\mathbf{u}_k)$, which has a limit cycle whose natural frequency is ω_k. The effect from the k-th oscillator to the l-th oscillator is represented by $\mathbf{V}_{kl}(\mathbf{u}_k, \mathbf{u}_l)$.

Here, the vector field $\mathbf{f}_0(\mathbf{u})$ also has a limit cycle C_0 and the natural frequency is ω_0. The solution on the limit cycle C_0 derived from the vector filed $\mathbf{f}_0(\mathbf{u})$ is represented by $\mathbf{u}_0(t)$. Since the vector filed $\delta\mathbf{f}_k(\mathbf{u})$ denotes a small perturbation, we obtain $(\omega_k - \omega_0)/\omega_0 \ll 1$.

Using the phase reduction of each oscillator, Eq.(2.1) can be reduced to

$$\frac{d\phi_k}{dt} = \omega_k + \mathbf{Z}_k(\phi_k) \cdot \sum_{l=1}^{N} \mathbf{V}_{kl}(\mathbf{u}_0^*(\phi_k), \mathbf{u}_0^*(\phi_l)), \qquad k = 1, \ldots, N, \tag{2.2}$$

where $\mathbf{u}_0^*(\theta) = \mathbf{u}_0(\theta/\omega_0)$. Note that the vector filed $\mathbf{f}_0(\mathbf{u}_k) + \delta\mathbf{f}_k(\mathbf{u}_k)$ satisfies the regularity conditions and the interaction $\mathbf{V}_{kl}(\mathbf{u}_k, \mathbf{u}_l)$ are sufficiently small for all k and l. As Eq. (1.2) in the previous section, a point on the limit cycle of the k-th oscillator is denoted by $\phi_k \in [0, 2\pi)$.

Here, we define a new variable $\psi_k = \phi_k - \omega_0 t$ for all $k = 1, \ldots, N$. Using the variables $\{\psi_k\}$, Eq. (2.2) can be written as

$$\frac{d\psi_k}{dt} = (\omega_k - \omega_0) + \mathbf{Z}_k(\psi_k + \omega_0 t) \cdot \sum_{l=1}^{N} \mathbf{V}_{kl}(\mathbf{u}_0^*(\psi_k + \omega_0 t), \mathbf{u}_0^*(\psi_l + \omega_0 t)). \tag{2.3}$$

Since $(\omega_k - \omega_0)/\omega_0 \ll 1$ and $|\mathbf{V}_{kl}| \ll 1$, both term in the right side of Eq. (2.3) are sufficiently small; i.e. the dynamics of ψ_k is "slower" than that of ϕ_k. Thus, we approximate the right side by a time average of the right side from $t = 0$ to $t = T$. We call this procedure "averaging" of Eq.(2.2).

Finally, we obtain the dynamics of coupled phase oscillators

$$\frac{d\phi_k}{dt} = \omega_k + \sum_{l=1}^{N} \Gamma_{kl}(\phi_k - \phi_l), \qquad k = 1, \ldots, N, \tag{2.4}$$

$$\Gamma_{kl}(\phi) = \frac{1}{2\pi} \int_0^{2\pi} \mathbf{Z}_k(\theta) \cdot \mathbf{V}_{kl}(\mathbf{u}_0^*(\theta), \mathbf{u}_0^*(\theta + \phi)) d\theta. \tag{2.5}$$

where we restore the original variables $\{\phi_k\}$. The function $\Gamma_{kl}(\phi)$ is called coupling function. Based on the coupled phase oscillator defined by Eq.(2.4), we can explore the synchronization more easily than that based on the interacting nonlinear oscillators defined by Eq.(2.1).

2.1.2 Analysis of two coupled phase oscillators

Here, we discuss synchronization properties of two coupled phase oscillators, where the natural frequencies are equal ($\omega_1 = \omega_2$) and the coupling functions between the two oscillators are symmetric ($\Gamma_{12}(\phi) = \Gamma_{21}(\phi) = \Gamma(\phi)$). We illustrated this coupled phase oscillators in Fig. 2.1.

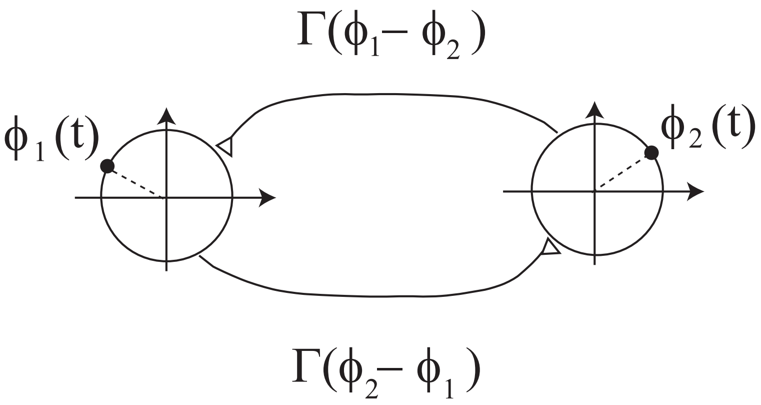

Figure 2.1: Two coupled phase oscillators.

The dynamics of the phase difference between the oscillators $\Delta\phi = \phi_1 - \phi_2$ is represented by

$$\frac{d\Delta\phi}{dt} = \Gamma^{-}(\Delta\phi), \tag{2.6}$$

where $\Gamma^{-}(\phi) = \Gamma_{12}(\phi) - \Gamma_{12}(-\phi)$. Equilibrium point $\Delta\phi_e$ satisfies $\Gamma^{-}(\Delta\phi_e) = 0$. When the derivative of $\Gamma^{-}(\phi)$ at $\phi = \Delta\phi_e$ is negative, the equilibrium point is stable. In Eq. (2.6), the points $\Delta\phi = 0$ and π are equilibrium points, because the function $\Gamma^{-}(\phi)$ is periodic and odd. We show three types of the functions $\Gamma^{-}(\phi)$ in Fig. 2.2. The solid curve represents the function $\Gamma^{-}(\phi)$, the point denotes the stable point, and the circle means the unstable point. The upper left and upper right panels indicate a in-phase and an anti-phase synchronization of the two oscillators, respectively. On the other hand, two oscillators are synchronized with a phase shift in $[0, 2\pi)$ in case of the lower panel. This type of synchronization is called out-of-phase synchronization.

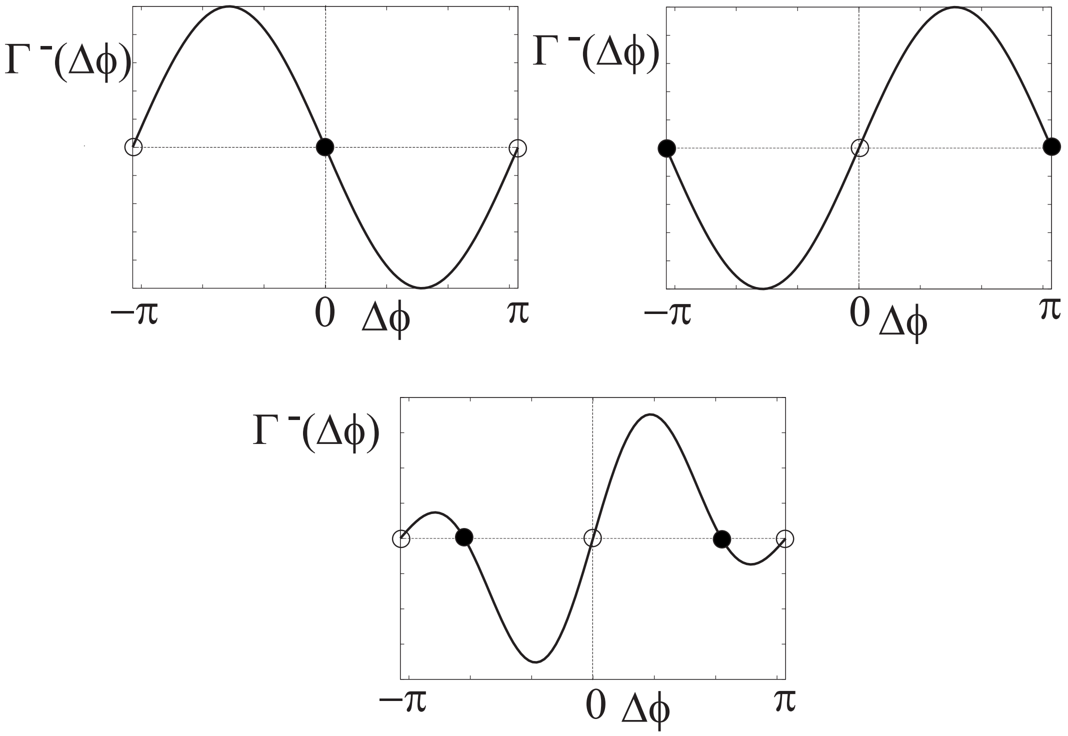

Figure 2.2: Equilibrium points and their stabilities. The solid curve indicate the functions $\Gamma^{-}(\phi) = \Gamma(\phi) - \Gamma(-\phi)$ and its zero-crossing means the equilibrium point of Eq.(2.6). The point and the circle shows that the equilibrium points are stable and unstable, respectively. Two symmetric connected oscillators are synchronized at in-phase, anti-phase and out-of-phase as shown in the upper-left panel, the upper-right panel and the lower panel, respectively.

2.2 Application in neuroscience

2.2.1 Mathematical model of neuron and synaptic transmission

To apply this theory to neuroscience, we discuss a system given by two neurons, which is synaptically inputted from neuron B to neuron A as shown in Fig. 2.3. Here, we assume that activities of both neurons are represented by the same nonlinear oscillator. Thus, the connected neurons can be considered as a example of coupled phase oscillators. In this section, we explain how to derive the coupling function $\Gamma(\phi)$ between the two neurons. The discussion in this section is easily extend to N synaptically connected neurons.

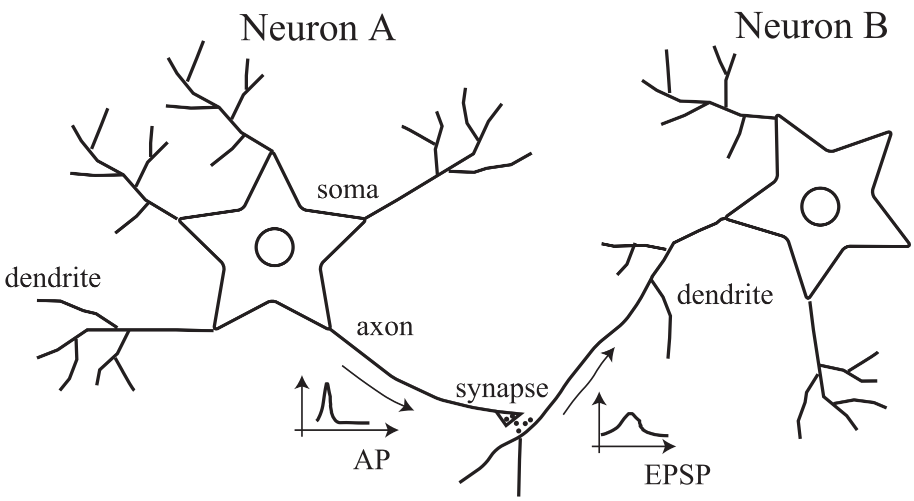

Figure 2.3: Synaptic connection from neuron A to neuron B.

For simplicity, neurons are assumed to be represented by conductance-based models [Koch and Schutter, 1999], which include Hodgkin-Huxley model [Hodgkin and Huxley, 1952] and Morris-Lecar model [Morris and Lecar, 1981]. The dynamics of neuron B connected from neuron A is described by the equations for the membrane potential v and the activities of ionic channels $u^{(1)}, \ldots, u^{(d-1)}$:

$$c\frac{dv}{dt} = \sum_{i=1}^{d-1} g_i(u^{(i)})(v - v_i) + i_{\text{ext}} + i_{\text{syn}}, \tag{2.7}$$

$$\frac{du^{(j)}}{dt} = f^{(j)}(v, u^{(1)}, \ldots, u^{(d-1)}), \qquad j = 1, \ldots, d-1, \tag{2.8}$$

where c is the membrane capacitance, g_i is the voltage-dependent conductance of the i-th ionic current, and v_i is its reversal potential. The current i_{ext} represents external inputs besides that from neuron A. The synaptic current i_{syn} from neuron A is usually modeled as

$$i_{\text{syn}} = -g_{\text{syn}}(v - v_{\text{syn}}) \sum_{j=0}^{N_{\text{pre}}} \alpha(t - t_j^{\text{spike}}), \tag{2.9}$$

where g_{syn} is the maximal synaptic conductance and v_{syn} is the reversal potential of the synapse. The summation in Eq. (2.9) means the total effect of all the spikes from neuron A, where t_j^{spike} is the timing of each spike, and N_{pre} is the number of the spikes. The function $\alpha(t)$, which is called alpha function, is defined by

$$\alpha(t) = \begin{cases} \frac{t}{\tau} \exp\left\{-\frac{t-\tau}{\tau}\right\}, & t \geq 0, \\ 0, & t < 0. \end{cases} \tag{2.10}$$

In Eqs.(2.7) and (2.8), the interaction between the two neurons is represented by the synaptic current i_{syn}; i.e. we can assume the form of the interaction in Eq.(2.1) is $\mathbf{V}_{1,2} = (i_{\text{syn}}, 0, \ldots, 0)$. The dynamics of coupling oscillators defined by Eq.(2.4) are affected from the interaction $\mathbf{V}_{1,2}$ through the form of the inner product $\mathbf{V}_{1,2} \cdot \mathbf{Z}(\phi)$ in Eq.(2.5). Thus, all components without the voltage component $Z(\phi)$ of the PRC $\mathbf{Z}(\phi)$ can be neglected. This is why the voltage component $Z(\phi)$ of the PRC gives sufficient information to analyze the synchronization of neurons.

2.2.2 Coupling function between neurons

To compute the coupling function $\Gamma(\phi)$ between the two neurons, we assume that the summation in Eq.(2.9) is approximated as

$$\alpha_T(t) = \sum_{n=0}^{-\infty} \alpha(t - nT), \tag{2.11}$$

because the activity of neuron A is periodic and its period is T [Vreeswijk et al., 1994]. Using these two formulas

$$\sum_{n=0}^{\infty} r^n = \frac{1}{1-r}, \qquad \sum_{n=0}^{\infty} n r^n = \frac{r}{(1-r)^2}, \qquad |r| < 1, \tag{2.12}$$

the periodic function $\alpha_T(t)$ is expressed as

$$\alpha_T(t) = \frac{1}{\tau} \exp\left\{-\frac{t-\tau}{\tau}\right\} \frac{t(1 - e^{-T/\tau}) - Te^{-T/\tau}}{(1 - e^{-T/\tau})^2}. \tag{2.13}$$

The coupling function defined by Eq.(2.5) is

$$\Gamma(\phi) = \frac{1}{2\pi} \int_0^{2\pi} Z(\theta) \left\{ -g_{\mathrm{syn}} (v^*(\theta) - v_{\mathrm{syn}}) \alpha_T^*(\theta + \phi) \right\} d\theta, \tag{2.14}$$

,where $Z(\theta)$ is the voltage component of the PRC of neuron B, $v^*(\theta) = v(\theta/\omega_0)$, and $\alpha_T^*(\theta) = \alpha_T(\theta/\omega_0)$.

Here, we show the example of the computation of the coupling function $\Gamma(\phi)$, when neuron B is represented by Morris-Lecar equations. Using the operational definition in Sec. 1.2, the PRC of neuron B is derived as shown in the upper-left panel of Fig. 2.4. The normalized voltage $v^*(\phi)$ and the periodic function $\alpha_T^*(\phi)$ are shown in the upper-right and lower-left panels, respectively. By numerically integrating Eq.(2.14), the coupling function is computed as the lower-right panel.

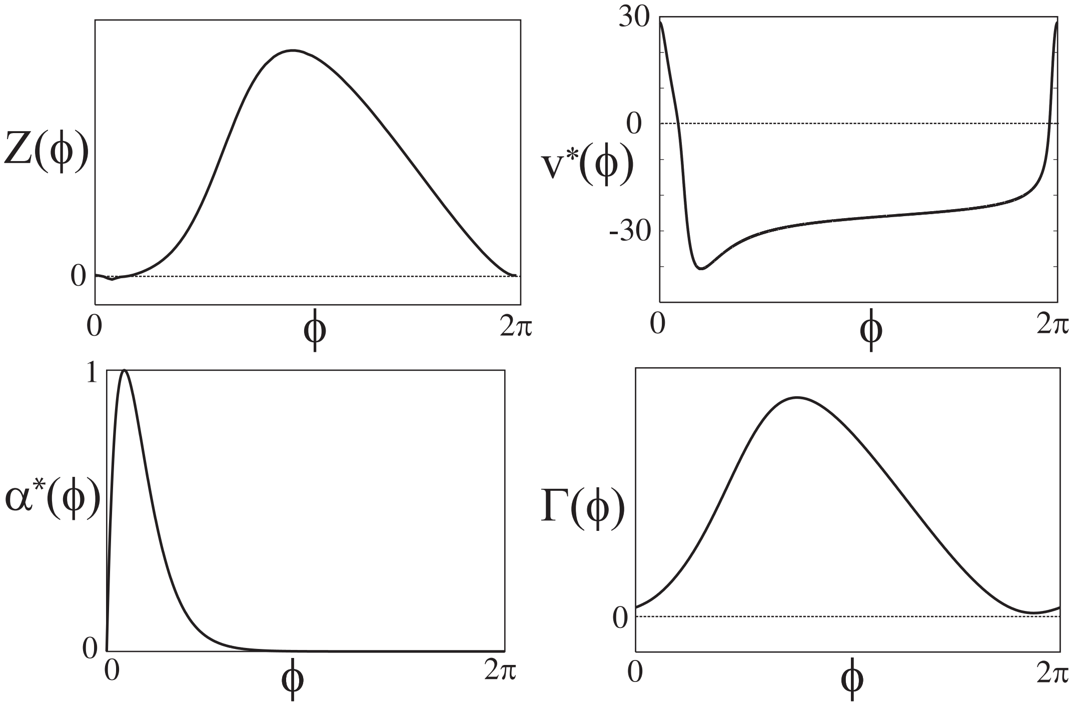

Figure 2.4: The voltage component $Z(\phi)$ of the PRC of Morris-Lecar equations is shown as the curve in the upper-left panel. The curves in the upper-right panel and the lower-left panel are the normalized voltage $v^*(\phi)$ and the function $\alpha^*(\phi)$, respectively. The coupling function $\Gamma(\phi)$ as shown in the lower-right panel is computed using the Eq. (2.14).

By using the function $\Gamma^-(\phi) = \Gamma(\phi) - \Gamma(-\phi)$, we can analyze the synchronization property of the two neurons as discussed in Sec. 2.1. Here, we assume neuron A and neuron B have the same PRCs and are symmetrically connected. When the coupling function is expressed as the lower-right panel in Fig. 2.4, the function $\Gamma^{-}(\Delta\phi)$ is shown in Fig. 2.5. The circle and the point in Fig. 2.5 represent the instability and the stability of equilibrium points of the phase difference $\Delta\phi = \phi_1 - \phi_2$ between the two neurons, respectively. Figure 2.5 shows that the two neurons are synchronized at anti-phase.

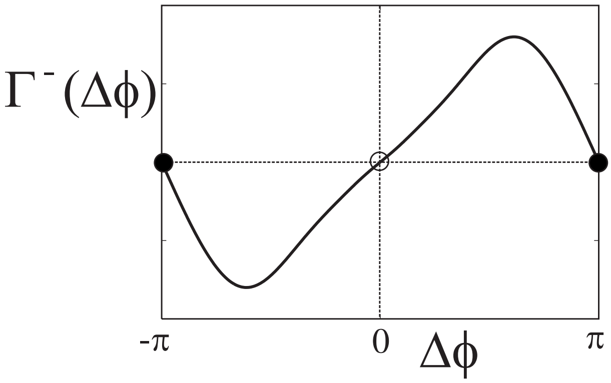

Figure 2.5: The function $\Gamma^{-}(\Delta\phi)$

2.2.3 Type-I and Type-II phase response curves

Using the function $\Gamma^{-}(\phi)$, Hansel et al. [1995], et al. discuss a synchronization property of two symmetrically connected neurons, whose periods and PRCs are the same. By their analysis, the following two types of PRCs are classified:

- in Type I, the value of the PRC $Z(\phi)$ is positive for all phases $\phi \in [0, 2\pi)$ as shown in the left panel of Fig. 2.6, whereas

- in Type II, the value of the PRC is negative for a phase as shown in the right panel of Fig. 2.6.

They conclude that the two neurons are *not* synchronized at in-phase, when the PRCs of the neurons are Type I.

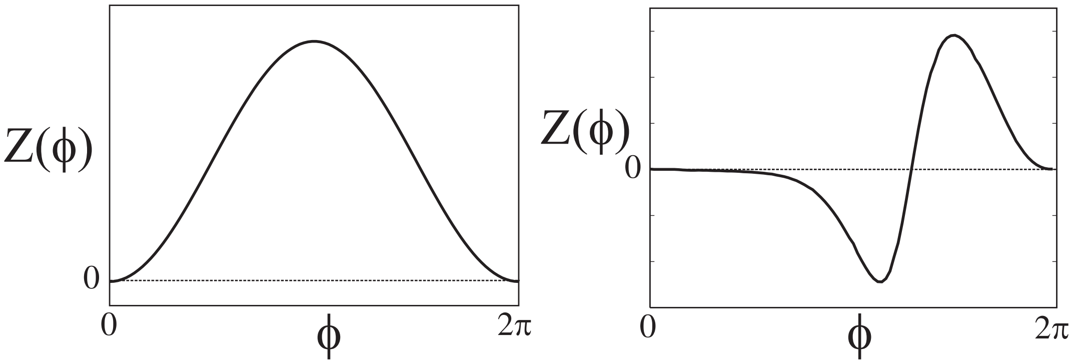

Figure 2.6: The Type-I and Type-II PRCs.

2.2.4 Usages of phase response curves in neuroscience

Here, we explain why PRCs are used in neuroscience. From the theoretical viewpoint, the dynamical system defined by Eq.(2.4) is easier for analyzing synchronizations than that defined by Eq.(2.1). Many mathematical models of a neuron are proposed to define the vector field $\mathbf{f}(\mathbf{u})$ in Eq.(1.2). For example, the leaky integrate-and-fire model [Koch and Schutter, 1999], Hodgkin-Huxley model [Hodgkin and Huxley, 1952], and Morris-Lecar equations [Morris and Lecar, 1981] are widely used in computational neuroscience. However, mathematical analysis based on the models is difficult, because the vector field $\mathbf{f}(\mathbf{u})$ is complicated (except for the leaky integrate-and-fire model). On the other hand, the dynamical system defined by Eq.(2.4) is usually simpler than the original dynamics. Actually, a lot of mathematical analysis is done based on Eq.(2.4) [Kuramoto, 1984, Tsubo et al., 2007a].

Moreover, computer simulations based on Eq.(2.4) are easier than that based on Eq.(2.1) [Galán et al., 2006], because the number of the dimension of the state $(\phi_1, \dots, \phi_N)$ in Eq.(2.4) is $1/d$ times of that of the state $(\mathbf{u}_1, \dots, \mathbf{u}_N)$ in Eq.(2.1).

Chapter 3

Estimation of phase response curves

3.1 Measurement of phase response curves

Measurements of PRCs are conventionally based on the operational definition of Sec. **??**. However, in experiments, inter-spike intervals fluctuate stochastically [Mainen and Sejnowski, 1995] as shown in the upper-left panel of Fig. 3.1. The period T in Eq. (1.1) is conventionally replaced by the average $\hat{T}$ of the inter-spike intervals. The data point (x_i, y_i) from the measurement is expressed as

$$x_i = 2\pi\frac{t_i}{\hat{T}}, \qquad y_i = 2\pi\frac{\hat{T} - T_i'}{\hat{T}} \qquad i = 1, \ldots, n. \tag{3.1}$$

The data points $\{(x_i, y_i)\}$ in the upper-right panel are generated with noisy Morris-Lecar equations explained in Appendix. B. The data in the lower panel are experimentally measured, which we discuss in Sec. 7.2.1. Note that the data point whose value $x_i \geq 2\pi$ exist in the example. This is one of key observations in this chapter.

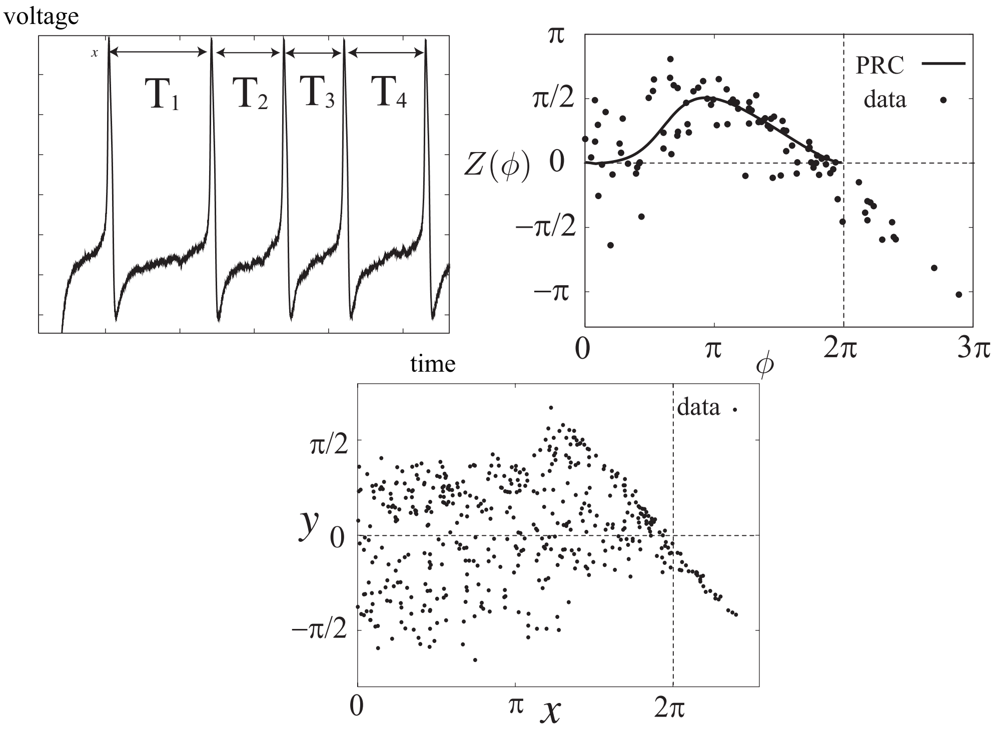

Figure 3.1: The left panel shows fluctuation of the periods. The ith inter-spike interval is denoted by T_i for $i = 1, 2, 3, 4$. Examples of the data is in the middle and right panels.

3.2 Previous studies

Fourier regression

In most existing studies, the PRC is estimated from the data $\{(x_i, y_i)\}$ in Sec. 3.1 based on the normal regression model

$$y_i = Z(x_i) + \varepsilon_i, \qquad \varepsilon_i \sim \mathcal{N}(0, \sigma^2), \qquad , i = 1, \ldots, n \tag{3.2}$$

where the error in the response variable is represented by ε_i, and the variance of the error is σ^2. In the regression model, the value x_i is assumed to be less than 2π, because the domain of the PRC is $[0, 2\pi)$. R. F. Galán and his collaborators [Galán et al., 2005] proposed a representation of the PRC $Z(\phi)$ as the finite Fourier series

$$Z(\phi) = \frac{a_0}{2} + \sum_{k=1}^{3} a_k \cos(k\phi) + b_k \sin(k\phi). \tag{3.3}$$

We call this method "Fourier regression" in this thesis. An example of the estimate is shown in Fig. 3.2, where the data points whose value $x_i \geq 2\pi$ are removed.

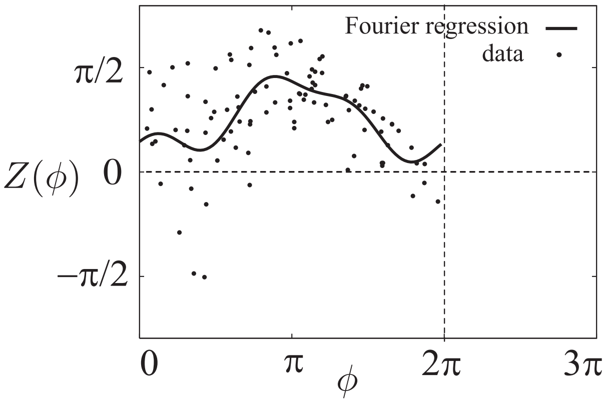

Figure 3.2: An example of the estimate obtained through Fourier regression

Spline regression

For estimating PRCs, Ke. Ota and his collaborators proposed a Bayesian method [Aonishi and Ota, 2006, Ota et al., 2009b] with a smoothing prior, where the representation of the PRC is based on high order Fourier series. Their method can deal with data generated with various types of experiments, where arbitrary input is injected to a neuron. When the injection is a pulse, their method essentially corresponds to Bayesian regression based on the normal regression model.

In this thesis, we introduce another Bayesian regression with a smoothing prior (see Secs. 5.3 and 5.3), the framework of which is proposed by Tanabe and Tanaka [1983]. It is convenient for our method proposed in part II. This Bayesian regression is also based on the normal regression model. Hereafter, we call the Bayesian regression "spline regression". The estimate through the spline regression is shown in Fig. 3.3.

In this thesis, “conventional regression” means the method based on the normal regression model Eq.(3.2), where no errors exist in explanatory variable. The Fourier regression and the spline regression are the examples of the conventional regression.

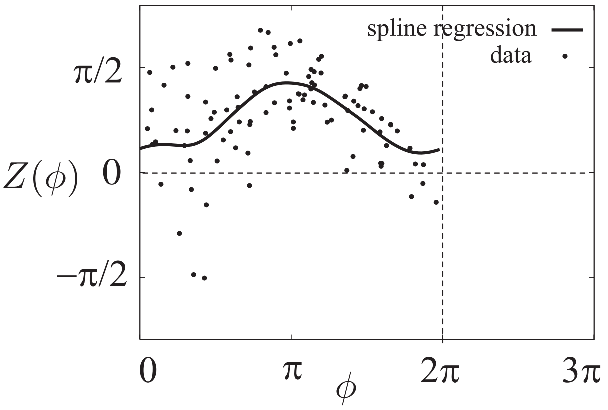

Figure 3.3: An example of the estimate obtained through spline regression

Other methods for different types of data

Recently, some methods are proposed for estimating PRCs using different types of data discussed in Sec. 3.1.

Phoka et al. [2010] proposes that supplemental data are added to the data explained in Sec. 3.1 using inter-spike intervals before and after the input of a neuron. The drawback of this method is that the estimated PRCs can not be a periodic function.

Ermentrout et al. [2007] and Ota et al. [2009a] propose that white and correlated noises are injected to a neuron, respectively. These experiments can be alternatives to the conventional experiments supposed in this thesis, although there are applications that would be difficult to treat with this approach, e.g., circadian rhythm.

Oprisan et al. [2003] estimates PRCs using the limit cycle reconstructed from membrane potential of a neuron. The PRCs estimated by this method correspond to PRCs where the strength of inputs are large in the operational definition of Sec. **??**; however, the strength should be small because of the definition from dynamical viewpoints in this thesis.

3.3 Measurement error model

The existence of the data point whose value $x_i \geq 2\pi$ implies errors in the explanatory variable. In my master thesis [Nakae, 2008], we discuss a measurement error model, where both errors in the explanatory and response variables are considered [Amari and Kawanabe, 1997, Cheng and Ness, 1999, Berry et al., 2002, Fuller, 2006, Caroll et al., 2006]. The measurement error model is expressed as

$$x_i = \phi_i + (\varepsilon_x)_i, \qquad (\varepsilon_x)_i \sim \mathcal{N}(0, (\sigma_x^2)_i), \tag{3.4}$$

$$y_i = Z(\phi_i) + (\varepsilon_y)_i, \qquad (\varepsilon_y)_i \sim \mathcal{N}(0, \sigma_y^2), \qquad , i = 1, \ldots, n, \tag{3.5}$$

where we assume that the variance $(\sigma_x^2)_i$ is proportional to x_i. The representation of the PRC $Z(\phi)$ in this model is that of the spline regression. In this model, the error $(\varepsilon_x)_i$ in the explanatory variable and the error $(\varepsilon_x)_i$ in the response variable are *independent* each other; the errors are not correlated. Unfortunately, we did not achieve a significant improvement over conventional regression in terms of accuracy.

3.4 Characteristics of errors in the data

In this section, we discuss two characteristics of errors in the data $\{(x_i, y_i)\}$ as follows:

1. The data point (x_i, y_i) whose value $x_i \geq 2\pi$ exist.
2. All data points are in the region $K = \{(x, y) \in \mathbb{R}^2 | x \geq 0, x + y \leq 2\pi\}$; as shown in the right panel of Fig. 3.4.

Characteristic 1 is caused by a perturbation inputted at the timing $t_i > \hat{T}$ as shown in the left panel of Fig. 3.4. Conventional regression can not deal with such data, because the domain of PRC is $[0, 2\pi)$.

Characteristic 2 is a consequence of the two inequalities for all $i = 1, \ldots, n$

$$x_i = 2\pi \frac{t_i}{\hat{T}} \geq 0, \tag{3.6}$$

$$x_i + y_i = 2\pi \frac{t_i}{\hat{T}} + 2\pi \frac{\hat{T} - T_i'}{\hat{T}} = 2\pi - \frac{2\pi}{\hat{T}}(T_i' - t_i) \leq 2\pi, \tag{3.7}$$

which are derived by the definition of the data point Eq.(3.1) and the trivial two inequalities $t_i \geq 0$ and $t_i \leq T_i'$.

The measurement error model Eqs. (3.4) and (3.5) is not sufficient; it generates the data points outside K, especially above the line $x + y = 2\pi$. This is because the error $(\varepsilon_x)_i$ and the error $(\varepsilon_y)_i$ are independent each other.

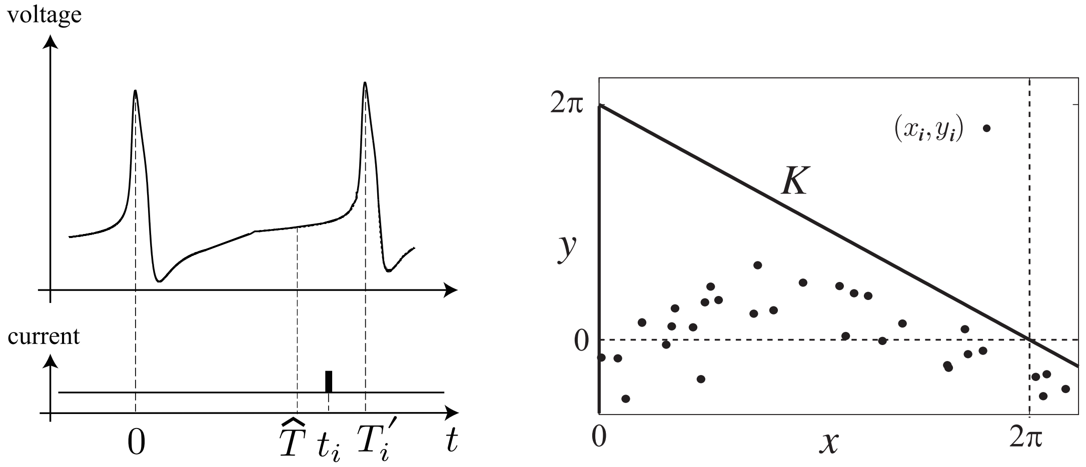

Figure 3.4: Two characteristics of the data.

3.5 Our Approach

The discussion in the previous section implies that the errors in the explanatory and response variables are not independent each other; the errors are correlated. Our motivation in this thesis is developing a statistical method dealing with the correlation.

In part II, we propose a statistical model, which represents a correlation between the explanatory and response variables. Based on the model, we provide a Bayesian method for estimating the PRCs using replica exchange Monte Carlo methods. In numerical experiments, we show that estimates obtained through the proposed method are more accurate than those obtained through conventional regressions.

Unfortunately, massive parallel computing environments are necessary for actual use of the proposed method. Without parallel computing, computation time of the proposed method is about 3 days for a sample size $n = 100$. On the other hand, computation time with parallel computing is reduced to approximately 2 hours for the same sample size. Our motivation of part III is developing a more efficient method based on the model proposed in part II.

In part III, the correlation is effectively removed using a transformation that mixes the explanatory and response variables. We show that the method through the transformation gives more accurate estimator than conventional regressions and the computation time is considerably less than that of the method in part II.

Chapter 4

Bayesian estimation and Markov chain Monte Carlo methods

4.1 Bayesian framework

In this section, we briefly explain a Bayesian framework used in this thesis. Suppose that observations $\mathbf{y} = \{y_i | i = 1, \ldots, n\}$ are independent and identically distributed; the distribution of the observations is depend on M-dimensional variables $\boldsymbol{\gamma} = (\gamma^{(1)}, \ldots, \gamma^{(M)}) \in \Gamma$ and M'-dimensional variables $\boldsymbol{\theta} \in \Theta$. The density function of the observation is represented by $p_{\boldsymbol{\gamma}}(\mathbf{y}|\boldsymbol{\theta})$. Here, the variables $\boldsymbol{\theta}$ called "parameters" are assumed to be random variables, while the variables $\boldsymbol{\gamma}$ called "hyperparameters" are assumed to be *not* random variables. The prior density of $\boldsymbol{\theta}$ is denoted by $p_{\boldsymbol{\gamma}}(\boldsymbol{\theta})$. The joint density of $\mathbf{y}$ and $\boldsymbol{\theta}$ is defined as

$$p_{\boldsymbol{\gamma}}(\mathbf{y}, \boldsymbol{\theta}) = p_{\boldsymbol{\gamma}}(\mathbf{y}|\boldsymbol{\theta}) p_{\boldsymbol{\gamma}}(\boldsymbol{\theta}). \tag{4.1}$$

We estimate the hyperparameters $\boldsymbol{\gamma}$ and the parameter $\boldsymbol{\theta}$ from the observations $\mathbf{y}$. The hyperparameters $\boldsymbol{\gamma}$ is estimated by an empirical Bayesian method [Good, 1965, Akaike, 1980, Titterington, 1985, MacKay, 1992] that maximizes the marginal likelihood

$$l_{\boldsymbol{\gamma}}(\mathbf{y}) = \int_{\boldsymbol{\theta} \in \Theta} p_{\boldsymbol{\gamma}}(\mathbf{y}, \boldsymbol{\theta}) d\boldsymbol{\theta} \tag{4.2}$$

over Γ. Once the estimate $\hat{\gamma}$ are obtained, the posterior density $p_{\hat{\gamma}}(\boldsymbol{\theta}|\mathbf{y})$ is derived by the

Bayes' theorem

$$p_{\hat{\gamma}}(\boldsymbol{\theta}|\mathbf{y}) = \frac{p_{\hat{\gamma}}(\mathbf{y}|\boldsymbol{\theta})p_{\hat{\gamma}}(\boldsymbol{\theta})}{l_{\hat{\gamma}}(\mathbf{y})}. \tag{4.3}$$

In the following sections, the parameter $\boldsymbol{\theta}$ is estimated by the expectation of $\boldsymbol{\theta}$ over the posterior distribution

$$\mathbb{E}_{\text{pos}}[\boldsymbol{\theta}] = \int_{\boldsymbol{\theta}\in\Theta} \boldsymbol{\theta} p_{\hat{\gamma}}(\boldsymbol{\theta}|\mathbf{y})d\boldsymbol{\theta}. \tag{4.4}$$

The estimate is denoted by $\hat{\boldsymbol{\theta}}$.

4.2 Markov chain Monte Carlo methods

4.2.1 Metropolis-Hastings method

The estimates $\hat{\gamma}$ and $\hat{\boldsymbol{\theta}}$ are automatically derived using the framework in the previous section. It is, however, difficult to give analytical representations of the marginal likelihood in Eq. (4.2) and the posterior expectation in Eq. (4.4), when the likelihood $p_{\gamma}(\mathbf{y}|\boldsymbol{\theta})$ and the prior $p_{\gamma}(\boldsymbol{\theta})$ are complicated. In this section, we explain a Metropolis-Hastings method [Hastings, 1970], which is one of Markov chain Monte Carlo (MCMC) methods, for approximating the integral in Eq. (4.4). The Metropolis-Hastings (MH) method is extended to a replica exchange Monte Carlo (REM) method [Geyer, 1991, Hukushima and Nemoto, 1996, Iba, 2001] in the next section. In Chap. 6, we will explain how to maximize the marginal likelihood in Eq. (4.2) based on the MCMC methods.

In the MCMC methods, the posterior expectation of $\boldsymbol{\theta}$ is approximated by the average of samples from the MCMC methods

$$\mathbb{E}_{\text{pos}}[\boldsymbol{\theta}] \approx \frac{1}{N_{\text{MC}}} \sum_{j=1}^{N_{\text{MC}}} \boldsymbol{\theta}^{j}, \tag{4.5}$$

where N_{MC} is the number of the samples, and $\boldsymbol{\theta}^j$ is jth sample. These samples are generated by the following procedure called Metropolis-Hastings methods. Here, we define a conditional distribution as a proposal distribution, whose density is represented by $q(\boldsymbol{\theta}'|\boldsymbol{\theta})$.

- Choose $\boldsymbol{\theta}_1$ in the region Θ.

  For $j = 1, \ldots, N_{\text{MC}-1}$

- Generate a candidate $\boldsymbol{\theta}^{\text{cand}} \sim q(\boldsymbol{\theta}'|\boldsymbol{\theta}_j)$
- Take

$$\boldsymbol{\theta}_{j+1} = \begin{cases} \boldsymbol{\theta}^{\text{cand}} & \text{with the probability } r, \\ \boldsymbol{\theta}_j & \text{otherwise,} \end{cases} \tag{4.6}$$

where

$$r = \min \left\{ \frac{p_\gamma(\mathbf{y}, \boldsymbol{\theta}^{\text{cand}}) q(\boldsymbol{\theta}^{\text{cand}}|\boldsymbol{\theta}^j)}{p_\gamma(\mathbf{y}, \boldsymbol{\theta}^j) q(\boldsymbol{\theta}^j|\boldsymbol{\theta}^{\text{cand}})}, 1 \right\}. \tag{4.7}$$

Note that $\boldsymbol{\theta}^{j+1} = \boldsymbol{\theta}^j$, when the candidate $\boldsymbol{\theta}^{\text{cand}}$ is out of the region Θ.

This procedure defines a Markov chain with the stationary density $p_\gamma(\boldsymbol{\theta}|\mathbf{y})$ on some convergence properties [Robert and Casella, 2004]. By simulating the Markov chain, we can draw samples of $\boldsymbol{\theta}$ according to the posterior density. Details of the general theory of MCMC can be found in books by [Robert and Casella, 2004, Gilks et al., 1995, MacKay, 2003, Gelman et al., 2003].

4.2.2 Replica exchange Monte Carlo method

The procedure explained in the previous section is a standard example of MCMC methods used in Bayesian statistics. It works if the number of iterations is sufficiently large. However, the number of iterations necessary to obtain stable results using such an algorithm can be very large in a complicated problem, which is known as “slow mixing” or “slow relaxation”. We will encounter the problem in part II of this thesis, where we can barely get stable results using a MH method in a range of hyperparameters.

To deal with this difficulty, we introduce the replica exchange Monte Carlo (REM) method, which is also known as parallel tempering or Metropolis coupled MCMC [Geyer, 1991, Hukushima and Nemoto, 1996, Iba, 2001].

REM is designed to increase the efficiency of MCMC method by connecting a fast mixing “easy” region to the slow mixing “difficult” region. The REM shares this idea with the simulated annealing algorithm for optimization, but there is an important difference. While simulated annealing is designed for obtaining an optimal solution and does not necessarily reproduce correct averages of statistics with a given distribution, the REM is designed for correct sampling and calculation of averages.

To implement the REM, we prepare N copies of the systems (replicas). Each replica corresponds to a posterior density $p_{\gamma'_k}(\boldsymbol{\theta}_k|\mathbf{y})$ parameterized by γ'_k. Here, γ'_k is usually a component of $\boldsymbol{\gamma}_k$; i.e. we denote $p_{(\gamma^{(1)},\ldots,\gamma'_k,\ldots,\gamma^{(M)})}(\boldsymbol{\theta}_k|\mathbf{y})$ as $p_{\gamma_k}(\boldsymbol{\theta}_k|\mathbf{y})$. The state of the kth replica is represented by $\boldsymbol{\theta}_k$. We assume that $\gamma'_1 \leq \gamma'_2 \leq \cdots \leq \gamma'_N$, and the hyperparameters γ'_1 and γ'_N correspond to the hyperparameters where the slowest and fastest mixing is observed, respectively. The idea of REM is to introduce occasional swaps of the states $\boldsymbol{\theta}_k$ and $\boldsymbol{\theta}_{k+1}$ of the replicas with the neighboring parameters γ'_k and γ'_{k+1}. The swap is performed as follows:

- Choose the index k of a replica randomly.
- Swap the pair with the probability

$$r = \min\left\{\frac{p_{\gamma'_k}(\mathbf{y},\boldsymbol{\theta}_{k+1})p_{\gamma'_{k+1}}(\mathbf{y},\boldsymbol{\theta}_k)}{p_{\gamma'_k}(\mathbf{y},\boldsymbol{\theta}_k)p_{\gamma'_{k+1}}(\mathbf{y},\boldsymbol{\theta}_{k+1})}, 1\right\}. \tag{4.8}$$

The entire algorithm of REM consists of a basic MCMC algorithm applied to each replica and the swap of replicas defined in the above.

An essential property of the swapping procedure of the REM is that it is designed for making the simultaneous density.

$$p(\boldsymbol{\theta}_1,\cdots,\boldsymbol{\theta}_N) = \prod_{k=1}^{N} p_{\gamma'_k}(\boldsymbol{\theta}_k|\mathbf{y}) \tag{4.9}$$

stationary. Through the swapping procedure, the states of the replicas in the fast mixing region propagate to the slow mixing region, which realizes an annealing effect as shown in Fig. 4.1. Even with such a propagation of states, we can reproduce the correct averages at all values $\{\gamma'_k\}$ of the parameter γ'; this is because the simultaneous density Eq. (4.9) represents the stationary distribution of the REM.

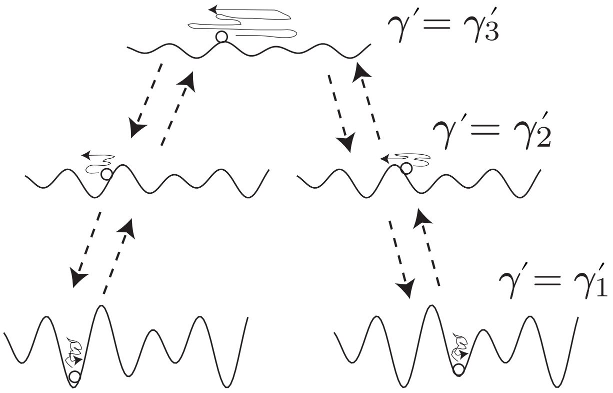
$\gamma' = \gamma'_3$
$\gamma' = \gamma'_2$
$\gamma' = \gamma'_1$

Figure 4.1: Schematic view of replica exchange Monte Carlo. For each value γ'_k of γ', the landscape sampled by MCMC is shown by the curve that represents $-\ln p_{\gamma'_k}(\cdot|\mathbf{y})$. A case with 3 replicas is shown in the figure, while 32 replicas are used in examples in part II.

Part II

Bayesian estimation of phase response curves using replica exchange Monte Carlo methods

Chapter 5

Bayesian model of phase response curves

5.1 Introduction

As discussed in Chap. 3, a common weakness of previous studies for estimating PRCs is that they neglect the correlation between errors in the PRC explanatory and response variables. The significance of this correlation is discussed in Sec. 5.2. This part is devoted to developing a new method that can deal with the correlation, which is realized by a systematic use of Bayesian methods. Using the method proposed in this part, we successfully improved the estimation accuracy for PRCs in examples of simulated data. The method is also applied to experimental data from the pyramidal cells in rat motor cortex.

The Bayesian model proposed in this part is non-linear and non-Gaussian; a standard way to treat such a model is by using Markov chain Monte Carlo (MCMC) methods [Gilks et al., 1995, MacKay, 2003, Gelman et al., 2003, Robert and Casella, 2004] such as Metropolis-Hastings methods in Chap. 4. For the current problem, however, a direct application of standard MCMC methods is difficult due to the slow convergence of MCMC. To deal with this difficulty, we introduce the replica exchange Monte Carlo (REM) method [Geyer, 1991, Hukushima and Nemoto, 1996, Iba, 2001] discussed in Chap. 4. REM is widely used in statistical physics and biomolecular simulations, and also applied to statistical inference [Geyer and Thompson, 1995, Huelsenbeck and Ronquist, 2001, Jasra et al., 2007]. Using REM, the difficulty is reduced, and we can get results within a reasonable amount of time.

This proposed method for PRC estimation is useful for any kind of nonlinear oscillator that permits the phase description. Although our current interest is in applications for brain science, the method can also be used in other fields of biology, chemistry, and physics.

The organization of this part is as follows. In this section, we propose a Bayesian model where we consider both the correlation of errors and smoothness of PRCs. In Chap. 6, we discuss how to estimate the PRC from data using REM. In Chap. 7, we test the proposed procedure with artificial data generated using the Morris-Lecar equations [Morris and Lecar, 1981] and data from a real experiment.

5.2 Derivation of the model

Effect of fluctuation of period T

As explained in Sec. 3.1, inter-spike intervals fluctuate stochastically in an experiment [Mainen and Sejnowski, 1995]; this suggests that period T itself should be considered as a random variable.

In conventional analysis, the period T in Eq. (1.1) is replaced by the average $\hat{T}$ of the inter-spike intervals of the neuron, which corresponds to the expectation of the random variable T. The resultant estimates x_i and y_i of ϕ_i and $Z(\phi_i)$ are represented by Eq. (3.1)

$$x_i = 2\pi \frac{t_i}{\hat{T}}, \qquad y_i = 2\pi \frac{\hat{T} - T'_i}{\hat{T}}.$$

In most existing studies, statistical analysis, such as fitting by trigonometric or spline functions, is performed after the data are normalized by Eq. (3.1) as discussed in Chap. 3.

We observed that this approach seems not optimal for our purposes. To explain the idea, we tentatively assume that we know the timing T_i of the next spike when the perturbation *does not* exist. The value T_i can be regarded as a realization of the random variable T in the ith trial. We can then define an i dependent normalization as

$$x'_i = 2\pi \frac{t_i}{T_i}, \qquad y'_i = 2\pi \frac{T_i - T'_i}{T_i}, \tag{5.1}$$

which leads to different estimates (x'_i, y'_i) of $(\phi_i, Z(\phi_i))$. Direct use of Eq. (5.1) is usually impossible in analysis of a real experiment where we cannot observe T_i. However, it will give results better than those from Eq. (3.1) when we know T_i.

To confirm this, we design the following numerical experiment. When we simulate a mathematical neuron model with noise on a computer, we can generate pairs of "perturbed" and "unperturbed" time-series of spikes using the same random number sequences. For the ith pair, a perturbation is added at $t = t_i$ for only the "perturbed" series. In this case, we can regard the inter-spike interval in the ith "unperturbed" series as T_i, which cannot be measured in a real experiment. Thus, we can realize the normalization with Eq. (5.1) and compare it to the results using Eq. (3.1).

Figure 5.1 shows the results of the experiment where the data is generated by the noisy Morris-Lecar equations (see appendix B). The values (x'_i, y'_i) of the variable normalized by Eq. (5.1) are plotted in the right panel, while the values (x_i, y_i) of the variable normalized by Eq. (3.1) are plotted in the left panel. The solid curve common to the panels corresponds to the true PRC estimated by numerical experiments without the noise term. The points (x'_i, y'_i) give a better approximation for the PRC, which supports our conjecture.

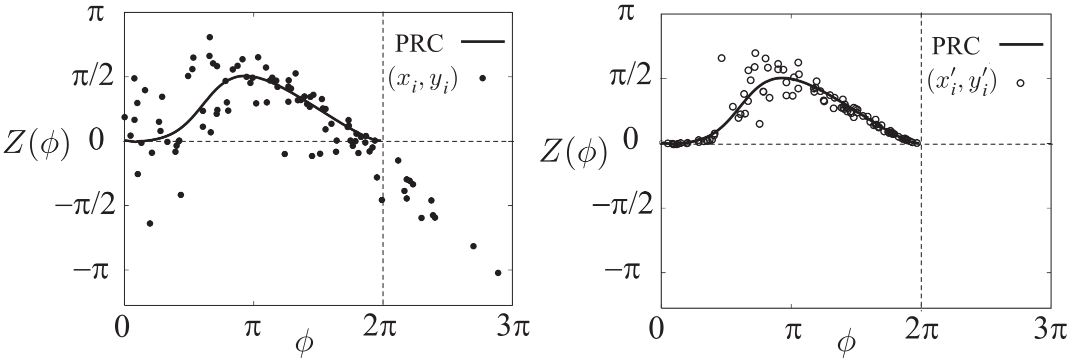

Figure 5.1: Comparison of the different normalization schemes. The left and right panels correspond to Eqs. (3.1) and (5.1), respectively.

An important observation is that the fluctuation of T_i causes a correlation between x_i and y_i as defined by Eq. (3.1). From Eqs. (3.1) and (5.1), the difference between (x_i, y_i) and (x'_i, y'_i) is written as

$$\begin{aligned} x_i - x'_i &= x_i \delta_i, \\ y_i - y'_i &= (y_i - 2\pi)\delta_i, \end{aligned} \tag{5.2}$$

where δ_i is defined by

$$\delta_i = \frac{T_i - \hat{T}}{T_i}. \tag{5.3}$$

If we assume that a point $(\phi_i, Z(\phi_i))$ on the true PRC is approximated well by the improved estimate (x_i', y_i'), the difference $(x_i - x_i', y_i - y_i')$ can be regarded as the error of the naive estimate (x_i, y_i). Equation (5.2) indicates that the errors in the explanatory variable is not negligible and that there is a strong correlation between the errors in the explanatory and response variables.

Figure 5.2 visualizes the correlation in the data of Fig. 5.1. Each arrow in Fig. 5.2 represents the vector $(x_i - x_i', y_i - y_i')$, where the starting point of the arrow is (x_i', y_i') and the endpoint is (x_i, y_i). The solid curve is the true PRC of the Morris-Lecar equations. The correlation is shown by the systematic distribution of the lengths and directions of the arrows, and is clearly seen in the data.

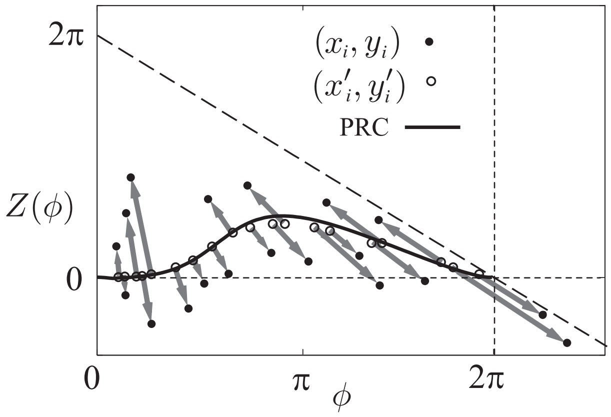

Figure 5.2: Correlated errors in an estimated PRC. The arrows showing the correlation never exceed the broken line, which corresponds to the constraint $t_i \leq T_i'$.

Estimation of Unobserved T_i

In real experiments, we cannot identify T_i directly. Our strategy in this part is to estimate both $Z(\cdot)$ and $\{T_i\}$ simultaneously. We give here a rough sketch of the concept. The method proposed in this part will be gone over in more details in Sec. 5.3 and Chap. 6.

In the previous section, we identified the points $\{(x_i', y_i')\}$ to $\{(\phi_i, Z(\phi_i))\}$, but there are actually some observational noises, i.e., we can write

$$\begin{aligned} x'_i &= \phi_i + \eta_i, \\ y'_i &= Z(\phi_i) + \xi_i, \end{aligned} \tag{5.4}$$

where η_i and ξ_i are small residual terms. Hereafter, we set $\eta_i = 0$. Later, in the analysis detailed in Sec. 5.3, we will assume that $\{\xi_i\}$ are samples from the normal distribution $\mathcal{N}(0, \theta^2)$.

Using Eq. (5.2) and Eq. (5.4) with $\eta_i = 0$, we have the relation

$$x_i = \phi_i + x_i\delta_i, \tag{5.5}$$

$$y_i = Z(\phi_i) + (y_i - 2\pi)\delta_i + \xi_{i.} \tag{5.6}$$

Note that δ_i in Eqs. (5.5) and (5.6) is defined from T_i by Eq. (5.3), and the data (x_i, y_i) is the output of an experiment normalized by the conventional Eq. (3.1). Given the function $Z(\cdot)$ and a prior distribution of δ_is, we can estimate $\{\delta_i\}$ (or equivalently $\{T_i\}$) by using Eqs. (5.5) and (5.6). On the other hand, given a set of $\{\delta_i\}$, Eqs. (5.5) and (5.6) are reduced to a functional regression problem of estimating $Z(\cdot)$, which can be treated by assuming some parametric form or smoothness of the function $Z(\cdot)$.

Roughly speaking, our goal of estimating both $Z(\cdot)$ and $\{\delta_i\}$ simultaneously can be attained by solving undetermined stochastic equations Eqs. (5.5) and (5.6) with assumptions for $Z(\cdot)$ and $\{\delta_i\}$. However, it is not so obvious as to how to formulate such a complicated problem and solve it. In this study, a combination of a Bayesian framework and MCMC is proposed as a systematic solution to the problem, which will be explained in the following sections.

5.3 Bayesian model in part II

Bayesian framework

As we discussed in the previous section, our task can be summarized as a simultaneous estimation of $Z(\cdot)$ and $\{\delta_i\}$ from the data $\{(x_i, y_i)\}$ defined by Eq. (3.1). In a Bayesian framework, we begin with writing down the simultaneous density of relevant variables.

Given δ_i, we can erase ϕ_i using the deterministic relation Eq. (5.5) and data $\{x_i\}$. The simultaneous density of $\mathbf{y}, Z$ and $\boldsymbol{\delta}$ is then written as

$$p(\mathbf{y}, Z, \boldsymbol{\delta}) = p(\mathbf{y}|Z, \boldsymbol{\delta})\, p(Z)\, p(\boldsymbol{\delta}). \tag{5.7}$$

Our Bayesian model now consists of three components; the likelihood function $p(\mathbf{y}|Z, \boldsymbol{\delta})$, and the prior distributions $p(Z)$ and $p(\boldsymbol{\delta})$, which will be defined in Secs. 5.3 – 5.3. Once these components are defined, the simultaneous density Eq. (5.7) is explicitly given, and the Bayes' theorem provides the posterior density

$$p(Z, \boldsymbol{\delta}|\mathbf{y}) = \frac{p(\mathbf{y}|Z, \boldsymbol{\delta})\, p(Z)\, p(\boldsymbol{\delta})}{\displaystyle\iint p(\mathbf{y}|Z, \boldsymbol{\delta})\, p(Z)\, p(\boldsymbol{\delta})\ d\boldsymbol{\delta}\, dZ} \tag{5.8}$$

of Z and $\boldsymbol{\delta}$. In the Bayesian framework, estimators of any quantity are derived from Eq. (5.8). For example, we can estimate the curve $Z(\cdot)$ that minimizes the posterior expectation of mean square loss as an average of Z over the distribution defined by the density Eq. (5.8).

In Eq. (5.8), the symbols $\int \cdots d\boldsymbol{\delta}$ and $\int \cdots dZ$ denote multiple integration and integration in a function space, respectively; the latter is approximated by finite dimensional integrals in an actual computation. Even with such an approximation, the sampling and calculation of averages with the posterior distribution Eq. (5.8) is far from trivial. This will be treated by MCMC in Chap. 6.

Representation of $Z(\cdot)$

Before defining the factors on the right hand side of Eq. (5.7), let us fix a representation of the function $Z(\cdot)$. We use a naive discretization of $Z(\cdot)$; this representation is convenient for our problem, where $\{x_i'\}$ are not uniformly separated and should be estimated from data.

We divide the ϕ axis into m successive intervals $\{[\phi_j^*, \phi_{j+1}^*),\ j = 1, \cdots, m\}$ of equal lengths. The piecewise constant curve $Z(\cdot)$ indexed with $\mathbf{z} = (z_1, \cdots, z_m)^T$ is then defined by $Z(\phi) = z_j$ for $\phi \in [\phi_j^*, \phi_{j+1}^*)$. Here $(\ )^T$ denotes the transpose of a vector. These definitions are illustrated in the Fig. 5.3.

When we use the discretized representation of $Z(\cdot)$ defined here, it is convenient to

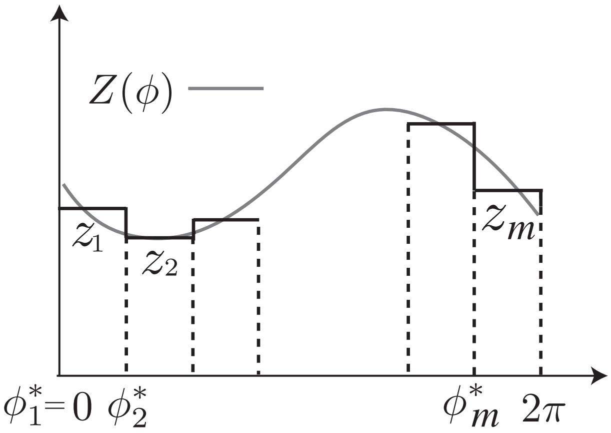

Figure 5.3: Representation of the function $Z(\cdot)$.

define the $n \times m$ matrix function $E(\mathbf{v})$ of $\mathbf{v} = (v_1, \ldots, v_n)$, whose (i, j) component is given by

$$E_{ij}(\mathbf{v}) = \begin{cases} 1 & v_i \in [\phi_j^*, \phi_{j+1}^*) \\ 0 & v_i \notin [\phi_j^*, \phi_{j+1}^*), \end{cases} \tag{5.9}$$

which we will use in Sec. 5.3.

Likelihood $p(y|Z, \boldsymbol{\delta})$

Let us begin with Eq. (5.4) in Sec. 5.2. Assuming that $\{\xi_i\}$ are independently distributed with the normal distribution $\mathcal{N}(0, \theta^2)$, the probability density $p(\mathbf{y}'|Z)$ of $\mathbf{y}'$ is written as

$$p(\mathbf{y}'|\mathbf{z}) = \frac{1}{\sqrt{2\pi\theta^2}} \exp\left\{-\frac{1}{2\theta^2}||\mathbf{y}' - E(\mathbf{x}')\mathbf{z}||^2\right\}, \tag{5.10}$$

where $\mathbf{x}'$ and $\mathbf{y}'$ are defined as a vector whose ith component is given by x_i' and y_i' in Eq. (5.1) respectively. Here $\mathbf{z}$ is the discretized representation of $Z(\cdot)$ and we use the $n \times m$ matrix $E(\mathbf{x}')$ defined by Eq. (5.9).

To obtain an explicit form of the density $p(\mathbf{y}|\mathbf{z}, \boldsymbol{\delta})$, the stochastic variable $\mathbf{y}'$ in Eq. (5.10) should be changed to $\mathbf{y}$). In addition, the variable $\mathbf{x}'$ should be represented by x_i and δ_i.

This can be done with the following relation,

$$x'_i = (1 - \delta_i)x_i, \tag{5.11}$$

$$y'_i = (1 - \delta_i)y_i + 2\pi\delta_i, \tag{5.12}$$

which is derived from Eq. (5.2). Using Eq. (5.11), the density $p(\mathbf{y}|\mathbf{z}, \boldsymbol{\delta})$ can be expressed in the matrix form

$$p(\mathbf{y}|\mathbf{z}, \boldsymbol{\delta}) = \left\{ \prod_{i=1}^{n} \frac{(1 - \delta_i)}{\sqrt{2\pi\theta^2}} \right\} \exp\left\{ -\frac{1}{2\theta^2} ||\mathbf{y}'(\boldsymbol{\delta}) - E(\mathbf{x}'(\boldsymbol{\delta}))\mathbf{z}||^2 \right\}, \tag{5.13}$$

where $\mathbf{x}'(\boldsymbol{\delta})$ and $\mathbf{y}'(\boldsymbol{\delta})$ are defined as vectors whose ith component is given by $x'_i(\boldsymbol{\delta}) = (1 - \delta_i)x_i$ and $y'_i(\boldsymbol{\delta}) = (1 - \delta_i)y_i + 2\pi\delta_i$, respectively. Note that the variance of y_i is computed as $\theta^2/(1 - \delta_i)^2$, which corresponds to the normalization factor $(1 - \delta_i)/\sqrt{2\pi\theta^2}$ in Eq. (5.13).

The Prior $p(\boldsymbol{\delta})$

A simple choice for the prior distribution of T_i is a normal distribution. However, it is reasonable to assume that $t_i \leq T_i$, because a neuron should fire after the perturbation is added. Thus, it is better to assume a truncated normal distribution $\mathcal{N}_{[t_i,\infty)}(\hat{T}, \hat{\sigma_T})$ as the prior distribution of T_i, whose density is given by

$$p(T_i) = \begin{cases} \dfrac{1}{\iota_i} \exp\left\{ -\dfrac{(T_i - \hat{T})^2}{2\hat{\sigma_T}^2} \right\}, & t_i \leq T_i, \\ 0, & \text{otherwise}, \end{cases} \tag{5.14}$$

where $\hat{T}$ and $\hat{\sigma_T}$ are the sample average and the sample variance of inter-spike intervals of the neuron, respectively.

When we change the variable from T_i to $\delta_i = (T_i - \hat{T})/T_i$, it is transformed to the prior density of δ_i

$$p(\delta_i) = \begin{cases} \dfrac{1}{\iota'_i}\dfrac{1}{(1-\delta_i)^2}\exp\left\{-\dfrac{1}{2(\hat{\sigma_T}/\hat{T})^2}\dfrac{\delta_i^2}{(1-\delta_i)^2}\right\}, & 1-\dfrac{2\pi}{x_i} \le \delta_i < 1. \\ 0, & \text{otherwise.} \end{cases} \tag{5.15}$$

Here ι_i and ι'_i are the normalization constants. The prior $p(\boldsymbol{\delta})$ is expressed as $\prod_{i=1}^{n} p(\delta_i)$ with $p(\delta_i)$ defined by Eq. (5.15).

The Prior $p(Z(\cdot))$

We assume that the phase response curves are smooth and periodic functions. To represent this, a smoothness prior of $Z(\cdot)$ is introduced. Using the discretized representation of $Z(\cdot)$, it is expressed as

$$p(\mathbf{z}) = \frac{1}{\iota(\tau)}\exp\left\{-\frac{\tau^2}{2}\sum_{j=1}^{m}(z_{j-1}-2z_j+z_{j+1})^2\right\}, \tag{5.16}$$

where we assume the periodic boundary condition $z_0 = z_m, z_{m+1} = z_1$. Equation (5.16) can also be expressed in the matrix form

$$p(\mathbf{z}) = \frac{1}{\iota(\tau)}\exp\left(-\frac{\tau^2}{2}||D\mathbf{z}||^2\right), \tag{5.17}$$

where the $m \times m$ matrix D is defined by

$$D = \begin{bmatrix} -2 & 1 & 0 & \dots & 0 & 0 & 1 \\ 1 & -2 & 1 & 0 & \dots & 0 & 0 \\ 0 & 1 & -2 & 1 & \dots & 0 & 0 \\ 0 & 0 & 1 & -2 & \dots & 0 & 0 \\ \vdots & \vdots & \vdots & \ddots & \ddots & \vdots & \vdots \\ 0 & 0 & 0 & \dots & 1 & -2 & 1 \\ 1 & 0 & 0 & \dots & 0 & 1 & -2 \end{bmatrix}. \tag{5.18}$$

The term $(z_{j-1}-2z_j+z_{j+1})^2$ in Eq. (5.16) represents the smoothness of the curve $Z(\cdot)$.

When the hyperparameter τ is larger, the estimated PRC $Z(\cdot)$ becomes smoother. This prior is essentially the same as the one introduced by [Aonishi and Ota, 2006], but here we utilize the discretized representation $\{z_j\}$ of the PRC $Z(\cdot)$ defined in Sec. 5.3. Smoothness priors in statistical science and machine learning have been discussed in the literature, *e.g.*, [Titterington, 1985, Wahba, 1990, Kitagawa and Gersch, 1996, MacKay, 1992]; regression using discretized representation and a smoothness prior is also considered as a version of spline regression [Wahba, 1990].

Precisely speaking, Eq. (5.16) defines an improper prior of $\mathbf{z}$, that is, we cannot give a finite normalization constant $\iota(\tau)$ without some additional regularization term. However, it is harmless for our purpose of estimating $\mathbf{z}$ and hyperparameters. The latter is because we can separate a finite part of $\iota(\tau)$ that reproduces the correct dependence of $\iota(\tau)$ on τ.

An alternative choice for the prior comes from the use of the fixed boundary condition $Z(0) = 0$, which is a consequence of the refractory period of a neuron and biologically plausible. In this case, the matrix form of the prior becomes

$$p(\mathbf{z}) = \frac{1}{\bar{\iota}(\tau)} \exp\left(-\frac{\tau^2}{2}||\bar{D}\mathbf{z}||^2\right), \tag{5.19}$$

where $\bar{D}$ is given by deleting the first row of the matrix D. In this case, the prior Eq. (5.19) is proper.

Hyperparameters

The Bayesian model defined in this chapter contains the tunable parameters $\hat{\sigma_T}$, $\hat{T}$, θ, and τ. Among them, $\hat{\sigma_T}$ and $\hat{T}$ can be measured in a preliminary experiment without perturbations. On the other hand, θ and τ are difficult to determine from auxiliary information and should be estimated from the present data $\{(x_i, y_i)\}$. In this part, these two parameters are treated as "hyperparameters" of the model and estimated by an empirical Bayesian method [Good, 1965, Akaike, 1980, Titterington, 1985, MacKay, 1992] that maximizes their marginal likelihood

$$l(\mathbf{y}|\theta, \tau) = \int\!\!\int p_\theta(\mathbf{y}|\mathbf{z}, \boldsymbol{\delta}) p_\tau(\mathbf{z}) p(\boldsymbol{\delta})\, d\boldsymbol{\delta} d\mathbf{z} \tag{5.20}$$

of these hyperparameters θ and τ. Here we explicitly show the dependence of $p(\mathbf{y}|\mathbf{z}, \boldsymbol{\delta})$ and $p(\mathbf{z})$ on the hyperparameters as $p_\theta(\mathbf{y}|\mathbf{z}, \boldsymbol{\delta})$ and $p_\tau(\mathbf{z})$. How to utilize the output of MCMC for maximizing Eq. (5.20) will be discussed in the next chapter.

Chapter 6

Estimation of the model using MCMC methods

6.1 Basic Markov chain Monte Carlo method

As explained in Sec. 5.3, once we define a Bayesian model, the posterior distribution $p(\mathbf{z}, \boldsymbol{\delta}|\mathbf{y})$ is automatically derived by the Bayes' theorem. It is, however, difficult to give an analytical representation of posterior averages because our likelihood and prior are very complicated. Here, we introduce a Markov chain Monte Carlo (MCMC) algorithm that consists of alternate sampling of $\mathbf{z}$ and $\boldsymbol{\delta}$.

Sampling of $\mathbf{z}$

The sampling of $\mathbf{z}$ is defined by drawing a new value of $\mathbf{z}$ according to the conditional density $p(\mathbf{z}|\boldsymbol{\delta}, \mathbf{y})$, which is given by the normal density with the mean

$$\boldsymbol{\mu}_{\mathbf{z}} = (E^T E + \theta^2 \tau^2 D^T D)^{-1} E^T \mathbf{y}', \tag{6.1}$$

and variance

$$\Sigma_{\mathbf{z}} = \left(\frac{1}{\theta^2} E^T E + \tau^2 D^T D \right)^{-1}, \tag{6.2}$$

where E and $\mathbf{y}'$ are shortened forms of $E(\mathbf{x}'(\boldsymbol{\delta}))$ and $\mathbf{y}'(\boldsymbol{\delta})$, respectively. The matrices $E(\mathbf{x}'(\boldsymbol{\delta}))$ and D and the vector function $\mathbf{y}'(\boldsymbol{\delta})$ used here are defined in Secs. 5.3, 5.3, and 5.3. Using the Cholesky decomposition of the matrix $\Sigma_{\mathbf{z}}^{-1}$, all components of $\mathbf{z}$ are generated simultaneously by a standard method (see, for example, [Gelman et al., 2003]).

Sampling of δ

Sampling of $\boldsymbol{\delta}$ is a little difficult because the distribution of $\boldsymbol{\delta}$ conditional on $\mathbf{z}$ is complicated and direct sampling is impossible. Here, we use the Metropolis method [Metropolis et al., 1953], which is a version of Markov chain Monte Carlo methods. Our implementation of the Metropolis method is as follows. First, we randomly select a component δ_i of $\boldsymbol{\delta}$. A candidate δ_i^{cand} for a new value of δ_i is then generated near the current value δ_i^{curr} of δ_i, as $\delta_i^{\text{cand}} = \delta_i^{\text{curr}} + \epsilon$, where $\epsilon \sim \mathcal{N}(0, \kappa^2)$ and the constant κ^2 is a parameter of the algorithm. Finally, the candidate δ_i^{cand} is accepted or rejected by comparing the ratio

$$q = \frac{p(\delta_i^{\text{cand}} | \boldsymbol{\delta}_{-i}, \mathbf{z}, \mathbf{y})}{p(\delta_i^{\text{curr}} | \boldsymbol{\delta}_{-i}, \mathbf{z}, \mathbf{y})} \tag{6.3}$$

to a uniform random number $r \in [0, 1)$ that is generated independently. If $r \leq q$, the candidate δ_i^{cand} is accepted as a new value of δ_i. Otherwise, if $r > q$, the candidate is rejected and we keep the current value $\delta_i = \delta_i^{\text{curr}}$. Note that $\boldsymbol{\delta}_{-i}$ in Eq. (6.3) indicates $\{\delta_j\}, j \neq i$.

Here, we derive the ratio q of our Bayesian model; the right side of Eq. (6.3) is calculated as follows

$$\frac{p(\delta_i^{\text{cand}} | \boldsymbol{\delta}_{-i}, \mathbf{z}, \mathbf{y})}{p(\delta_i^{\text{curr}} | \boldsymbol{\delta}_{-i}, \mathbf{z}, \mathbf{y})} = \frac{p(\delta_i^{\text{cand}}, \boldsymbol{\delta}_{-i}, \mathbf{z}, \mathbf{y})}{p(\delta_i^{\text{curr}}, \boldsymbol{\delta}_{-i}, \mathbf{z}, \mathbf{y})} = \frac{p(\mathbf{y} | \mathbf{z}, \delta_i^{\text{cand}}, \boldsymbol{\delta}_{-i}) p(\delta_i^{\text{cand}}, \boldsymbol{\delta}_{-i}) p(\mathbf{z})}{p(\mathbf{y} | \mathbf{z}, \delta_i^{\text{curr}}, \boldsymbol{\delta}_{-i}) p(\delta_i^{\text{curr}}, \boldsymbol{\delta}_{-i}) p(\mathbf{z})}$$

$$= \frac{p(y_i | \mathbf{z}, \delta_i^{\text{cand}}) p(\delta_i^{\text{cand}})}{p(y_i | \mathbf{z}, \delta_i^{\text{curr}}) p(\delta_i^{\text{curr}})}, \tag{6.4}$$

where we use definition of conditional probability and joint probability of our model. Using the likelihood defined by Eq. (5.13) and the prior of δ_i defined by Eq. (5.15), the ratio is expressed as

$$\begin{aligned} q = \exp\{ &- \frac{1}{2\theta^2}(y_i'^{\text{cand}} - z_j^{\text{cand}})^2 - \frac{1}{2\sigma_T^2}\left(\frac{\delta_i^{\text{cand}}}{1-\delta_i^{\text{cand}}}\right) - \log(1-\delta_i^{\text{cand}}) \\ &+ \frac{1}{2\theta^2}(y_i'^{\text{curr}} - z_j^{\text{curr}})^2 + \frac{1}{2\sigma_T^2}\left(\frac{\delta_i^{\text{curr}}}{1-\delta_i^{\text{curr}}}\right) + \log(1-\delta_i^{\text{curr}})\}. \end{aligned} \tag{6.5}$$

The terms $y_i'^{\text{cand}}$ and $y_i'^{\text{curr}}$ are defined by Eq. (5.12); the terms z_j^{cand} and $z_j'^{\text{curr}}$ are the i-th component of the vectors $E((\delta_i^{\text{cand}}, \boldsymbol{\delta}_{-i}))\mathbf{z}$ and $E((\delta_i^{\text{curr}}, \boldsymbol{\delta}_{-i}))\mathbf{z}$, respectively.

Summary of the MCMC algorithm

The summary of the MCMC algorithm is described as follows:

1. Initialize $\mathbf{z}$ and $\boldsymbol{\delta}$. Set a counter $N_{\text{MC}} = 0$.
2. Update $\mathbf{z}$.
    - Compute the Cholesky decomposition of the matrix $\Sigma_{\mathbf{z}}^{-1}$.
    - Draw a new value of the random number $\mathbf{z}$ according to the normal distribution defined by $\boldsymbol{\mu}_{\mathbf{z}}$ and $\Sigma_{\mathbf{z}}^{-1}$.
3. Update $\boldsymbol{\delta}$.
    - Choose i randomly.
    - Draw $\epsilon \sim \mathcal{N}(0, \kappa^2)$ and define the candidate by $\delta_i^{\text{cand}} = \delta_i^{\text{curr}} + \epsilon$, where δ_i^{curr} is the current value of δ_i.
    - Compute the ratio q by Eq. (6.3).
    - Draw a uniform random number $r \in [0, 1)$.
      Set the value of δ_i to δ_i^{cand} if $r \leq q$.

    $\star$ It is possible to define a modification where this step is repeated multiple times.
4. Set $N_{\text{MC}} = N_{\text{MC}} + 1$. If N_{MC} is smaller than the prescribed value, return to step 2. Otherwise, terminate the procedure.

These steps define an ergodic Markov chain with stationary density $p(\mathbf{z}, \boldsymbol{\delta}|\mathbf{y})$. By simulating the Markov chain, we can draw samples of $\mathbf{z}$ and $\boldsymbol{\delta}$ according to the posterior density

$p(\mathbf{z}, \boldsymbol{\delta}|\mathbf{y})$. These samples are correlated but can be used for computing posterior averages. Details of the general theory of MCMC can be found in books by [Robert and Casella, 2004, Gilks et al., 1995, MacKay, 2003, Gelman et al., 2003]; some examples of applications of MCMC to models with errors in explanatory variables are found in [Berry et al., 2002, Caroll et al., 2006, Gilks et al., 1995].

Example

Here, we test this basic MCMC algorithm with artificial data generated by a neuron model. We employ the noisy Morris-Lecar equation [Morris and Lecar, 1981] as a source of artificial data; the details of the numerical experiments are discussed in appendix B.

The points in Fig. 6.1 represent the artificial data, which contain $n = 100$ samples. Here, the level s of the noise is 0.3 (see appendix B). The estimates of mean and variance of periods are $\hat{T} = 44.2$ and $\hat{\sigma_T} = 6.4$. The result of the method is compared with the true PRC (the broken curve in Fig. 6.1) estimated with noiseless experiments.

The red curves in Fig. 6.1 shows the PRCs estimated with the basic MCMC algorithm; each red curve is different about the initial point $(\mathbf{Z}, \boldsymbol{\delta})$ of the method. All estimated curves are not close to the true curve. This means that more sophisticated method is necessary for faster convergence to the stationary density.

The details of the algorithm used in computing the above result are as follows. We set hyperparameters $\theta \approx 0.09$ and $\tau \approx 90$. The number m of the pieces of the discretized curve $Z(\cdot)$ is 100 and the periodic boundary condition is assumed. The number N_{MC} of iterations is 10^6. The variance κ_k of the proposal distribution is 0.01.

6.2 Extension to replica exchange methods

Transformation of hyperparameters

The procedure explained in the previous section is a standard example of MCMC methods used in Bayesian statistics. It works if the number of iterations is sufficiently large. However, the number of iterations necessary to obtain stable results using such an algorithm can be very large in a complicated problem, which is known as “slow mixing” or “slow relaxation”. We found that our problem of estimating PRCs from data with correlated errors

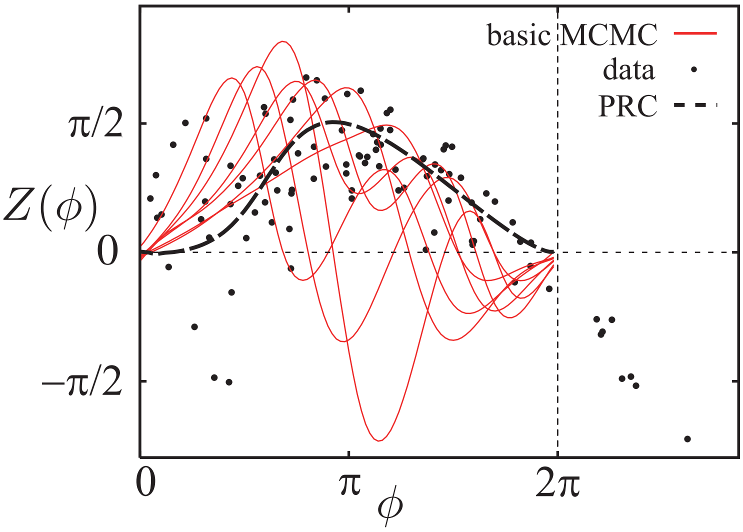

Figure 6.1: Result of applying the basic MCMC algorithm using artificial data. The estimated PRCs (red curves) are different about the initial points $(\mathbf{Z}, \boldsymbol{\delta})$ of the method.

gives a typical example of slow mixing; this is partially supported by the example of the previous section. In a range of hyperparameters, we can barely get stable results using a naive MCMC algorithm.

To deal with this difficulty, we use the replica exchange Monte Carlo (REM) method discussed in Sec. 4.2.2, where we discussed a generic algorithm. When REM is used in statistical physics, the parameter γ' in the generic algorithm usually corresponds to the temperature of a system. How can we choose the parameter γ' in the present example of posterior sampling?

A basic observation is that the values of hyperparameters θ^2 and $1/\tau^2$ become larger, the variance of the posterior also becomes larger. Keeping this in mind, we transform the set (θ, τ) of hyperparameters to (α, β) with

$$\alpha = \theta\tau, \qquad \beta = \theta/\tau \tag{6.6}$$

Here, the hyperparameter β corresponds to the temperature in statistical physics. In a Gaussian model where the errors in the explanatory variable is ignored [Ota et al., 2009b, Aonishi and Ota, 2006], α determines the shape of the estimated curve while β determines the variance around the curve. In the proposed model, however, both hyperparameters affects the estimated PRC.

Then, the hyperparameter β is the natural choice for the role of γ'; the density $p_{\gamma'_k}(\boldsymbol{\theta}_k|\mathbf{y})$ in the generic algorithm is replaced with $p_{\beta_k}(\mathbf{z},\boldsymbol{\delta}|\mathbf{y})$, which defines the REM for the proposed model.

Replica exchange Monte Carlo

To implement the REM, we prepare N copies of the systems (replicas). Each replica corresponds to a posterior density $p_{\beta_k}(\mathbf{z}_k,\boldsymbol{\delta}_k|\mathbf{y})$ parameterized by β_k, where $\beta_1 \le \beta_2 \le \cdots \le \beta_N$. We assume that the hyperparameters β_1 and β_N correspond to the hyperparameters where the slowest and fastest mixing is observed, respectively. The REM is implemented with occasional swaps of the states $(\mathbf{z}_k,\boldsymbol{\delta}_k)$ and $(\mathbf{z}_{k+1},\boldsymbol{\delta}_{k+1})$ of the replicas with the neighboring parameters β_k and β_{k+1}. The swap is performed as follows:

- Choose the index k of a replica randomly.
- Swap the pair with the probability

$$r = \min\left\{\frac{p_{\beta_k}(\mathbf{y},\mathbf{z}_{k+1},\boldsymbol{\delta}_{k+1})p_{\beta_{k+1}}(\mathbf{y},\mathbf{z}_k,\boldsymbol{\delta}_k)}{p_{\beta_k}(\mathbf{y},\mathbf{z}_k,\boldsymbol{\delta}_k)p_{\beta_{k+1}}(\mathbf{y},\mathbf{z}_{k+1},\boldsymbol{\delta}_{k+1})},1\right\}. \tag{6.7}$$

The entire algorithm of REM consists of a basic MCMC algorithm applied to each replica and the swap of replicas defined in Sec. 6.1. The details of the REM are explained in Chap. 4

Here, we derive the probability r of our Bayesian model under a value of hyperparameter α. Using Eq. (5.7), the ratio in Eq. (6.7) is calculated as follows:

$$\begin{aligned}\frac{p_{\beta_k}(\mathbf{y},\mathbf{z}_{k+1},\boldsymbol{\delta}_{k+1})p_{\beta_{k+1}}(\mathbf{y},\mathbf{z}_k,\boldsymbol{\delta}_k)}{p_{\beta_k}(\mathbf{y},\mathbf{z}_k,\boldsymbol{\delta}_k)p_{\beta_{k+1}}(\mathbf{y},\mathbf{z}_{k+1},\boldsymbol{\delta}_{k+1})} &= \frac{p_{\beta_k}(\mathbf{y},\mathbf{z}_{k+1}|\boldsymbol{\delta}_{k+1})p(\boldsymbol{\delta}_{k+1})p_{\beta_{k+1}}(\mathbf{y},\mathbf{z}_k|\boldsymbol{\delta}_k)p(\boldsymbol{\delta}_k)}{p_{\beta_k}(\mathbf{y},\mathbf{z}_k|\boldsymbol{\delta}_k)p(\boldsymbol{\delta}_k)p_{\beta_{k+1}}(\mathbf{y},\mathbf{z}_{k+1}|\boldsymbol{\delta}_{k+1})p(\boldsymbol{\delta}_{k+1})} \\ &= \frac{p_{\beta_k}(\mathbf{y},\mathbf{z}_{k+1}|\boldsymbol{\delta}_{k+1})p_{\beta_{k+1}}(\mathbf{y},\mathbf{z}_k|\boldsymbol{\delta}_k)}{p_{\beta_k}(\mathbf{y},\mathbf{z}_k|\boldsymbol{\delta}_k)p_{\beta_{k+1}}(\mathbf{y},\mathbf{z}_{k+1}|\boldsymbol{\delta}_{k+1})},\end{aligned} \tag{6.8}$$

where we use the independence between the prior $p(\boldsymbol{\delta})$ and the hyperparameter $\beta = \theta\tau$. The probability $p_\beta(\mathbf{y}, \mathbf{z}|\boldsymbol{\delta})$ are expressed as

$$p_\beta(\mathbf{y}, \mathbf{z}|\boldsymbol{\delta}) = p_\beta(\mathbf{y}|\mathbf{z}, \boldsymbol{\delta}) p_\beta(\mathbf{z}) \propto \exp\left\{-\frac{1}{2\beta} H(\mathbf{z}, \boldsymbol{\delta})\right\}, \tag{6.9}$$

where the function $H(\mathbf{z}, \delta)$ is defined as

$$H(\mathbf{z}, \boldsymbol{\delta}) = \alpha ||\mathbf{y}'(\boldsymbol{\delta}) - E(\boldsymbol{\delta})\mathbf{z}||^2 + \frac{1}{\alpha}||D\mathbf{z}||^2. \tag{6.10}$$

Using this expression of $p_\beta(\mathbf{y}, \mathbf{z}|\boldsymbol{\delta})$, we obtain the following probability:

$$r = \min\left\{\exp\left\{-\frac{1}{2}\left(\frac{1}{\beta_{k+1}} - \frac{1}{\beta_k}\right)(H(\mathbf{z}_k, \boldsymbol{\delta}_k) - H(\mathbf{z}_{k+1}, \boldsymbol{\delta}_{k+1}))\right\}, 1\right\}. \tag{6.11}$$

Design of replica exchange Monte Carlo

To design an efficient REM, the variance κ^2 of the proposal distribution used in the basic algorithm should depend on the index k of replicas. In Chap. 7, we use the following formula

$$\kappa_k = \frac{\kappa_N - \kappa_1}{N - 1} \times (k - 1) + \kappa_1, \tag{6.12}$$

for the value κ_k of κ in the kth replica. This formula gives larger value of κ when β is large. The constants κ_1 and κ_N are determined to keep the acceptance ratios in the basic algorithm within a reasonable range; this is usually around ~ 50%.

Using REM with these remarks, the mixing of MCMC for large or middle values of α becomes fast enough for the practical use of the method proposed in this part. It is, however, still difficult to treat the problem with smaller value of α, where MCMC does not mix well. Here, we employ the following trick that realizes a kind of annealing by decreasing α: First we run MCMC with the largest value of α, using REM that consists of parallel runs with different values of β. Then, we decrease the value of α sequentially using the same set of β, where each run of MCMC is initialized by a sample from the previous run with a larger α.

Although an artificial choice of initial conditions in this scheme is not fully justified from the spirit of MCMC, this method gives reasonable results in the following sections and is considered as a practical approach to the problem. A better founded solution may be obtained with some improved version of REM, which is left for future studies.

6.3 Estimation of hyperparameters

Estimation using log-derivatives of marginal likelihood

Here, we explain how to utilize the output of MCMC to estimate hyperparameters. In an empirical Bayes procedure, hyperparameters are estimated through a maximization of the marginal likelihood Eq. (5.20). The marginal likelihood cannot be directly computed with samples from the posterior distribution $p(\mathbf{z}, \boldsymbol{\delta}|\mathbf{y})$. Log-derivatives of the marginal likelihood by hyperparameters, however, can be computed using MCMC, which is usually enough when searching for hyperparameters that maximize the marginal likelihood.

Taking log-derivatives of Eq. (5.20), we obtain

$$\frac{\partial \ln l(\mathbf{y}|\theta,\tau)}{\partial(\tau^2)} = -\frac{1}{2}\mathbb{E}_{\text{pos}}\left[||D\mathbf{z}||^2\right] + \frac{m}{2\tau^2}, \tag{6.13}$$

$$\frac{\partial \ln l(\mathbf{y}|\theta,\tau)}{\partial(1/\theta^2)} = -\frac{1}{2}\mathbb{E}_{\text{pos}}[\,||\mathbf{y}'(\boldsymbol{\delta}) - E(\mathbf{x}'(\boldsymbol{\delta}))\mathbf{z}\,||^2] + \frac{n\theta^2}{2}, \tag{6.14}$$

where $\mathbb{E}_{\text{pos}}[f]$ denotes the posterior average of a function f of $\mathbf{z}$ and $\boldsymbol{\delta}$ as

$$\mathbb{E}_{\text{pos}}[f] = \iint f(\mathbf{z},\boldsymbol{\delta})p(\mathbf{z},\boldsymbol{\delta}|\mathbf{y})\,d\mathbf{z}d\boldsymbol{\delta}. \tag{6.15}$$

Thus, computing the log-derivatives of the marginal likelihood is reduced to calculating the posterior averages, which can be treated by MCMC.

Log-derivatives of marginal likelihood with respect to α and β

As discussed in the previous section, it is natural to use the hyperparameters α and β defined by Eq. (6.6), instead of θ and τ. To maximize the marginal likelihood with respect to α and β, we can use the relations

$$\frac{\partial \ln l(\mathbf{y}|\theta,\tau)}{\partial\alpha} = \frac{1}{\beta}\frac{\partial \ln l(\mathbf{y}|\theta,\tau)}{\partial(\tau^2)} - \frac{1}{\alpha^2\beta}\frac{\partial \ln l(\mathbf{y}|\theta,\tau)}{\partial(1/\theta^2)}, \tag{6.16}$$

$$\frac{\partial \ln l(\mathbf{y}|\theta,\tau)}{\partial \beta} = -\frac{\alpha}{\beta^2}\frac{\partial \ln l(\mathbf{y}|\theta,\tau)}{\partial(\tau^2)} - \frac{1}{\alpha\beta^2}\frac{\partial \ln l(\mathbf{y}|\theta,\tau)}{\partial(1/\theta^2)}. \tag{6.17}$$

An example of estimation of hyperparameters using Eqs. (6.13) – (6.17) will be shown in Sec. 7.1.1.

Chapter 7

Numerical experiments and analysis of experimental data

7.1 Numerical experiments

7.1.1 Examples

Designs of numerical experiments

In this section, we test the proposed method with artificial data generated by a neuron model. Here we employ the noisy Morris-Lecar equation [Morris and Lecar, 1981] as a source of artificial data; this is a bivariate stochastic differential equation widely used in neural science. The details of the numerical experiments are discussed in appendix B.

we show two examples of the estimation of PRC from sets of artificial data through the method in this part. The result of the method in this part is compared with the true PRC estimated with noiseless experiments.

The result is also compared with that of conventional Bayesian regression [Tanabe and Tanaka, 1983] with a smoothness prior, where the errors in the explanatory variable is ignored. This algorithm employs the same representation and smoothness prior of $Z(\cdot)$, but assumes the normal regression model (Eq.(3.2))

$$y_i = Z(x_i) + \varepsilon_i,\ \varepsilon_i \sim \mathcal{N}(0, \sigma^2).$$

It is similar to that proposed by the regression method [Ota et al., 2009b, Aonishi and

Ota, 2006], as discussed in Chap. 3. We call this algorithm as "spline regression". We also compare the method in part II with Fourier regression [Galán et al., 2005], which is discussed in Chap. 3. In this thesis, the spline regression and the Fourier regression are called conventional regression.

To apply the conventional regression, the value x_i of the explanatory variable should satisfy the relation $x_i < 2\pi$. This means that we should discard samples with $x_i \geq 2\pi$ when we apply the conventional regression. In the following experiments using artificial data, we remove such samples from the input of the conventional regression; to keep the number of samples and make the comparison fair, an equal number of new samples that satisfying $x_i < 2\pi$ is generated and added to the input data.

The sets of artificial data used here contain $n = 100$ samples, where the timing of perturbation $\{t_i\}_{i=1}^{n}$ is randomly chosen. The level s of the noise are 0.3 (high) and 0.1 (low); details are explained in appendix B). The estimates of mean and variance of periods are $\hat{T} = 44.2$ and $\hat{\sigma_T} = 6.4$ for the high noise level $s = 0.3$, and $\hat{T} = 45.3$ and $\hat{\sigma_T} = 2.3$ for the low noise level $s = 0.1$, respectively. These are estimated with a simulation with the noisy neuron model where we do not input perturbations.

Estimation of hyperparameters

Let us start with estimation of the hyperparameters α and β. First, the log-derivative Eq. (6.17) of the marginal likelihood with respect to β is plotted with a set of values of β, as shown in the left panel of Fig. 7.1 for the high noise level $s = 0.3$ and Fig. 7.2 for the low noise level $s = 0.1$. Each curve corresponds to a value of α in a given set $\{\alpha_l\}$. Then, we estimate the zero crossing of each curve, which we denote $\beta^*(\alpha_l)$. Next, for each value of $\beta^*(\alpha_l)$, we plot the log-derivative Eq. (6.16) of the marginal likelihood with respect to α for the values of $\alpha \in \{\alpha_l\}$, as shown in the right panel of Fig. 7.1 and Fig. 7.2. The zero crossing of this curve gives the estimate $\hat{\alpha}$ of α. The estimate $\hat{\beta}$ of β is also obtained as $\beta^*(\hat{\alpha})$. In the right panel of Fig. 7.1, the zero crossing is located near $\alpha = 7$, and we choose $\hat{\alpha} = 8$ as a rough estimate of α among the five values that we have tested here. In the right panel of Fig. 7.2, the zero crossing of the curve is located at $\alpha = 4.5$. The values of β for the low and high noise levels are estimated as the same $\hat{\beta} = \beta^*(8) \simeq 0.00074$.

In the above procedure, we assume that the zero point is unique. It is possible to introduce more sophisticated iterative procedures to find zeros, a rough estimate of α and β is usually enough for the purpose estimating the PRC $Z(\cdot)$.

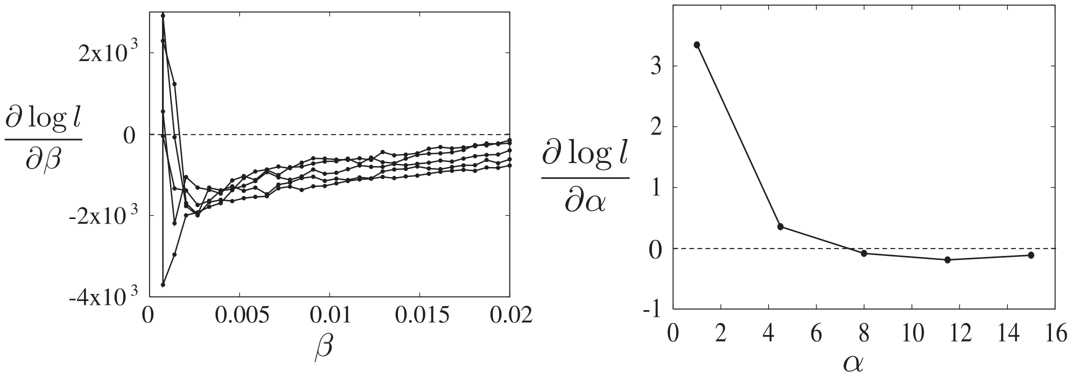

Figure 7.1: Log derivatives of marginal likelihood for artificial data (high noise level $s = 0.3$) with respect to hyperparameters α and β. Details are explained in the text. The five curves in the left panel correspond to $\alpha = 1, 4.5, 8, 11.5$, and 15.

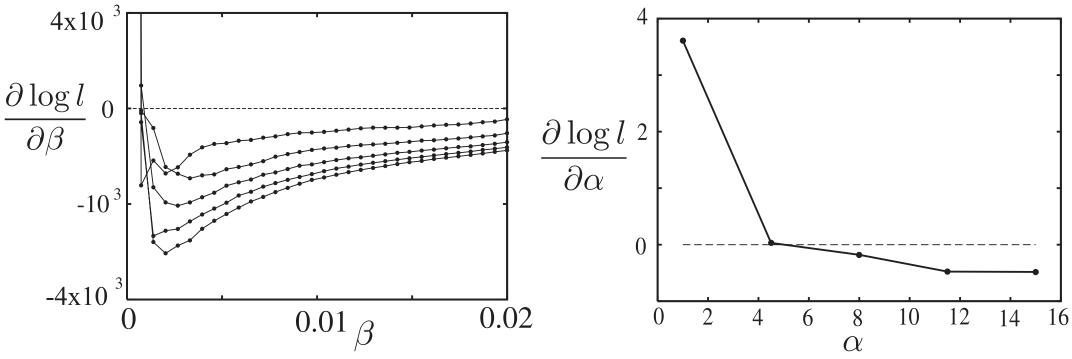

Figure 7.2: Log derivatives of marginal likelihood for artificial data (high noise level $s = 0.1$) with respect to hyperparameters α and β. Details are explained in the text. The five curves in the left panel correspond to $\alpha = 1, 4.5, 8, 11.5$, and 15.

Estimation of PRCs

The upper left panels of Fig. 7.3 for the high noise level $s = 0.3$ and Fig. 7.4 for the low noise level $s = 0.1$ show the PRCs estimated with the method in this part using the hyperparameters $\hat{\alpha}$ and $\hat{\beta}$ as defined above. For comparison, the upper right panels of Fig. 7.3 and Fig. 7.4 show the PRCs estimated with the spline regression. The hyperparameters of the spline regression are also determined by maximizing the corresponding marginal likelihood, where θ^2 is analytically optimized and $\hat{\alpha} = 40$ is found by a grid search (see Appendix. A). The result with the Fourier regression is also shown in the lower panel; the dataset used in the Fourier regression are the same as that used in the spline regression.

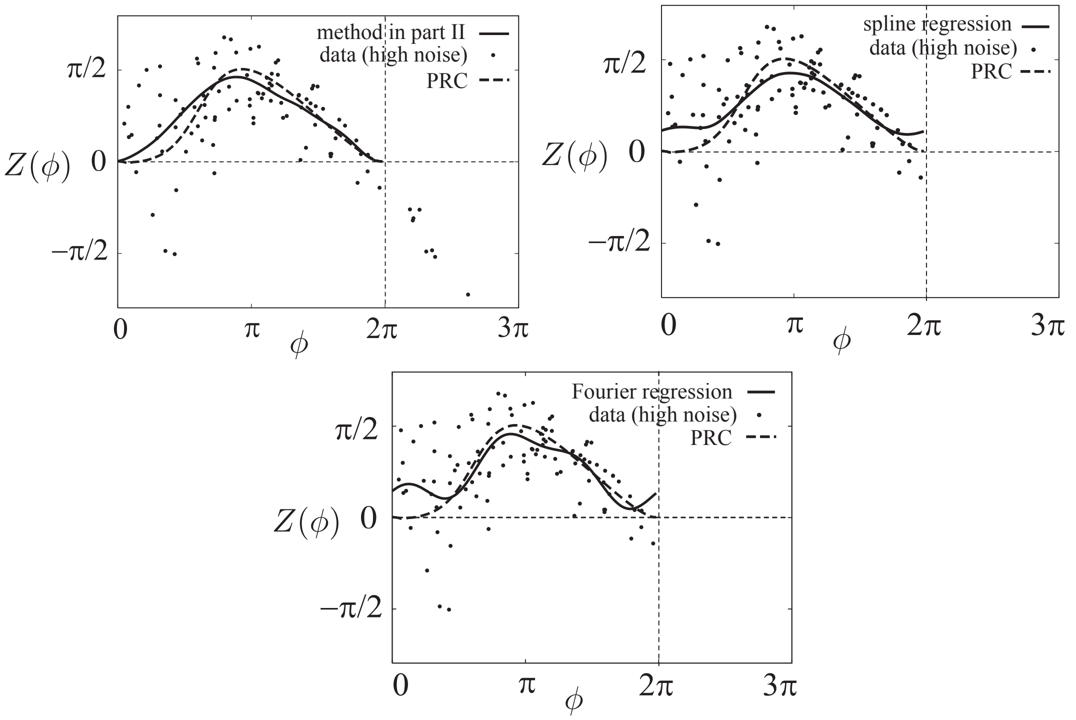

Figure 7.3: Comparison between the method in this part and conventional methods using artificial data (high noise level$s = 0.3$). In this example, the data point (x_i, y_i) whose value $x_i \geq 2\pi$ does not exist. The solid curve corresponds to the PRC estimated from samples shown by black dots, and the broken curve shows the true PRC estimated with noiseless simulation. The upper left and upper right panels correspond to the method in this part and the spline regression, respectively; the result with the Fourier regression is also shown in the lower panel. Differences in the samples shown in the upper left and upper right (or lower) panels are explained in the text.

In each panel of Fig. 7.3 and Fig. 7.4, a solid curve shows the estimate, while a broken curve shows the true PRC. In Fig. 7.3 (high noise level), the solid curve is closer to the broken curve in the upper left panels than the one in the upper right panel. On the other hand, in Fig. 7.4 (low noise level), all solid curves are close to the broken curves. These suggest that the method in this part outperforms the spline regression for this set of data for

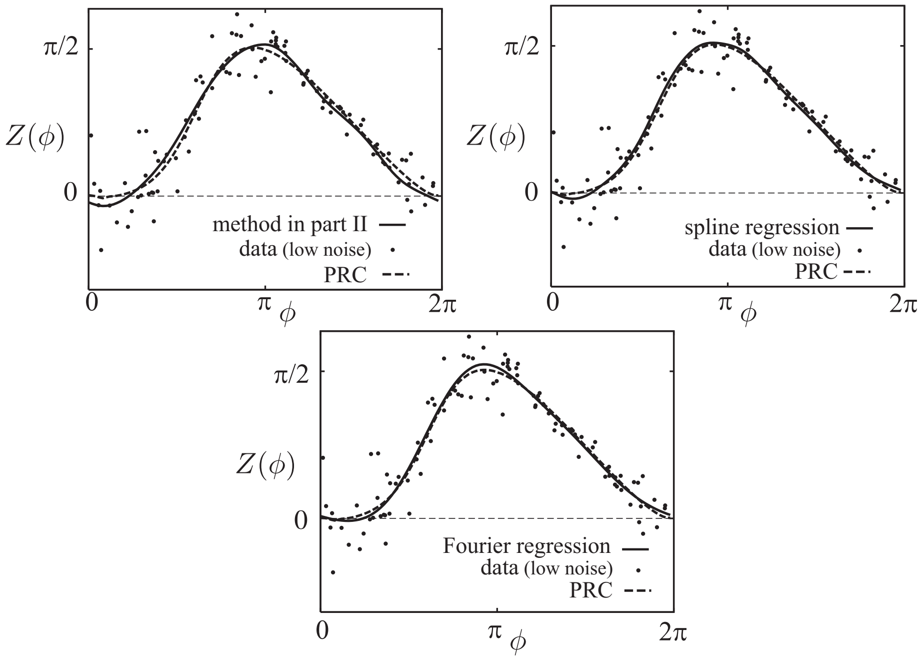

Figure 7.4: Comparison between the method in this part and conventional methods using artificial data (low noise level$s = 0.1$). In this example, the data points (x_i, y_i) whose values $x_i \geq 2\pi$ exist; we remove the data points in case of the spline and Fourier regressions. The details are explained in the text.

the high noise level $s = 0.3$. The method is also better than the Fourier regression in this example.

The details of the algorithm used in computing the above result are as follows. The number m of the pieces of the discretized curve $Z(\cdot)$ is 100 and the periodic boundary condition is assumed. The number of replicas N used in REM is 32, and the number N_{MC} of iterations per replica is 10^6. We try to exchange neighboring pairs of replicas once within 20 iterations. The variance κ_k of the proposal distribution in the kth replica is defined by Eq. (6.12), where $\kappa_1 = 0.01$ and $\kappa_N = 0.07$; this is independent of α.

We make use of the advantage of REM in parallel computation. Computation time on 32 cores(16CPU) of AMD Opteron 252(2.6GHz) is about 6 hours for each dataset ($N = 100$), including hyperparameter search on a 5×32 grid on the (α, β) plane; it reduces to about $1/3$ on faster hardware with 32 cores(4CPU) of Intel Xeon X5570(2.93GHz). Intel C++ compiler, MPI and LAPACK are used for the computation.

7.1.2 Statistical comparison using average L^2 error

In Sec. 7.1.1, we apply the method in this part to two sets of artificial data. Here, we consider sets of simulation data and compare the method in this part with the spline regression and the Fourier regression using the average L^2 error defined by

$$\sum_{w=1}^{N_D} \left(\int_0^{2\pi} (Z(\phi) - Z^{[w]}(\phi))^2 d\phi \right)^{1/2}, \tag{7.1}$$

where the number of the datasets is N_D and the curve estimated from the wth dataset is denoted by $Z^{[w]}(\phi)$.

We consider seven sets of data with different levels of external noise $s = 0.1, 0.15, 0.2, 0.25, 0.3, 0.35$, and 0.4. For each value of s, we consider the average over $N_D = 100$ sets of artificial data for the method in this part, and $N_D = 500$ sets of artificial data for the spline regression and the Fourier regression, respectively. Each set is generated by a simulation with a different random number sequence. The estimates of $\hat{T}$ and $\hat{\sigma_T}$ are shown in Table 7.1 with the level s of noise.

s	$\hat{T}$	$\hat{\sigma_T}$	$\hat{\sigma_T}/\hat{T}$
0.1	45.3	2.3	0.05
0.15	44.9	3.6	0.07
0.2	45.0	4.8	0.11
0.25	44.6	5.4	0.12
0.3	44.2	6.4	0.15
0.35	44.2	7.5	0.17
0.4	43.7	7.8	0.18

Table 7.1: $\hat{T}$ and $\hat{\sigma_T}$ from artificial data.

The hyperparameters α and β are estimated from each set of data by the method explained in the previous sections. The parameters used for the method are the same as those defined in the previous subsection, except that the estimated value of α is considerably large at $s = 0.35, 0.4$ and search in a larger hyperparameter space is required in the case.

Figure 7.5 shows the average L^2 errors for the method in this part (solid curve), for the spline regression (broken curve), and for the Fourier regression (chain curve); the horizontal axis corresponds to the normalized standard error $\hat{\sigma_T}/\hat{T}$, which gives a measure of the fluctuation of inter-spike intervals. The figure shows that the method in this part produces better results in the region $0.15 \le \hat{\sigma_T}/\hat{T}$.

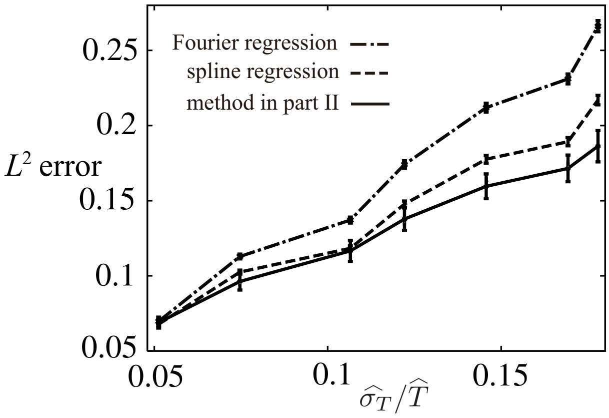

Figure 7.5: Comparison of the average L^2 errors.

7.1.3 Detail analysis with L^2 errors

Scatter plots

In this section, we present a detailed comparison between the method in part II and the spline or Fourier regression using the L^2 errors. To see raw data of the L^2 errors in the previous section, scatter plots of the L^2 errors are presented in Fig. 7.6 and Fig 7.7. The horizontal axes in the panels correspond to the L^2 errors by the method in part II; the vertical axes in the panels of Fig. 7.6 and Fig. 7.7 correspond to the L^2 errors by the spline regression and Fourier regression, respectively. The panels in each figure correspond to the noise levels $s = 0.1, 0.15, 0.2, 0.25, 0.3, 0.35$ and 0.4, respectively. The point in the panels represents a set of artificial data; we plot $N_D = 100$ points obtained by the datasets of a noise level in each panel.

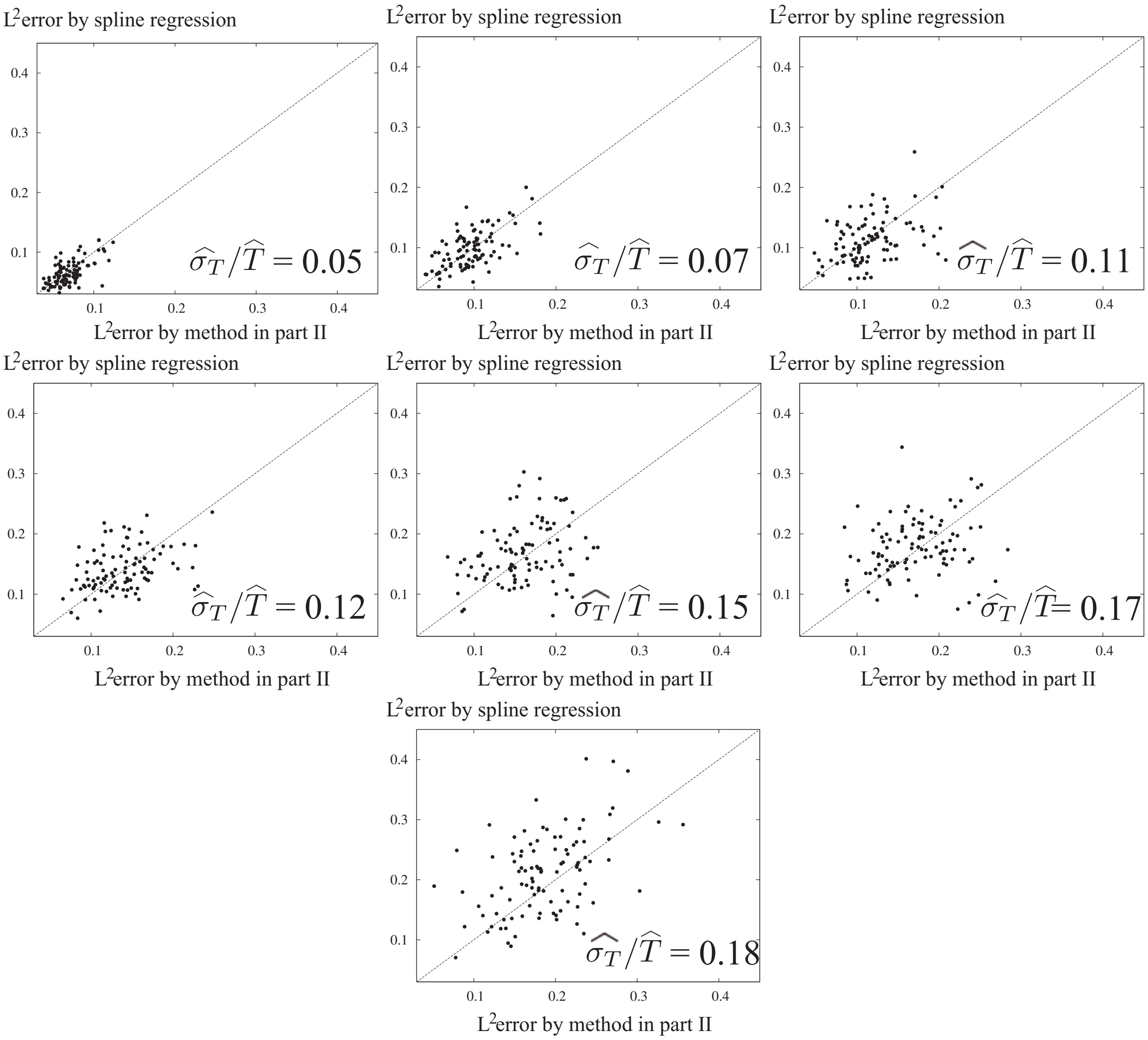

Figure 7.6: Scatter plots of L^2 errors by the method in part II (horizontal axis) and the spline regression (vertical axis).

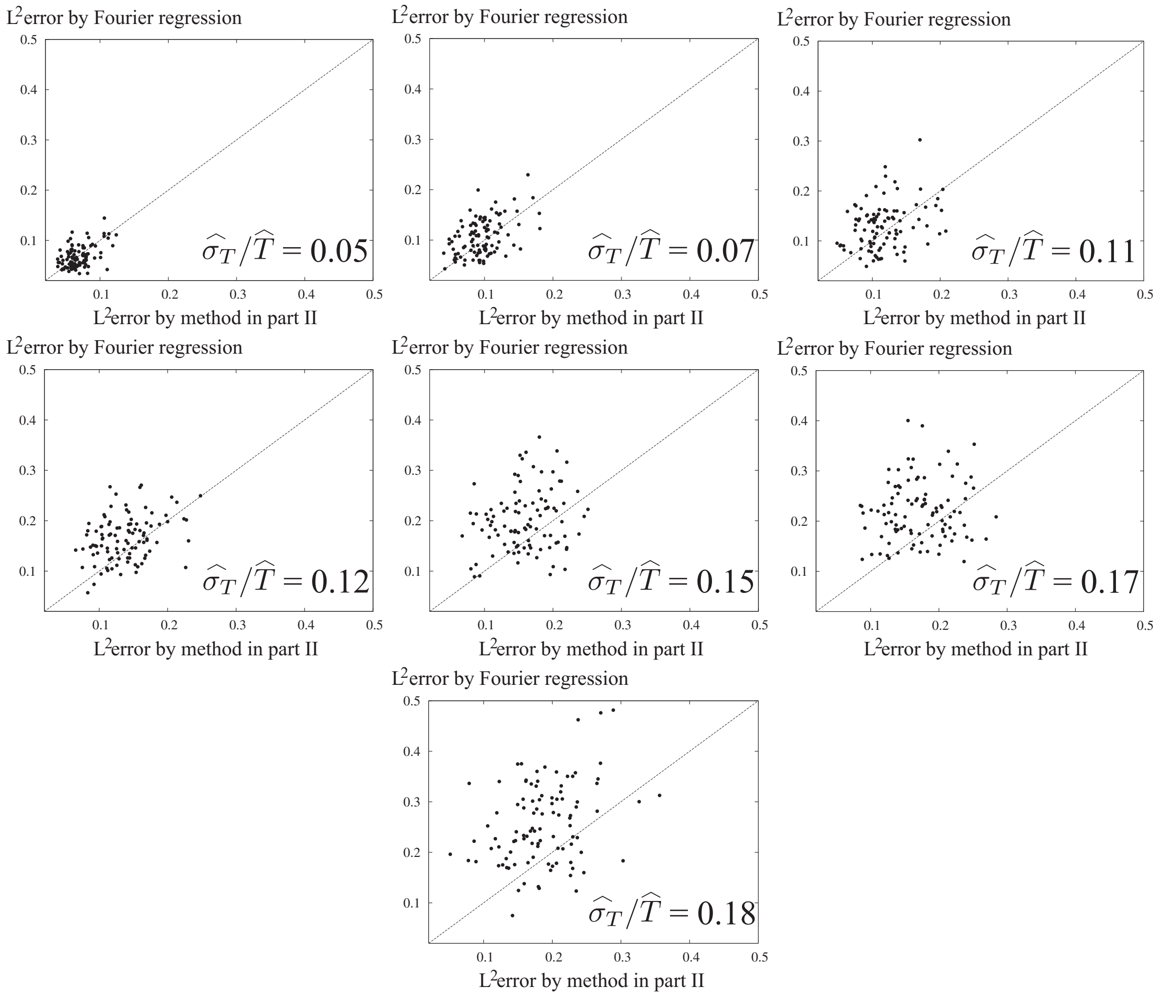

Figure 7.7: Scatter plots of L^2 errors by the method in part II (horizontal axis) and the Fourier regression (vertical axis).

Win rates

To compare the differences of the L^2 accuracy, we estimate win rates of the method in part II to conventional regressions using the datasets. Here, we define $\{Y_w\}_{w=1}^{N_D}$ as

$$Y_w = \begin{cases} 1 & \text{the method in part II outperforms another method for } w\text{-th dataset,} \\ 0 & \text{otherwise,} \end{cases} \tag{7.2}$$

and assume that Y_w follows an i.i.d. binomial distribution. The win rate corresponds to the population rate p of the binomial distribution where the estimate $\hat{p}$ is $\sum_{w=1} Y_w/N_D$. Using the normal approximation, we calculate the 95 % confidence interval of $\hat{p}$ as $[\hat{p} - 1.96\sqrt{\hat{p}(1-\hat{p})/N_D}, \hat{p} + 1.96\sqrt{\hat{p}(1-\hat{p})/N_D}]$. Note that the approximation is valid when p is near 0.5 and N_D is sufficently large.

In Fig. 7.8, we present the estimates of the win rates and the confidence intervals with respect to the normalized variance $\hat{\sigma}_T/\hat{T}$. The left and right panels represent the win rates of the method in part II to the spline and Fourier regressions, respectively.

The left panel shows that the method in part II outperforms the spline regressions significantly above chance for $\hat{\sigma}_T/\hat{T} \geq 0.17$; the right panel shows that the method in part II outperforms Fourier regressions significantly above chance except for $\hat{\sigma}_T/\hat{T} = 0.05$ and 0.11. When $\hat{\sigma}_T/\hat{T}$ is 0.05 in the left and right panels, the win rate p is smaller than 0.5. This is possibly because of rough estimation of the hyperparameters α and β in the method in part II.

Box and whisker plots

Here, we show the difference between the method in part II and the conventional methods in more detail. We show box and whisker plots [Tukey, 1977] of differences from the L^2 errors by the spline regression to those by the method in part II in the left panel of Fig. 7.9. The vertical and horizontal axes correspond to the difference and the normalized variance $\hat{\sigma}_T/\hat{T}$ in the previous section, respectively. Each box and whisker plot represents five-number summaries of the differences: sample minimum, lower quantile, median, upper quantile, and sample maximum. Note that lower and upper edges of the box do not represent confidence interval of the median but lower and upper quantiles, respectively.

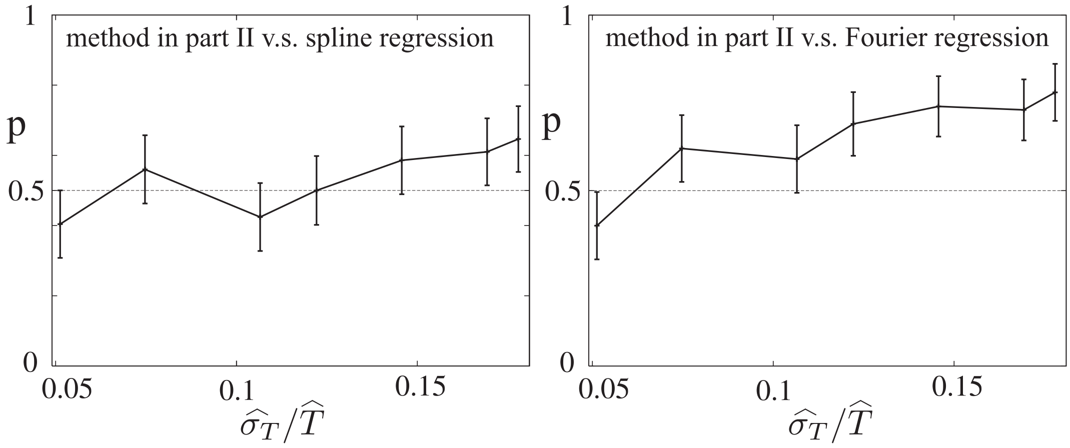

Figure 7.8: Estimates of the win rates of the method in part II to the spline (left panel) and Fourier (right panel) regressions with respect to $\hat{\sigma}_T/\hat{T}$. The error bars represent the 95 % confidence intervals by normal approximation.

When the median of the differences is above zero, the method in part II outperforms the spline regression for over half of the datasets. The box and whisker plots in the left panel of Fig. 7.9 suggest it when $\hat{\sigma}_T/\hat{T} \geq 0.15$; this result is consistent with the result through the average L^2 error in the previous section.

The right panel of Fig. 7.9 represents box and whisker plots of differences from the L^2 errors by Fourier regression to those by the method in part II. This panel means that the method in part II outperforms Fourier regression for over half of the datasets except for $\hat{\sigma}_T/\hat{T} = 0.05$. The quantiles of the box and whisker plots suggest that the method in part II outperforms Fourier regression for about 75 % of the datasets when $\hat{\sigma}_T/\hat{T} \geq 0.15$

7.2 Analysis of experimental data

7.2.1 Experimental data

We test the method with experimental data recorded from the pyramidal cells of in rat motor cortex. Two sets of data, hereafter denoted by A and B, are obtained using whole-cell patch-clamp recordings at the somata of layer-5 pyramidal neurons in rat motor cortex. Details of the experiments are found in the paper [Tsubo et al., 2007a]. The parameters $\hat{T}$

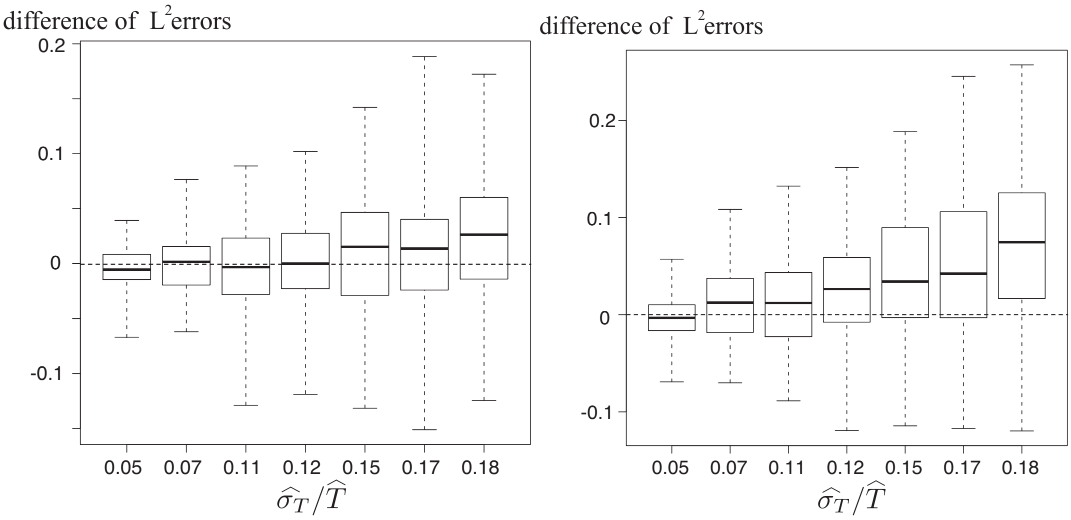

Figure 7.9: Box and whisker plots of the differences of L^2 errors with respect to $\hat{\sigma}_T/\hat{T}$. The differences from the spline and Fourier regressions to the method in part II are presented in the left and right panels, respectively. The line, upper edge and lower edge in each box represent the median, upper quantile and lower quantile, respectively. The upper and lower edges of each whisker represent the sample minimum and maximum, respectively.

and $\hat{\sigma_T}$ estimated from the experimental data are shown in Table 7.2 as well as the number n of samples.

dataset	n	$\widehat{T}$ (ms)	$\widehat{\sigma_T}$ (ms)	$\widehat{\sigma_T}/\widehat{T}$
A	435	34.9	2.8	0.08
B	440	64.3	9.4	0.15

Table 7.2: $\hat{T}$ and $\hat{\sigma_T}$ from experimental data.

We use parameters for the algorithm that are essentially the same as those used in Sec. 7.1.1. In this analysis of experimental data, however, we add the condition $Z(0) = 0$ and use the prior Eq. (5.19) instead of Eq. (5.17), for both the method in this part and the spline regression. Unlike as in the case of artificial data, the points $x_i \geq 2\pi$ are merely removed when the spline regression or the Fourier regression is applied.

The hyperparameters α and β are estimated in the same manner as that explained in Sec. 7.1.1. In the left panels of Fig. 7.10, the log-derivative Eq. (6.17) of the marginal likelihood with respect to β is plotted with the values of β. Each curve corresponds to a value of α. The zero crossing $\hat{\beta}$ is almost independent of α in the range of $1 \leq \alpha \leq 15$ in both datasets. Fixing the value of β to $\hat{\beta}$, we then plot the log-derivative Eq. (6.16) of the marginal likelihood with respect to α as shown in the right panels of Fig. 7.10. The resultant estimates of hyperparameters are $\hat{\alpha} = 4.5$ and $\hat{\beta} = 0.00058$ for dataset A and $\hat{\alpha} = 4.5$ and $\hat{\beta} = 0.00074$ for dataset B. The hyperparameters of the spline regression are also estimated by maximizing marginal likelihood.

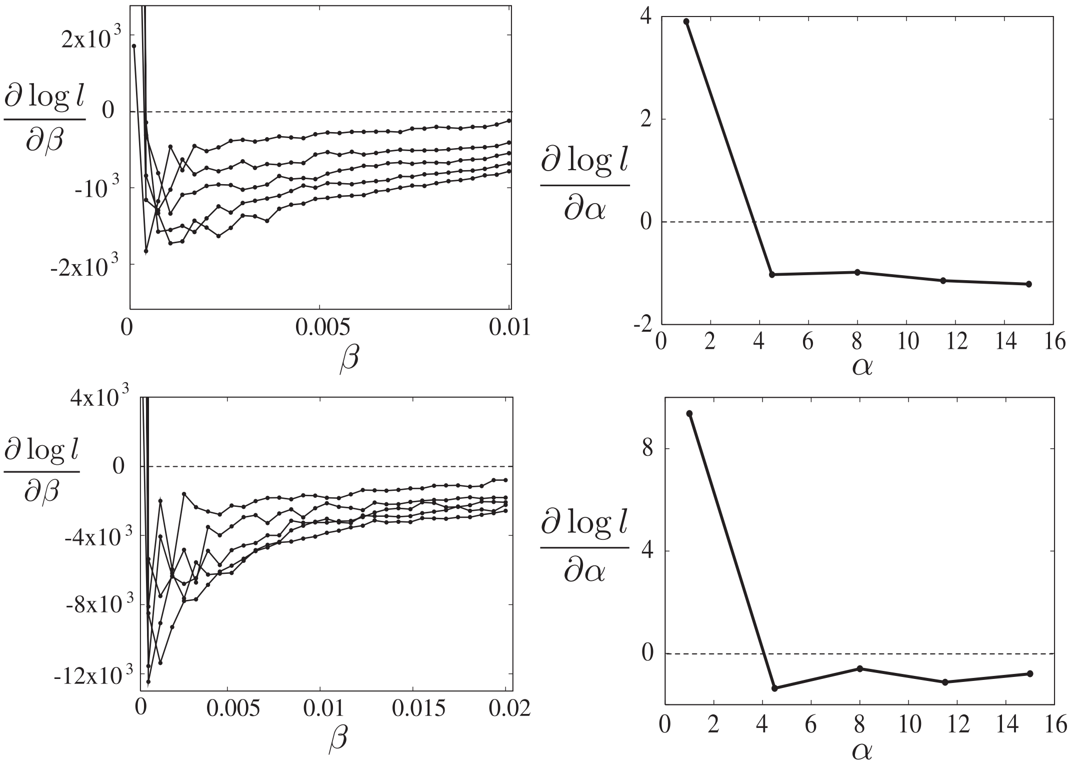

Figure 7.10: Log derivatives of the marginal likelihood with respect to hyperparameters α and β (experimental data). Details are explained in the text. The five curves in the left panel correspond to $\alpha = 1, 4.5, 8, 11.5$, and 15. The upper and lower panels correspond to the datasets A and B, respectively.

The PRCs estimated with these hyperparameters are shown in Fig. 7.11. The left and right panels of Fig. 7.11 correspond to the datasets A and B, respectively. In each panel, the solid curve shows the PRC estimated with the method in this part, and the broken curve shows the PRC estimated with the spline regression or the Fourier regression. Samples in the datasets are shown by black dots. Computation time on 32cores(16CPU) of AMD

Opteron 252(2.6GHz) is about 49 hours for each dataset ($N = 435$), including hyperparameter search on the (α, β) plane.

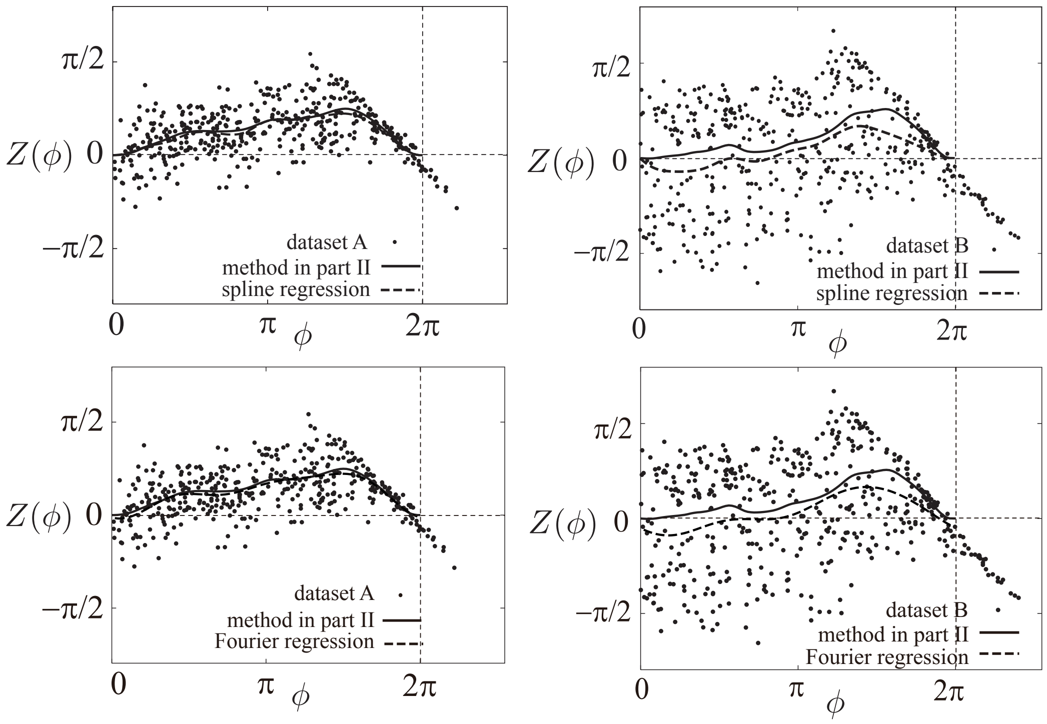

Figure 7.11: Comparison between the method in this part and conventional methods using experimental data. The upper panels show comparison to the spline regression, while the lower panels show comparison to the Fourier regression. The left and right panels correspond to the datasets A and B, respectively. In each panel, the solid curve shows the result of the method in this part and the broken curve shows the result of a conventional method; both are almost overlapped in the left panels. The black dots are samples.

The results shown in the left panels of Fig. 7.11 indicate that there is no significant improvement with the method in this part for dataset A, where the value of $\hat{\sigma_T}/\hat{T}$ is small. On the other hand, in the right panels, where the value of $\hat{\sigma_T}/\hat{T}$ is larger, considerable differences are observed. This result implies the utility of the method in this part when the normalized variance $\hat{\sigma_T}/\hat{T}$ is large.

7.2.2 Analysis of synchronization property

Finally, we compare synchronization properties based on the estimates of the PRC from the experimental data. As discussed in Sec. 2.2, we analyze a system of two symmetrically connected neurons whose PRCs are the same. Using the function $\Gamma^{-}(\phi) = \Gamma(\phi) - \Gamma(-\phi)$, we can determine stabilities of in-phase, anti-phase and out-of-phase synchronization between the two neurons. The coupling function $\Gamma(\phi)$ is defined by Eq. (2.14)

$$\Gamma(\phi) = \frac{1}{2\pi}\int_0^{2\pi} \hat{Z}(\theta)\left\{-g_{\text{syn}}(\hat{v}^*(\theta) - v_{\text{syn}})\alpha_T^*(\theta+\phi)\right\} d\theta,$$

where the estimate of the PRC of the neuron is $\hat{Z}(\theta)$, the estimate of the normalized activity of the voltage is $\hat{v}^*(\theta)$, and the normalized effect of spikes from another neuron is $\alpha_T^*(\theta) = \alpha_T(\theta/\omega_0)$ defined by Eq. (2.13). Here, we set $g_{\text{syn}} = 1$, $v_{\text{syn}} = 0$, and $\tau = 2$ in the function $\alpha_T^*(\theta)$ because we assume the excitatory connection between the two neurons. We estimate the normalized voltage $v^*(\theta)$ by averaging time series of the voltage in inter-spike intervals, whose periods are normalized from 0 to 2π. The normalized voltages for dataset A and B are shown in the left and right panel in Fig. 7.12, respectively.

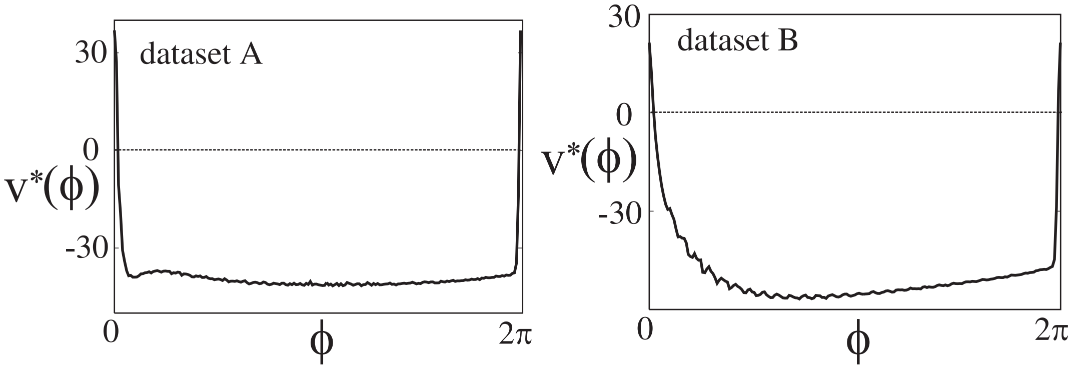

Figure 7.12: Normalized voltage $v^*(\phi)$ estimated from the time series of the voltage in experiments. The left and right panel represents the normalized voltage of the neuron for dataset A and dataset B, respectively.

For dataset A, we show the functions $\Gamma^{-}(\Delta\phi)$ computed from the estimates through the method proposed in part II, the spline regression, and Fourier regression in the upper-left, upper-right and lower panels of Fig. 7.13, respectively. The points and the circles mean the stabilities and the instabilities of equilibrium points of the phase difference $\Delta\phi = \phi_1 - \phi_2$ between the two neurons, respectively. Figure. 7.13 shows that two neurons are synchronized at out-of-phase for all these estimates. This result is consistent with the fact that these estimates of the PRC for dataset A are considered as Type-I PRCs.

For dataset B, we show the functions $\Gamma^{-}(\Delta\phi)$ computed from these estimates of the PRC in Fig. 7.14. The points and the circles also represent the stabilities and the instabilities. The upper-left panel, which corresponds to the estimate through the method in part II, shows that the two neurons are synchronized at out-of-phase. This result is also consistent with the facts that the estimates through the method in part II is considered as the Type-I PRC. The upper-right panel, which corresponds to the estimate through the spline regression, shows that the two neurons are synchronized at in-phase. The lower panel, which corresponds to the estimate through Fourier regression, shows that the two neurons are synchronized at out-of-phase. It seems strange that synchronization properties computed form the estimates are different, although the estimates of the spline and Fourier regression are close. This is because we do not assume $Z(0) = 0$ in the Fourier regression; on the other hand, we assume $Z(0) = 0$ in the spline regression and the proposed method.

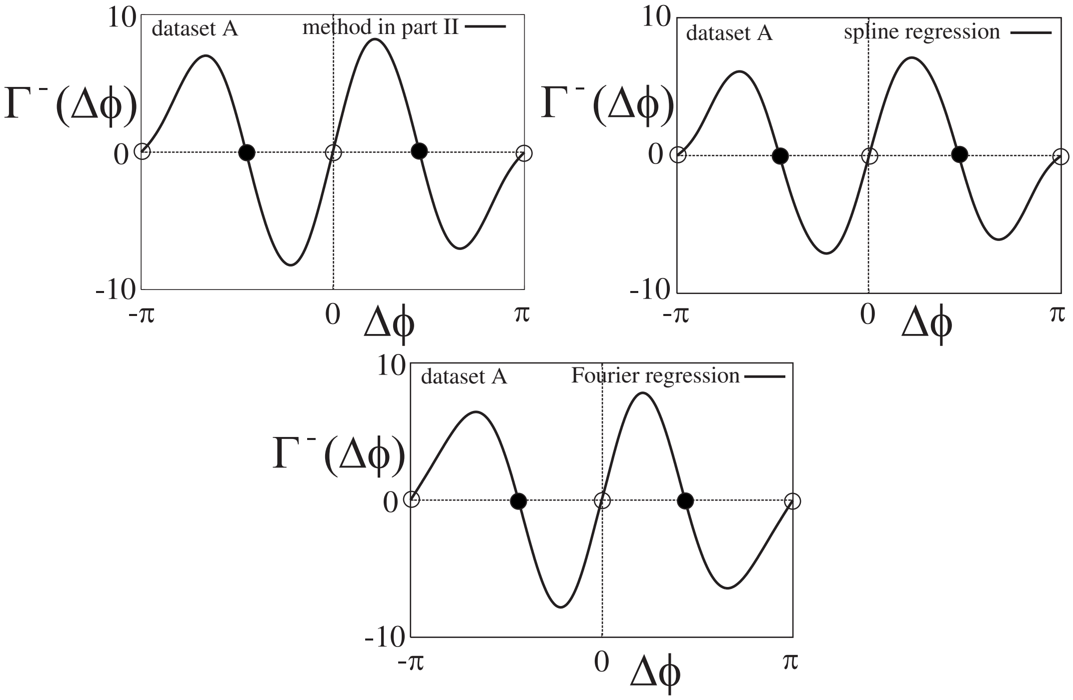

Figure 7.13: The function $\Gamma^{-}(\phi)$ for analyzing synchronicity of two symmetric connected neurons. The upper-left, upper-right and lower panels represents the function obtained through the PRCs estimated by Fourier regression, spline regression and the method in part II for dataset A. The point and the circle shows that the equilibrium points are stable and unstable.

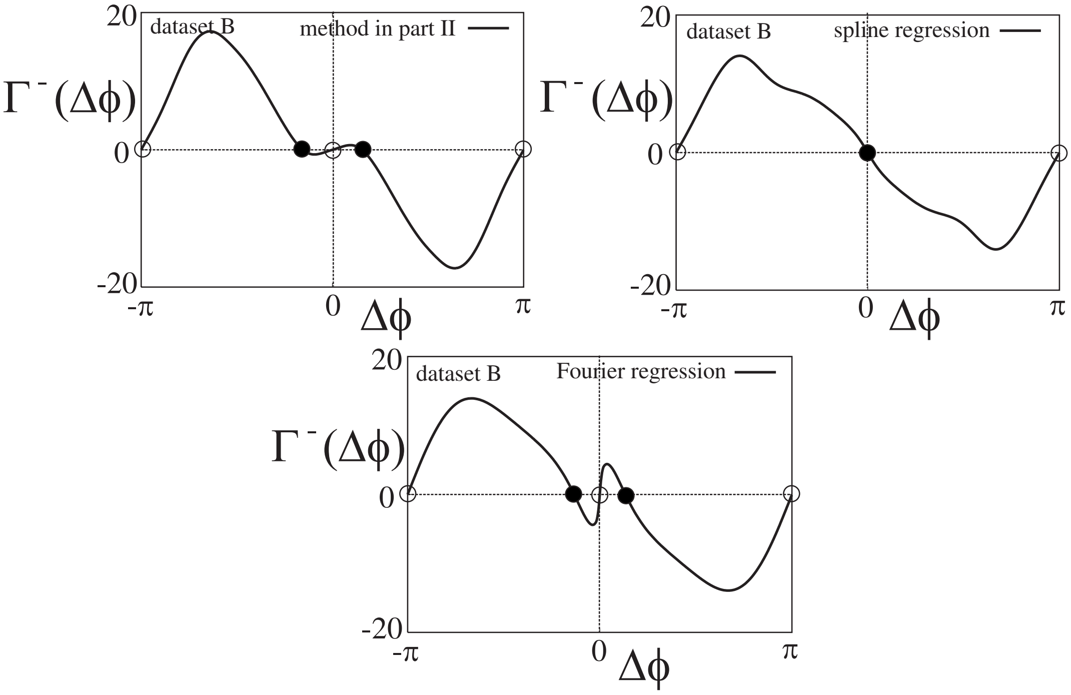

Figure 7.14: The function $\Gamma^{-}(\phi)$ for analyzing synchronicity of two symmetric connected neurons. The upper-left, upper-right and lower panels represents the function obtained through the PRCs estimated by Fourier regression, spline regression and the method in part II for dataset B. The point and the circle shows that the equilibrium points are stable and unstable.

Part III

Statistical estimation of phase response curves using data transformation

Chapter 8

Estimation using data transformation

8.1 Introduction

The method proposed in part II deals with a correlation between errors in the PRC explanatory and response variables. The correlation is neglected in the previous studies, as discussed in Chap. 3. We showed that the method in part II gives a better accuracy than the conventional regression for the data generated by the Morris-Lecar equations.

However, parallel computing environments are necessary for actual use of the method in part II. Without parallel computing, computation time of the method will be about $32 \times 2 = 64$ hours for the example ($n = 100$) in Sec. 7.1.1, because computation time on 32 cores is approximately 2 hours. Even now, everyone can not use massive parallel computing environments. For actual use, we need more efficient method to deal with the correlation.

In this part, we propose a novel method that deals with the correlation and takes considerably lesser time than the method in part II. To achieve this, we introduce a transformation that mixes the explanatory and response variables. After the data are transformed, no error exists in the explanatory variable and the correlation is removed in the transformed data. Hence, an estimation of the PRC is reduced to a normal regression.

8.2 Statistical model in part III

In part II, the correlation is represented by the observation model Eqs. (5.5) and (5.6)

$$x_i = \phi_i + x_i\delta_i, \tag{8.1}$$

$$y_i = Z(\phi_i) + (y_i - 2\pi)\delta_i + \xi_i, \qquad i = 1, \dots, n, \tag{8.2}$$

where ξ_i follows a normal distribution. In Eq.(5.3), the error δ_i is a function of a realization T_i of the period, where $\delta_i = (T_i - \hat{T})/T_i$. Using a prior Eq.(5.14), we assumed $T_i \sim$ a truncated normal distribution in part II.

Here, we define $\nu_i = (1 - \delta_i)^{-1}$, and rewrite the observational model as

$$x_i = \phi_i\nu_i, \tag{8.3}$$

$$y_i = (Z(\phi_i) + \xi_i - 2\pi)\nu_i + 2\pi, \qquad i = 1, \dots, n. \tag{8.4}$$

To simplify the model, we assume $\xi_i = 0$ and obtain

$$x_i = \phi_i\nu_i, \tag{8.5}$$

$$y_i = (Z(\phi_i) - 2\pi)\nu_i + 2\pi, \qquad i = 1, \dots, n. \tag{8.6}$$

In this part, we assume $T_i \sim$ a log normal distribution. Here, the distribution of $\ln \nu_i$ is represented by

$$\ln \nu_i \sim \mathcal{N}(0, \lambda^2), \tag{8.7}$$

where the variance of $\ln \nu_i$ is denoted by λ^2. In this part, we estimate the PRC $Z(\phi)$ based on the model Eqs. (8.5), (8.6), and (8.7).

A graphical interpretation of this model is shown in the left panel of Fig. 8.1. The solid curve represents the PRC $Z(\phi)$ of the model. The model indicates that the data point (x_i, y_i) is generated from the point $(\phi_i, Z(\phi_i))$ by shifting the broken line.

The model also indicates that the broken line passes the point $(0, 2\pi)$ for all data point (x_i, y_i); i.e. three points $(0, 2\pi)$, (x_i, y_i) and $(\phi_i, Z(\phi_i))$ lie on the line. Using Eqs. (8.5) and (8.6), the slope of the straight line joining $(0, 2\pi)$ and (x_i, y_i) is calculated as

$$\frac{2\pi - y_i}{0 - x_i} = \frac{2\pi - \{(Z(\phi_i) - 2\pi)\nu_i + 2\pi\}}{-\phi_i \nu_i} = \frac{2\pi - Z(\phi)}{0 - \phi_i}. \tag{8.8}$$

Therefore, the slope is equal to that of the straight line joining $(0, 2\pi)$ and $(\phi_i, Z(\phi))$. This means that the three points lies on the same straight line.

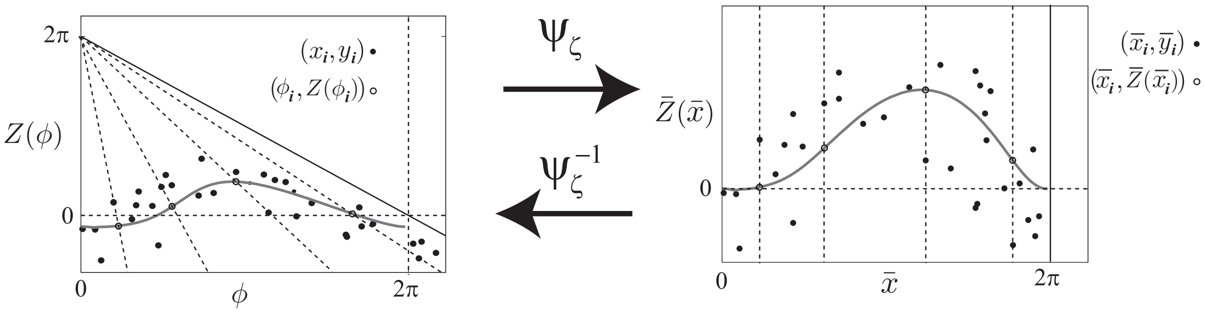

Figure 8.1: Procedure of estimating the PRC by using the transformation ψ_ζ. The left panel shows how the data point (x_i, y_i) is generated from the PRC represented by the solid curve. Using the transformation ψ_ζ, we can show that the points $(\bar{x}_i, \bar{y}_i)$ in the right panel are generated from the circle $(\bar{x}_i, \bar{Z}(\bar{x}_i))$ through the broken line parallel to the vertical axis.

8.3 Rough sketch of the estimation using data transformation

Here, we give a rough sketch of the data transformation using Fig. 8.1. We discuss the details of this method in the next section.

First, we define the transformation

$$\psi_\zeta(x, y) = \left(\frac{2\pi - \zeta}{2\pi - y} x, \ln \frac{2\pi - \zeta}{2\pi - y} \right), \tag{8.9}$$

which is parameterized by $\zeta = Z(0)$. The tuning parameter ζ is fixed in this and the next sections, and is estimated in Sec. 8.6.

When the data point (x_i, y_i), the circle $(\phi_i, Z(\phi_i))$ and the broken line in the left panel are transformed by ψ_ζ, we obtain the points $(\bar{x}_i, \bar{y}_i)$, the circle $(\bar{x}_i, \bar{Z}(\bar{x}_i))$, and the broken line parallel to the vertical axis in the right panel. This implies the eliminations of an error in the explanatory variable and a correlation between the explanatory and response variables in the right panel. As a result, we can easily estimate a function $\bar{Z}(\bar{x})$, which is shown as the solid curve in the right panel from the transformed data $(\bar{x}_i, \bar{y}_i)$. Finally, the PRC $Z(\phi)$ is determined to transform the function $\bar{Z}(\bar{x})$ by the inverse of ψ_ζ.

8.4 Details of the estimation using the data transformation

In the following section, we explain the details of the estimation based on the model in this part (Eqs. (8.5), (8.6), and (8.7)).

When we transform both sides of Eqs. (8.5) and (8.6) by ψ_ζ, the transformed model is given by

$$\bar{x}_i = \frac{2\pi - \zeta}{2\pi - Z(\phi_i)} \phi_i, \tag{8.10}$$

$$\bar{y}_i = \ln \frac{2\pi - \zeta}{2\pi - Z(\phi_i)} - \ln \nu_i, \tag{8.11}$$

where $(\bar{x}_i, \bar{y}_i)$ is the transformed data $\psi_\zeta(x_i, y_i)$. The deterministic equation (Eq. (8.10)) indicates that a smooth function h, which satisfies $\phi_i = h(\bar{x}_i)$, exists under the condition

$$\forall \phi \in [0, 2\pi), \quad 2\pi - Z(\phi) + \phi Z'(\phi) > 0. \tag{8.12}$$

We substitute $\phi_i = h(\bar{x}_i)$ in Eq. (8.11), which is reduced to the normal regression model

$$\bar{y}_i = \bar{Z}(\bar{x}_i) + \bar{\nu}_i, \qquad \bar{\nu}_i \sim \mathcal{N}(0, \lambda^2), \tag{8.13}$$

where

$$\bar{Z}(\bar{x}) = \ln \frac{2\pi - \zeta}{2\pi - Z(h(\bar{x}))}, \quad \bar{\nu}_i = -\ln \nu_i. \tag{8.14}$$

We call the function $\bar{Z}(\bar{x})$ a transformed PRC in the following sections. Note that the transformed PRC $\bar{Z}(\bar{x})$ satisfies the three conditions: $\bar{Z}(\bar{x})$ has the fixed boundary point $\bar{Z}(0) = 0$, $\bar{Z}(\bar{x})$ is periodic in the domain $[0, 2\pi)$, and $\bar{Z}(\bar{x})$ is smooth except $\bar{x} = 0$.

We estimate the transformed PRC $\bar{Z}(\bar{x})$ from the transformed data $\{(\bar{x}_i, \bar{y}_i)\}$ based on the normal regression model (8.13). Details of the estimation are explained in the next section and appendix A. The transformed PRC is assumed to be estimated from the transformed data in this section.

Finally, the PRC $Z(\phi)$ is estimated to transform the estimate of $\bar{Z}(\bar{x})$ using the inverse of ψ_ζ

$$\psi_\zeta^{-1}(\bar{x}, \bar{y}) = \left(\bar{x}e^{-\bar{y}}, 2\pi - (2\pi - \zeta)e^{-\bar{y}}\right). \tag{8.15}$$

The equation $\psi_\zeta^{-1}(\bar{x}_i, \bar{Z}(\bar{x}_i)) = (\phi_i, Z(\phi_i))$ derived from Eqs. (8.10) and (8.14) suggests that the estimate of the PRC is equal to the true PRC if the estimates of the transformed PRC is equal to the true transformed PRC.

Note that the estimate of PRC may be a multi-valued function, although PRC is not a multi-valued function. This is because of the mixing of the variables $\bar{x}$ and $\bar{y}$ in the component $\bar{x}e^{-\bar{y}}$ in Eq. (8.15).

8.5 Estimation of the transformed phase response curve

In this section, the transformed PRC $\bar{Z}(\bar{x})$ is estimated for three conditions: $\bar{Z}(\bar{x})$ has the fixed boundary point $\bar{Z}(0) = 0$, $\bar{Z}(\bar{x})$ is periodic in the domain $[0, 2\pi)$, and $\bar{Z}(\bar{x})$ is smooth in the region $[0, 2\pi)$. The last condition is inconsistent with the previous assumption that the transformed PRC $\bar{Z}(\bar{x})$ is smooth except for $\bar{x} = 0$, but we simply neglect the inconsistency for a decrease in the computation time of the method in this part.

Bayesian frameworks are appropriate to deal with the three conditions. We can choose a prior distribution of the transformed PRC $\bar{Z}(\bar{x})$, which satisfies the conditions. When we define $\bar{\mathbf{y}}$ as $(y_1, \ldots, y_n)^T$, the likelihood function $p(\bar{\mathbf{y}}|\bar{Z}(\cdot), \lambda)$ is derived by Eq. (8.13). Then a posterior distribution $p(\bar{Z}(\cdot)|\bar{\mathbf{y}}, \lambda, \bar{\tau})$ is derived using the Bayes' theorem

$$p(\bar{Z}(\cdot)|\bar{\mathbf{y}}, \lambda, \bar{\tau}) = \frac{p(\bar{\mathbf{y}}|\bar{Z}(\cdot), \lambda)p(\bar{Z}(\cdot)|\bar{\tau})}{\int p(\bar{\mathbf{y}}|\bar{Z}(\cdot), \lambda)p(\bar{Z}(\cdot)|\bar{\tau})d\bar{Z}}, \tag{8.16}$$

where $p(\bar{Z}(\cdot)|\bar{\tau})$ is a density function of the smoothing prior [Aonishi and Ota, 2006, Ota et al., 2009b, Tanabe and Tanaka, 1983, Nakae et al., 2010] defined in appendix A. The tuning parameter $\bar{\tau}$ in the prior controls the degree of smoothness of the transformed PRC $\bar{Z}(\bar{x})$. When $\bar{\tau}$ is larger, the estimated curve becomes smoother.

In the Bayesian framework, the estimate of the transformed PRC $\bar{Z}(\bar{x})$ is an expectation of the posterior. The details of the estimation are discussed in appendix A.

8.6 Choice of the tuning parameters λ,$\bar{\tau}$ and ζ

The tuning parameters $\lambda, \bar{\tau}$ and ζ of the model, which we call “hyperparameters”, are fixed in the previous sections. The hyperparameters are estimated to maximize the log marginal likelihood

$$\ln p_\zeta(\bar{\mathbf{y}}|\lambda, \bar{\tau}) = \ln \int p_\zeta(\bar{\mathbf{y}}|\bar{Z}(\cdot), \lambda) p(\bar{Z}(\cdot)|\bar{\tau}) d\bar{Z}, \tag{8.17}$$

where $p_\zeta(\bar{\mathbf{y}}|\bar{Z}(\cdot), \lambda)$ is the likelihood in Eq. (8.16), which is dependent on $\zeta = Z(0)$.

When the hyperparameters $\lambda, \bar{\tau}$, and ζ are changed to the new hyperparameters $\lambda, \bar{\alpha}$ and ζ, where $\bar{\alpha} = \lambda\bar{\tau}$, the estimate of λ is analytically derived as $\hat{\lambda}(\bar{\mathbf{y}}, \bar{\alpha}, \zeta)$. To substitute $\hat{\lambda}$ into the log marginal likelihood, we consider only a maximization of $\ln p_\zeta(\bar{\mathbf{y}}|\bar{\alpha}, \hat{\lambda})$ over a plane of the hyperparameters $(\bar{\alpha}, \zeta)$. The details of the derivation are presented in appendix A.

We numerically maximize $\ln p_\zeta(\bar{\mathbf{y}}|\bar{\alpha}, \hat{\lambda})$ over a region $[\bar{\alpha}_{\text{min}}, \bar{\alpha}_{\text{max}}] \times [\zeta_{\text{min}}, \zeta_{\text{max}}]$. The values of the maximum point $(\hat{\bar{\alpha}}, \hat{\zeta})$ are estimates of the hyperparameters $\bar{\alpha}$ and ζ.

Here, ζ_{min} is determined by the equation

$$\zeta_{\text{min}} = \max_i \left\{ \frac{2\pi(x_i + y_i - 2\pi)}{x_i} \right\} \tag{8.18}$$

, which is derived on the assumption that all of the data $\{(x_i, y_i)\}$ is generated by the model in this part (Eqs. (8.5), (8.6), and (8.7)).

Chapter 9

Numerical experiment

9.1 Examples

Here, the method in this part is applied to the data $\{(x_i, y_i)\}$ generated with the noisy Morris-Lecar equations in appendix B. The numerical experiment in this part is the same condition as that in part II.

We show two examples of the estimates of the PRCs from the same datasets discussed in Sec. 7.1.1, where a sample size n is 100 and timings of the perturbations $\{t_i; i = 1, \dots, n\}$ are randomly chosen. The noise levels s, defined in appendix B, of the two examples are 0.3 (high) and 0.1 (low). The number of parameters that represent the transformed PRC $\bar{Z}(\bar{x})$ is $m = 99$ (see Appendix A).

Let us begin with the estimation of the hyperparameters $\bar{\alpha}$ and ζ. For the dataset with the high noise level $(s = 0.3)$, we set the range of the hyperparameters as $\bar{\alpha}_{\text{min}} = 1,\ \bar{\alpha}_{\text{max}} = 200,\ \zeta_{\text{min}} \approx -7.3\times10^{-3}$ and $\zeta_{\text{max}} = 0.2$. For the dataset with the low noise level $(s = 0.1)$, we set $\bar{\alpha}_{\text{min}} = 1,\ \bar{\alpha}_{\text{max}} = 200,\ \zeta_{\text{min}} \approx -1.4\times10^{-2}$ and $\zeta_{\text{max}} = 0.2$, where ζ_{min} is determined from the data $\{(x_i, y_i)\}$ using Eq.(8.18). The marginal likelihoods $\ln p_\zeta(\bar{\mathbf{y}}|\bar{\alpha}, \hat{\lambda})$ defined in Sec. 8.6 are numerically optimized on a 100×30 grid in the plane of the hyperparameters $(\bar{\alpha}, \zeta)$. As a result, pairs of the estimates of the hyperparameter $(\hat{\bar{\alpha}}, \hat{\zeta})$ for the datasets with the high noise level $(s = 0.3)$ and the low noise level $(s = 0.1)$ are about $(6.1 \times 10^1, -7.3 \times 10^{-3})$ and $(1.7 \times 10^1, 3.5 \times 10^{-2})$, respectively. The left and right panels of Fig. 9.1 show regions of level curves of $\ln p_\zeta(\bar{\mathbf{y}}|\bar{\alpha}, \hat{\lambda})$ over the hyperparameters for $s = 0.3$ and 0.1, respectively. The maximum points $(\hat{\bar{\alpha}}, \hat{\zeta})$ are shown as the points in Fig. 9.1.

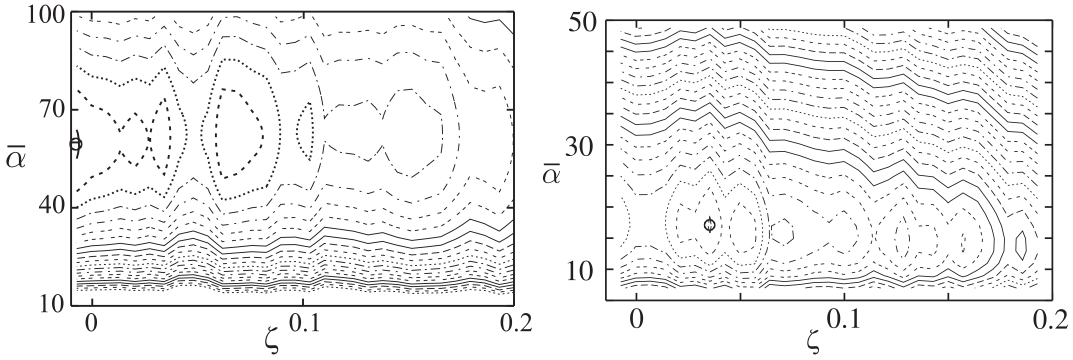

Figure 9.1: Level curves of $\ln p_\zeta(\bar{\mathbf{y}}|\bar{\alpha}, \hat{\lambda})$ over $[\bar{\alpha}_{\min}, \bar{\alpha}_{\max}] \times [\zeta_{\min}, \zeta_{\max}]$. The point on the region represents the maximum point $(\hat{\bar{\alpha}}, \hat{\zeta})$. The left and right panels correspond to the level curves with the high noise level $s = 0.3$ and the low noise level $s = 0.1$, respectively.

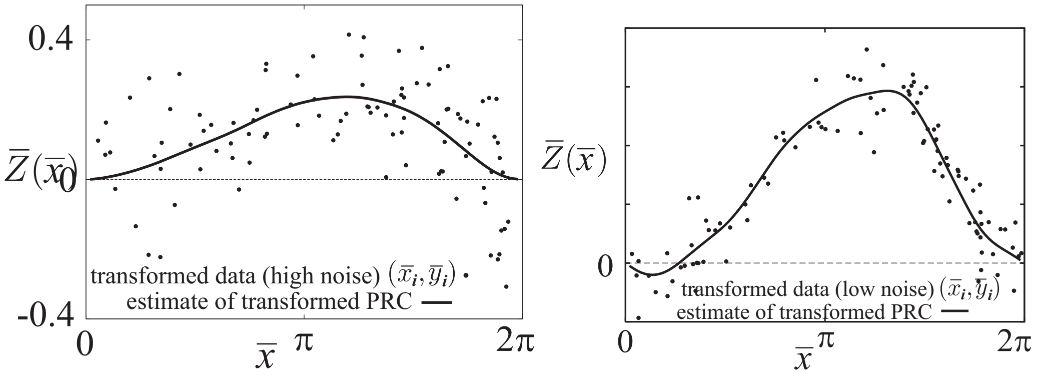

Figure 9.2: Transformed data and the estimate of the transformed PRC. The noise levels of the datasets in the left and right panels are high $(s = 0.3)$ and low $(s = 0.1)$, respectively.

The left and right panels of Fig 9.2 show the transformed data $\{(\bar{x}_i, \bar{y}_i)\}$ and the estimates of the transformed PRCs $\bar{Z}(\bar{x})$ on the hyperparameters $\hat{\bar{\alpha}}$ and $\hat{\zeta}$ for the high noise level $s = 0.3$ and the low noise level $s = 0.1$, respectively.

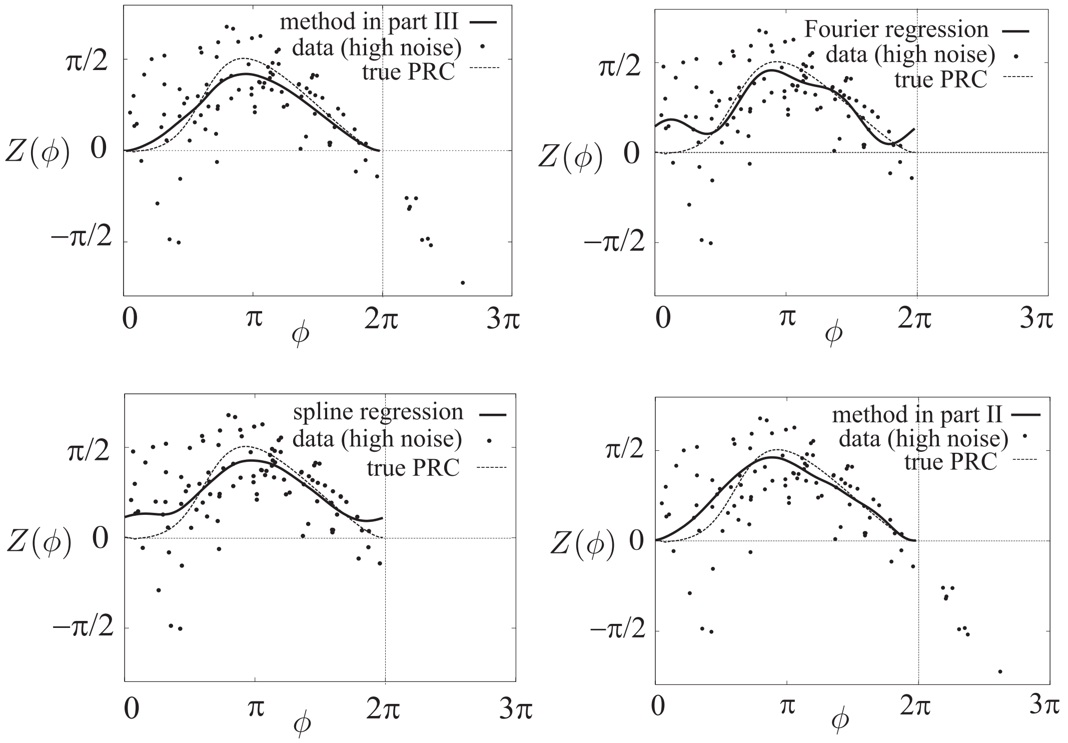

Figure 9.3: Comparison between the method in this part (upper–left panel), Fourier regression (upper–right panel), spline regression (lower–left panel) and the methods in part II (lower–right panel) using a set of data. The solid curve corresponds to the PRC estimated from the samples shown by the points, and the broken curve shows the true PRC estimated with noiseless simulation. These panels (except for the upper-left panel) are cited in our previous study.

Then, we show the estimate of the PRC $Z(\phi)$ through the method in this part. The estimates of the PRC $Z(\phi)$ for the datasets with $s = 0.3$ and $s = 0.1$ are shown as the solid curve in the upper left panel of Fig. 9.3 and Fig. 9.4, respectively. In the examples, both estimates of the PRC are not multi-valued functions, as discussed in Sec. 8.4. They are compared with the true PRC estimated in noiseless experiments. We discuss how to obtain the true PRC in appendix B. The true PRCs are shown as the broken curve in the upper left

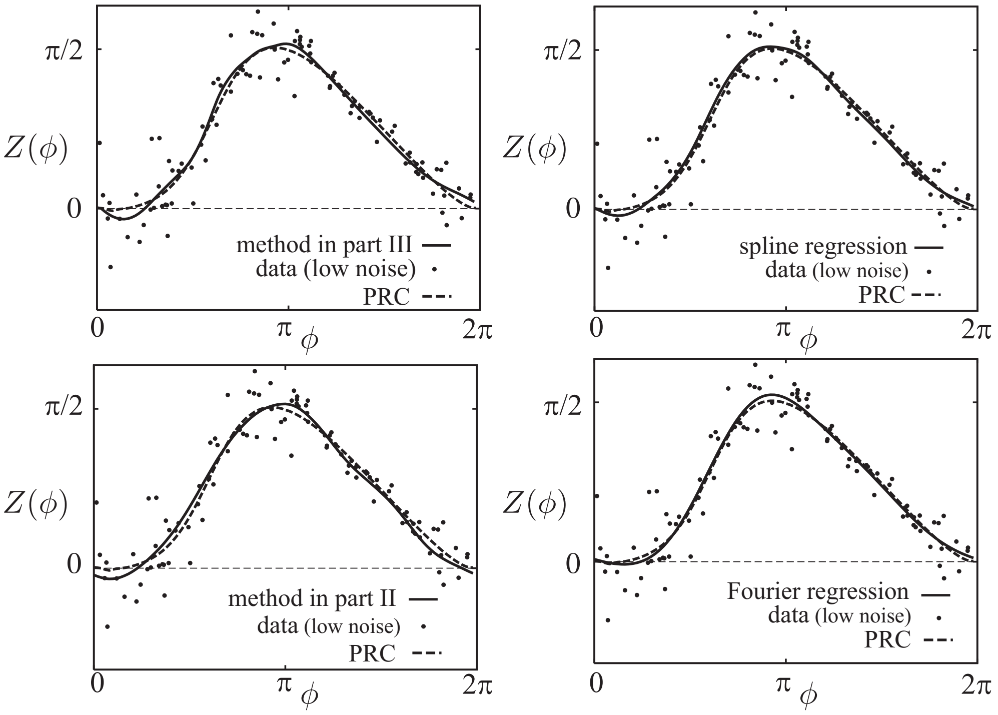

Figure 9.4: Comparison between the method in this part and conventional methods using artificial data. The solid curve corresponds to the PRC estimated from samples shown by black dots, and the broken curve shows the true PRC estimated with noiseless simulation. The upper left and upper right panels correspond to the method in this part and the spline regression, respectively; the result with the Fourier regression is also shown in the lower panel. Differences in the samples shown in the upper left and upper right (or lower) panels are explained in the text.

panel of Fig. 9.3 and Fig. 9.4. Note that the true PRC satisfies the condition in Eq. (8.12).

Finally, we compared the estimate of the PRC through the method in this part with three estimates through the Fourier regression and the spline regression and the method in part II. The results are shown as the solid curve in the other three panels of Fig. 9.3 and Fig. 9.4. The true PRC is also shown as the broken curve. In Fig. 9.4 (high noise level), the solid curves by the method in this part and part II are closer to the true PRC than the ones generated by Fourier regression and spline regression. In Fig. 9.4 (low noise level), on the other hand, all solid curves estimated by these methods are close to the true PRC.

9.2 Statistical comparison using average L^2 error

Here, we consider sets of data and compare the accuracy of the estimates. We use the measure of the accuracy as the average L^2 error

$$\frac{1}{N_D}\sum_{w=1}^{N_D}\left(\int (Z(\phi)-\hat{Z}^{[w]}(\phi))^2 d\phi\right)^{1/2}, \tag{9.1}$$

where the number of datasets is expressed as N_D and the estimate from the w th dataset is defined by $\hat{Z}^{[w]}(\phi)$. We consider seven datasets, which are different levels of the external noise: $s = 0.1, 0.15, 0.2, 0.25, 0.3, 0.35$ and 0.4. For each value of s, we consider $N_D = 500$ data sets in the cases of Fourier regression, spline regression and the method in this part, and $N_D = 100$ data sets in the case of the method in part II.

The result of the comparison is shown in Fig. 9.5. The horizontal axis represents the noise level s and the vertical axis represents the average L^2 error defined by Eq. (9.1). Fourier regression (red), spline regression (blue), the method in part II (green) and the method in this part (black) are represented by the lines and the 95% confidence intervals in Fig. 9.5. The result shows that the estimator of the method in this part is more accurate than that of Fourier regression and spline regression for all s. Fig. 9.5 also shows that the accuracy of the estimate of the method in this part is the same as that of the method in part II when s is small.

Note that the estimates of the PRC for all of the datasets are one-valued function, as discussed in Sec. 8.4.

9.3 Detail analysis with L^2 errors

9.3.1 Comparison to conventional regressions

Scatter plots

In this section, we present a detailed comparison of the L^2 errors between the method in part III and the conventional regressions. To see raw data of the L^2 errors, we show scatter plots of the L^2 errors in Fig. 9.6 and Fig 9.7. The horizontal axes in the panels correspond to the

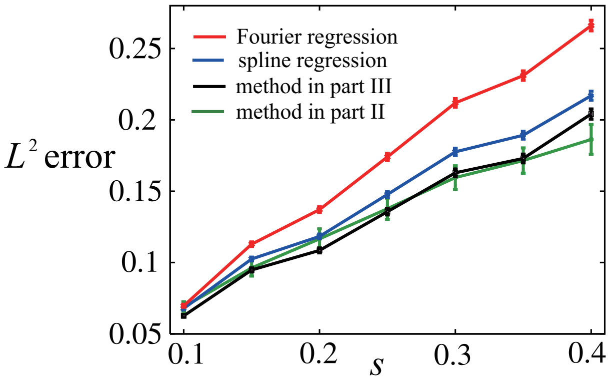

Figure 9.5: Comparison of the average L^2 errors with respect to the noise level s.

L^2 errors by the method in part III; the vertical axes in the panels of Fig. 9.6 and Fig. 9.7 correspond to the L^2 errors by the spline regression and Fourier regression, respectively. The panels in these figures are different with the noise levels $s = 0.1, 0.15, 0.2, 0.25, 0.3, 0.35$ and 0.4. The point in the panels represents a set of artificial data; we plot $N_D = 500$ points obtained by the datasets of a noise level in each panel.

Win rates

To compare the differences of the L^2 accuracy, we estimate win rates of the method in part III to conventional regressions using the datasets. Here, we define $\{Y_w\}_{w=1}^{N_D}$ as

$$Y_w = \begin{cases} 1 & \text{the method in part III outperforms another method for } w\text{-th dataset,} \\ 0 & \text{otherwise,} \end{cases} \tag{9.2}$$

and assume that Y_w follows an i.i.d. binomial distribution. The win rate corresponds to the population rate p of the binomial distribution where the estimate $\hat{p}$ is $\sum_{w=1} Y_w/N_D$. Using the normal approximation, we calculate the 95 % confidence interval of $\hat{p}$ as $[\hat{p} - 1.96\sqrt{\hat{p}(1-\hat{p})/N_D}, \hat{p} + 1.96\sqrt{\hat{p}(1-\hat{p})/N_D}]$. Note that the approximation is valid when p is near 0.5 and N_D is sufficently large.

In Fig. 9.8, we present the estimates of the win rates and the confidence intervals with respect to the noise level s. The left and right panel represents the win rates of the method in part III to the spline and Fourier regressions, respectively. The left and right panels show

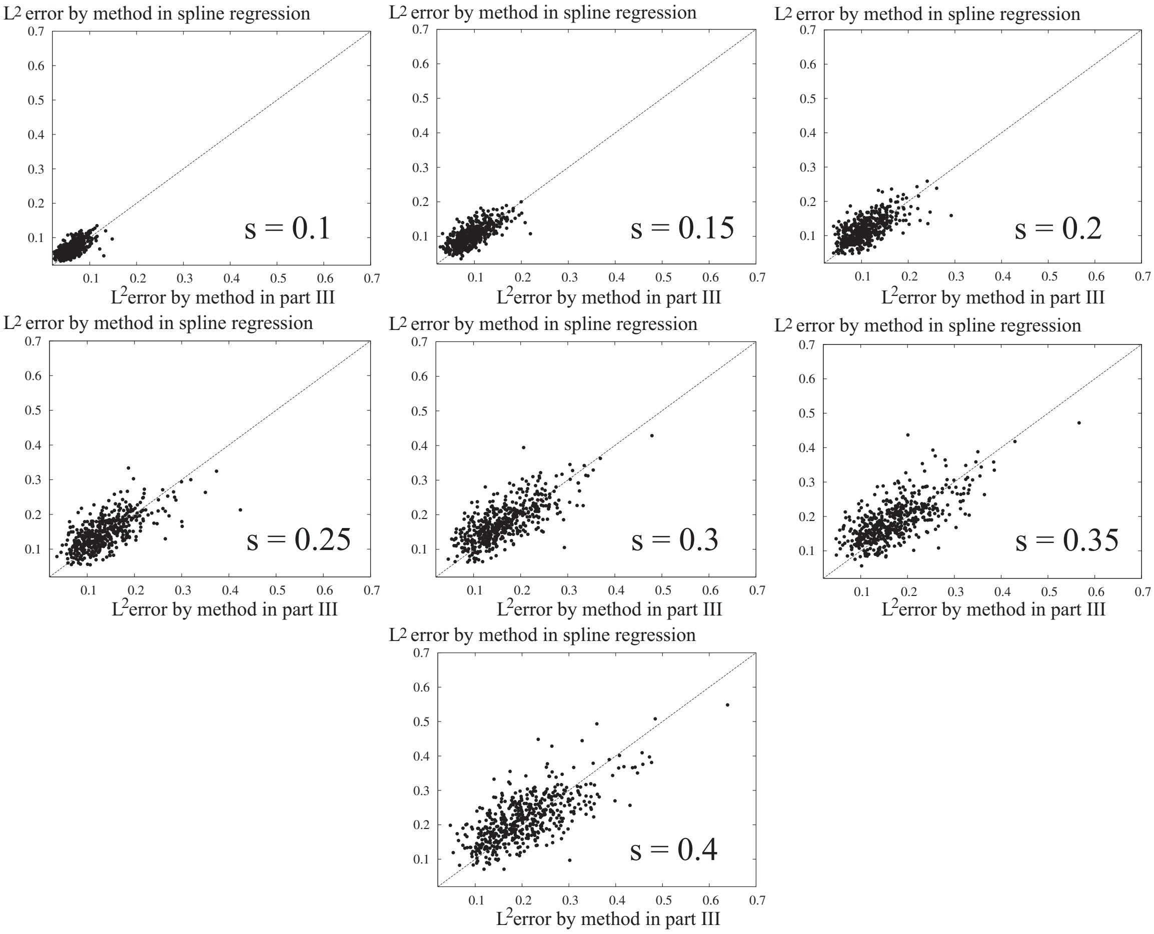

Figure 9.6: Scatter plots of L^2 errors by the method in part III (horizontal axis) and the spline regression (vertical axis).

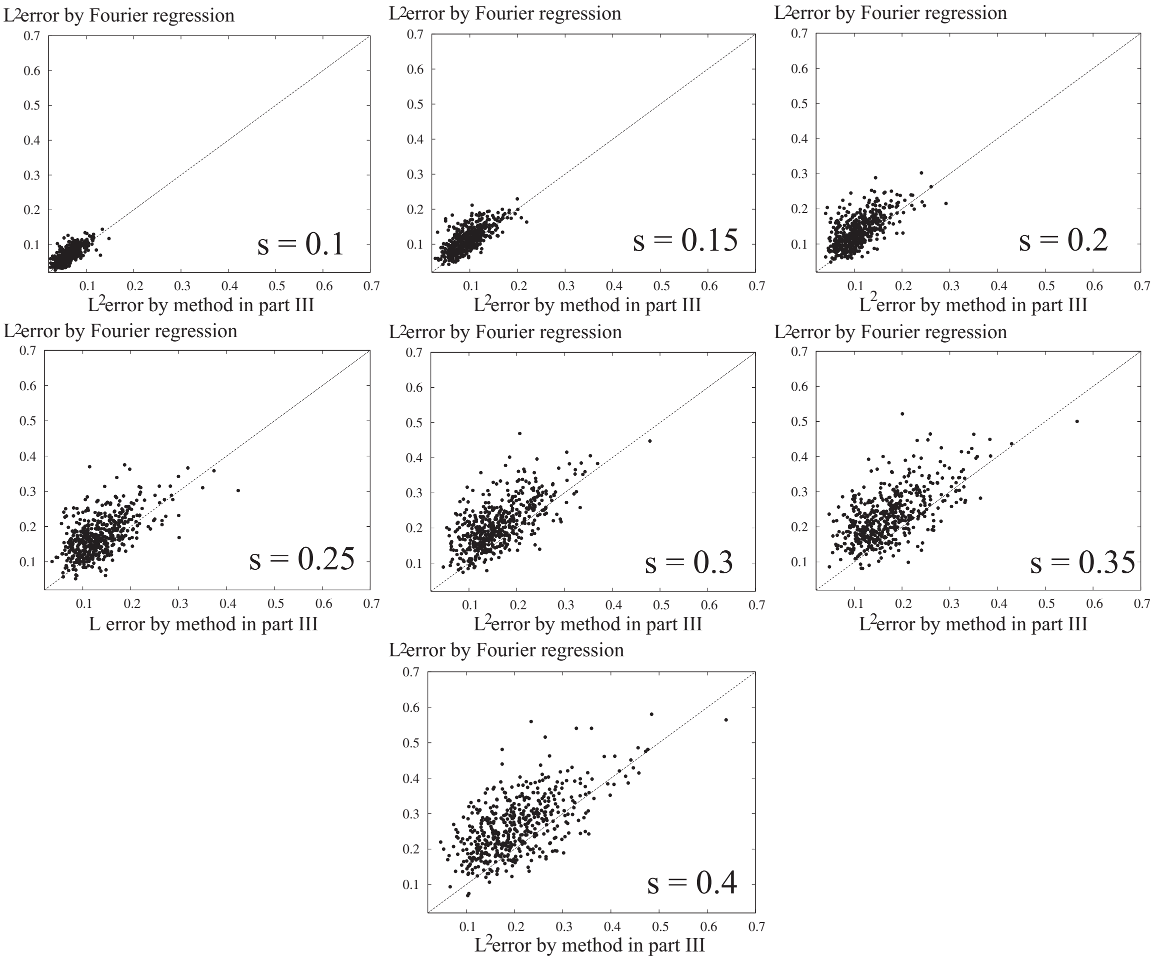

Figure 9.7: Scatter plots of L^2 errors by the method in part III (horizontal axis) and the Fourier regression (vertical axis).

that the method in part III outperforms the spline and Fourier regressions significantly above chance for all noise levels s, respectively.

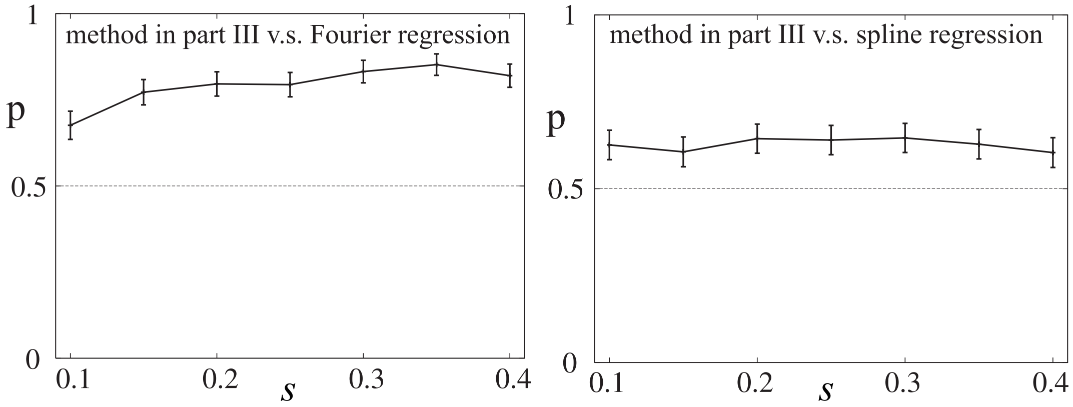

Figure 9.8: Estimates of the win rates of the method in part III to the spline (left panel) and Fourier (right panel) regressions with respect to s. The error bars represent the 95 % confidence intervals by normal approximation.

Box and whisker plots

Here, we show the difference between the method in part III and the conventional methods in more detail. We show box and whisker plots [Tukey, 1977] of differences from the L^2 errors by the spline regression to those by the method in part III in the left panel of Fig. 9.9. The vertical and horizontal axes correspond to the difference and the noise level s, respectively. Each box and whisker plot represents five-number summaries of the differences: sample minimum, lower quantile, median, upper quantile, and sample maximum. Note that lower and upper edges of the box do not represent confidence interval of the median but lower and upper quantiles, respectively.

When the median of the differences is above zero, the method in part III outperforms the spline regression for over half of the datasets. The box and whisker plots in the left panel of Fig. 9.9 suggest the outperformance for all noise levels s.

The right panel of Fig. 7.9 represents box and whisker plots of differences from the L^2 errors by Fourier regression to those by the method in part III. This panel also indicates that the method in part III outperforms Fourier regression for over half of the datasets for all noise levels s. Furthermore, the quantiles of the box and whisker plots in the right panel suggest that the method in part III outperforms Fourier regression for about 75 % of the datasets when $s \geq 0.15$.

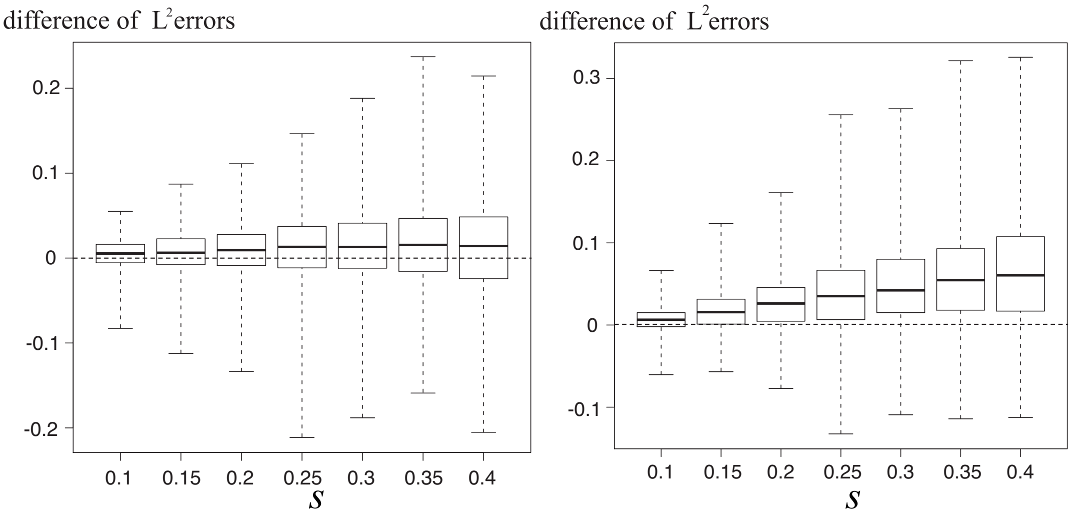

Figure 9.9: Box and whisker plots of the differences of L^2 errors with respect to s. The differences from the spline and Fourier regressions to the method in part III are presented in the left and right panels, respectively. The line, upper edge and lower edge in each box represent the median, upper quantile and lower quantile, respectively. The upper and lower edges of each whisker represent the sample minimum and maximum, respectively.

9.3.2 Comparison to method in part II

Scatter plots

In this section, we present a detailed comparison of the L^2 errors between the methods in part III and part II. In Fig. 9.10, we show scatter plots of the L^2 errors obtained by the method in part III (horizontal axis) and part II (vertical axis). The panels correspond to the noise levels $s = 0.1, 0.15, 0.2, 0.25, 0.3, 0.35$ and 0.4, respectively. The point in the panels represents a set of artificial data; we plot $N_D = 100$ points obtained by the datasets of a noise level in each panel.

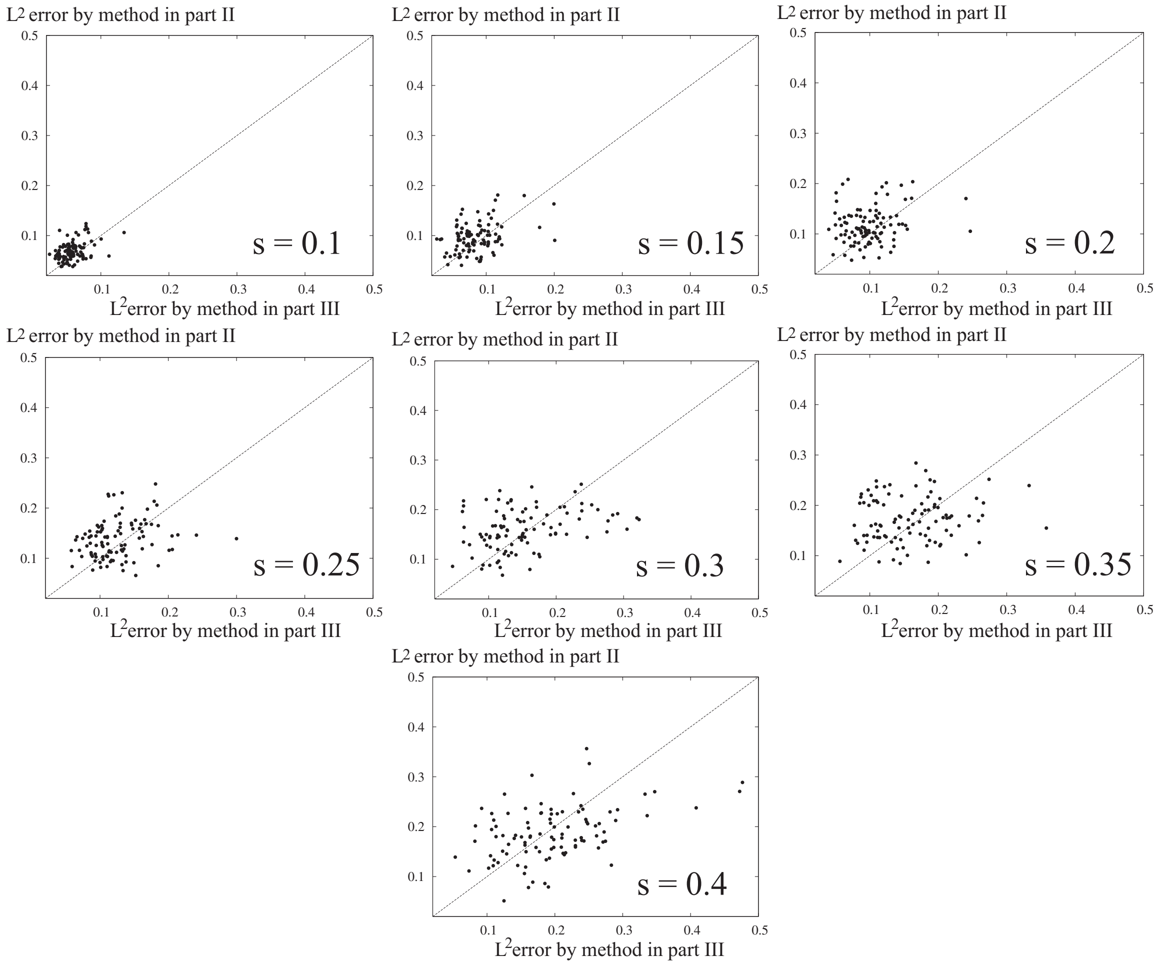

Figure 9.10: Scatter plots of L^2 errors by the method in part III (horizontal axis) and in part II (vertical axis) with respect to the noise levels s.

Win rates

To compare the differences of the L^2 accuracy, we estimate win rates of the method in part III to the method in part II. As explained in the previous section, we estimate the win rate p and the 95% confidence interval using a binomial distribution. The estimates of them with respect to the noise level s are shown in Fig. 9.11; the vertical axis corresponds to the win rate. The method in part III outperforms the method in part II significantly above chance when $s \leq 0.25$.

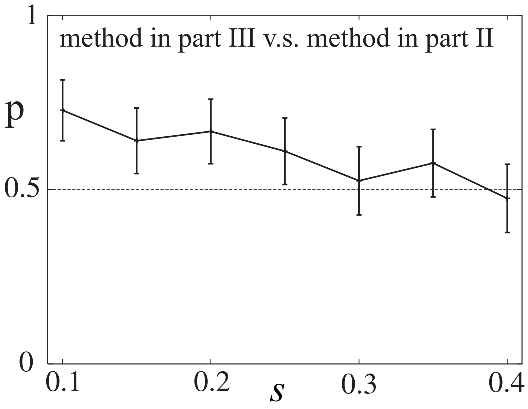

Figure 9.11: Estimates of the win rates of the method in part III to the method in part II with respect to s. The error bars represent the 95 % confidence intervals by normal approximation.

Box and whisker plots

Here, we show the difference between the method in part II and the conventional methods in more detail. We show box and whisker plots of differences from the L^2 errors by the method in part II to those by the method in part III in Fig. 9.12. The vertical and horizontal axes correspond to the difference and the noise level s, respectively.

When the median of the differences is above zero, the method in part III outperforms the method in part II for over half of the datasets. The box and whisker plots suggest the outperformance except for the noise level $s = 0.4$. By the quantiles of the box and whisker plots, the method in part III outperforms the method in part II for about 75 % of the datasets when $s = 0.1$.

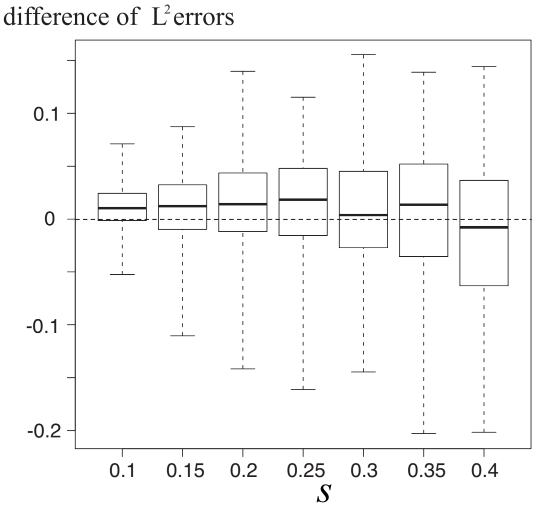

Figure 9.12: Box and whisker plots of the differences of L^2 errors with respect to s. The differences from the method in part II to the method in part III are presented.

9.4 Computation time

The Computation times of Fourier regression, spline regression, the methods in this part and part II for the datasets are compared. The computation times are obtained on a Fujitsu PRIMERGY RX200 S5, whose CPU is Intel Xeon X5570 (2.93GHz, 8 core). The methods are implemented using C++ code with LAPACK. The estimate of the method in part II is calculated with parallel computing, where we use 4 CPUs (32 core) and implement the method in part II using MPI.

We show the averages of the computation times over the datasets in Table. 9.1. This suggests that the computation time of the method in part II ($\approx$ 3 h) is considerably longer than that of other methods (1 min or less).

The computation times without the method in part II are mostly determined by the number of iterations N_L of a linear computation, such as Eqs. (A.7) and (A.10) in appendix A, and the number of parameters M of the linear computation. The time complexities of the methods without the method in part II are $O(M^3 N_L)$, because all linear computations in this thesis are implemented using direct methods [Press et al., 2007], which do not consider sparsity of matrices.

method	computation time (sec)	M	N_L
Fourier regression	2.4×10^{-5}	7	1
spline regression	1.5×10^{0}	100	2×10^{2}
method in part III	4.5×10^{1}	99	6×10^{3}
method in part II	8.8×10^{3}	*	*

Table 9.1: Averages of computation times, the number of parameters M and the number of iterations N_L

We also list the number of parameters M and the number of iterations N_L of a linear computation performed using all methods mentioned above except the method in part II in Table. 9.1. This suggests that the computation times of these methods are roughly consistent with their time complexities. The consistency explains the difference in the computation times between Fourier regression, spline regression and the method in this part. The large difference in the computation times between Fourier regression and spline regression mainly arises from the difference in the number of parameters M. The difference in the computation times between spline regression and the method in this part arises from difference in the number of hyperparameters. The spline regression has one hyperparameter. On the other hand, the method in this part has two hyperparameters: $\bar{\alpha}$ and ζ.

9.5 On the choice of hyperparameters

Unbiasedness of the estimate $\hat{\zeta}$

Here, we compute averages and confidence intervals of the estimate $\hat{\zeta}$ to validate the use of $\ln p_\zeta(\bar{\mathbf{y}}|\bar{\alpha}, \hat{\lambda})$ in Sec. 8.6. The result is plotted in Fig. 9.13, where the horizontal axis represents the value of s, and the vertical axis represents the average of the estimate of $\zeta = Z(0)$. The solid line in Fig. 9.13 represents the method in this part, the broken line represents spline regression, and the dotted line represents Fourier regression. We ignore the results of the method in part II, because the confidence interval is too large for a small size of datasets. The true ζ is zero in the case of the Morris-Lecar equations. The results show that the estimator $\hat{\zeta}$ defined in Sec. 8.6 seem to be unbiased for the dataset when $s \leq 0.3$.

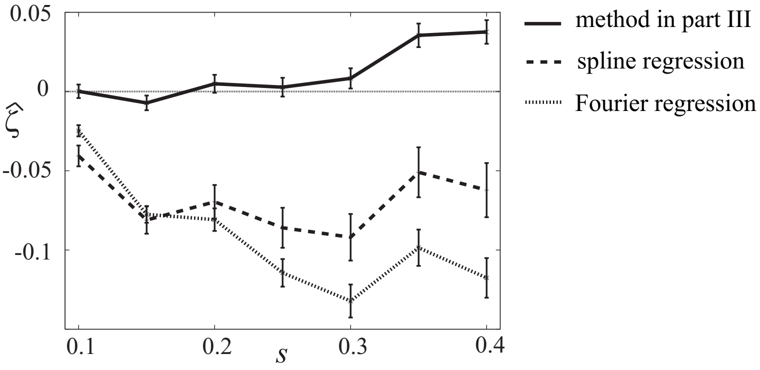

Figure 9.13: Comparison of the averages of the estimates $\hat{\zeta}$

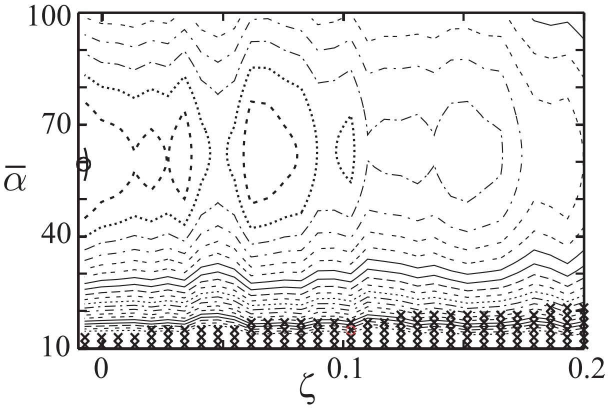

Figure 9.14: Level curves of $\ln p_\zeta(\bar{\mathbf{y}}|\bar{\alpha}, \hat{\lambda})$. The details are presented in the text.

Multi-valued functions induced by missing choice of hyperparameters

As discussed in Sec. 8.4, the estimate of PRC through the method in part III may be a multi-valued function; for all datasets used in this thesis, the estimates are not multi-valued functions. In this section, we show a example that the estimate is a multi-valued function because of missing the choice of the hyperparameters $(\bar{\alpha}, \zeta)$. For the dataset presented in Fig. 9.3, we again plot the level curves of $\ln p_\zeta(\bar{\mathbf{y}}|\bar{\alpha}, \hat{\lambda})$ in Fig. 9.14. The point is a maximum point of $\ln p_\zeta(\bar{\mathbf{y}}|\bar{\alpha}, \hat{\lambda})$. The cross means that the estimate of PRC is a multi-valued function on the corresponding values of hyperparameters.

To confirm this, we show the estimate on the values of hyperparameters $(\bar{\alpha}, \zeta) \approx$

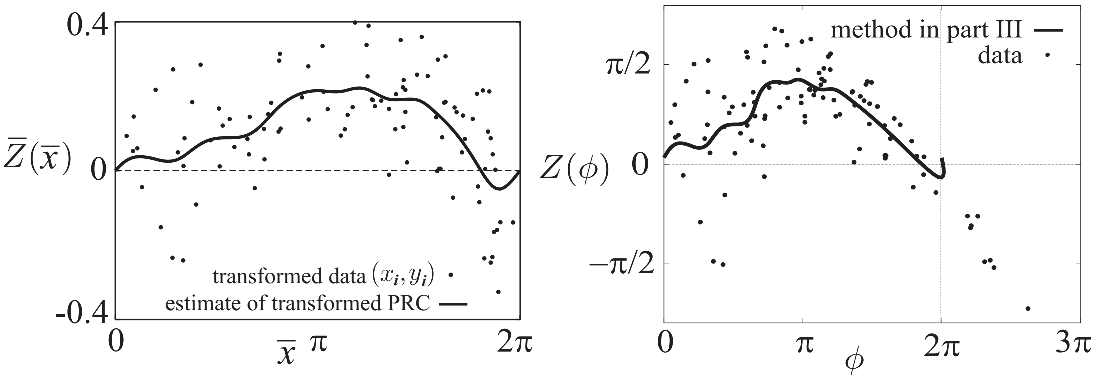

Figure 9.15: Estimate of transformed PRC (left panel) and estimate of PRC (right panel) on wrong values of hyperparameters.

$(15, 0.1)$ corresponding to the red point of the Fig. 9.14. The transformed data and the estimate of transformed PRC are represented by the points and curve in the left panel of Fig. 9.15, respectively. The estimate of PRC is obtained through the inverse transformation ψ_ζ as shown in the right panel of Fig. 9.15. The estimate of PRC near $\phi \approx 2\pi$ has multi values.

Chapter 10

Summary and future problems

10.1 Summary

Two statistical methods are proposed for estimating the phase response curve (PRC). The novelty of these methods is that they take into account the correlation between errors in the explanatory and response variables of PRC.

In part II, we formulated the method in a Bayesian framework with a smoothness prior, and implemented using the replica exchange Monte Carlo (REM) method, which enables efficient sampling from multimodal posterior distributions. We tested the method in part II both with artificial data generated by the noisy Morris-Lecar equations and real experimental data recorded from the pyramidal cells of in rat motor cortex. The test with artificial data shows that the the method in part II is advantageous over conventional regression [Galán et al., 2005, Ota et al., 2009b] when the level of noise is high. In the analysis of the real experimental data with large fluctuation of spike intervals, there is considerable difference compared to the conventional regression, which only allow for the errors in the response variable.

In part III, we propose more computationally efficient method, which also take into account the correlation. We slightly modify the model in part II, and show that the modified model is reduced to a normal regression model by using a transformation that removes the correlation. Thus, PRC is estimated through the normal regression. The method in part III is tested using data generated with the noisy Morris-Lecar equations in part II. We compare the method in part III with the method in part II and conventional regression. This comparison shows that the method in part III is advantageous to the conventional regression in terms of accuracy, while it is better than the method in part II in terms of computation times.

10.2 Future problems

PRCs estimated from experimental data are useful for simulating large-scale neural networks such as the blue brain project [Markram, 2006]. PRCs are concise representation of the dynamical systems of neurons; mathematical neuron models in the neural networks such as the Hodgkin-Huxley equations [Hodgkin and Huxley, 1952] and Morris-Lecar equations [Morris and Lecar, 1981] can be replaced to PRCs.

In the methods in part II and part III, we assume that the period follows a truncated normal and a log normal distributions, respectively. In neuroscience, various distributions of periods are considered: for example, a exponential distribution [Dayan and Abbott, 2001, Rieke and Warland, 1999], a gamma distribution [Kuffler et al., 1957, Shimokawa and Shinomoto, 2009], an inverse Gaussian distribution [Tuckwell, 1988, Chhikara and Folks, 1989]. Our method can be easily extended to deal with these distributions and a nonparametric distribution estimated from periods in experiments. For example, we can use kernel density estimation [Parzen, 1962, Silverman, 1998] as the nonparametric method.

In part II, we introduce a "phenomenological" hypothesis that noises in the data essentially correspond to fluctuation of periods, which lead to a correlation between errors in explanatory and response variables. In future, the correlation will be studied from "theoretical" viewpoint ; such a study will elucidate the origin of the fluctuation of period and replace it with a different mechanism that effectively generates a similar correlation. Such considerations may lead to a more realistic model of errors and better algorithms based on the model.

In part III, we assume that the error ν_i follows the log normal distribution represented by

$$\ln \nu_i \sim \mathcal{N}(0, \lambda^2).$$

The mean of $\ln \nu_i$ is zero; this indicates that the median of y_i is $Z(\phi_i)$ in Eq.(8.6). Therefore, the method in part III are considered as a version of quantile (median) regression [Koenker, 2005] under a log normal distribution. To change the mean of $\ln \nu_i$, we can estimate the

PRCs from the data whose expectation or mode is assumed to be $Z(\phi_i)$. We will investigate which the best estimator is.

As mentioned in Sec. 3.2, methods using different types of experiments are proposed, where white noise [Ermentrout et al., 2007], correlated noise [Ota et al., 2009a], or arbitrary input [Aonishi and Ota, 2006, Ota et al., 2009b] is injected to a neuron. Our approach in part II will be extended to deal with data generated with the experiments.

Appendix A

Bayesian regression with a boundary condition

In Sec. 8.5, we briefly introduce a Bayesian framework to estimate the transformed PRC $\bar{Z}(\bar{x})$ based on the normal regression model (8.13) under the conditions: the transformed PRC $\bar{Z}(\bar{x})$ has the fixed boundary point $\bar{Z}(0) = 0$, $\bar{Z}(\bar{x})$ is periodic in the domain $[0, 2\pi)$, and $\bar{Z}(\bar{x})$ is smooth. A detail of the estimation is explained in this appendix. We also explain how to estimate the hyperparameter $\bar{\alpha}$ and ζ using the log marginal likelihood represented by Eq.(8.17). The framework discussed in this appendix is based on a framework proposed by Tanabe and Tanaka [1983].

Here, we explain a discrete representation of the transformed PRC $\bar{Z}(\bar{x})$, whose domain is from 0 to 2π. The region $[0, 2\pi)$ along $\bar{x}$-axis is divided into $m+1$ successive intervals $\{[\bar{x}_j^*, \bar{x}_{j+1}^*); j = 0, \ldots, m\}$, where $\bar{x}_0^* = 0$ and $\bar{x}_{m+1}^* = 2\pi$. The transformed PRC is represented by a piecewise constant function $\bar{Z}(\bar{x})$ indexed with $\bar{\mathbf{z}} = (\bar{z}_1, \ldots, \bar{z}_m)^T$, where $\bar{z}_i = \bar{Z}(\bar{x})$ for $\bar{x} \in [\bar{x}_i^*, \bar{x}_{i+1}^*)$. These definitions are illustrated in Fig. A.1. Note that we do not consider $(\bar{z}_0 = \bar{Z}(0), \bar{z}_1, \ldots, \bar{z}_m)^T$ but consider $\bar{\mathbf{z}}$ for the fixed boundary condition $\bar{Z}(0) = 0$.

To calculate the posterior about $\bar{\mathbf{z}}$ based on the Bayes' theorem, a likelihood and a prior about $\bar{\mathbf{z}}$ is necessary. The likelihood is derived by Eq. (8.13) and the discrete representation of the transformed PRC $\bar{Z}(\bar{x})$, and defined below

$$p(\bar{\mathbf{y}}|\bar{\mathbf{z}}, \lambda) = \frac{1}{(2\pi\lambda^2)^{n/2}} \exp\left\{ -\frac{1}{2\lambda^2} ||\bar{\mathbf{y}} - E\bar{\mathbf{z}}||^2 \right\}, \tag{A.1}$$

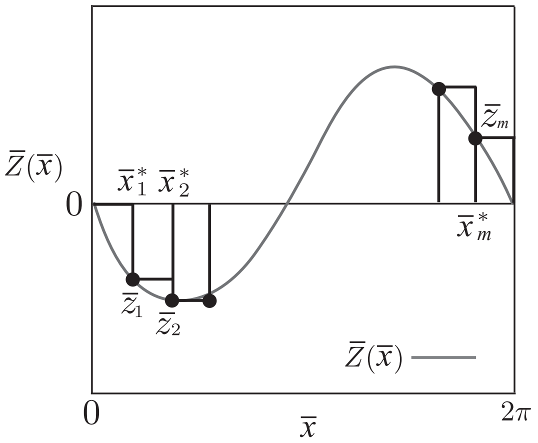

Figure A.1: Representation of the transformed PRC $\bar{Z}(\bar{x})$

where E is the $n \times m$ matrix, whose (i, j) component is given by

$$E_{ij} = \begin{cases} 1 & \bar{x}_i \in [\bar{x}_j^*, \bar{x}_{j+1}^*) \\ 0 & \text{otherwise} \end{cases} . \tag{A.2}$$

A density function of the prior of $\bar{\mathbf{z}}$, which describe the periodicity and the smoothness of $\bar{Z}(\bar{x})$ is expressed as

$$p(\bar{\mathbf{z}}|\bar{\tau}) \propto \exp\left\{-\frac{\bar{\tau}^2}{2}\sum_{j=0}^{m}(\bar{z}_{j-1} - 2\bar{z}_j + \bar{z}_{j+1})^2\right\} \tag{A.3}$$

where we assume the periodic and fixed boundary condition $\bar{z}_{-1} = \bar{z}_m$ and $\bar{z}_0 = \bar{z}_{m+1} = 0$. Then, a matrix form of the density function is expressed as

$$p(\bar{\mathbf{z}}|\bar{\tau}) = \frac{\bar{\tau}^m}{(2\pi)^{m/2}\sqrt{|\det(D^T D)|}} \exp\left\{-\frac{\bar{\tau}^2}{2}||D\bar{\mathbf{z}}||^2\right\}, \tag{A.4}$$

where D is the $(m+1)\times m$ matrix, whose (i,j) component is given by

$$D_{ij} = \begin{cases} -2 & i=j \\ 1 & |i-j|=1 \text{ or } (i,j)=(m+1,1) \\ 0 & \text{otherwise} \end{cases} . \tag{A.5}$$

The factor $\bar{\tau}$ controls a degree of a smoothness of the transformed PRC $\bar{Z}(\bar{x})$. When $\bar{\tau}$ is larger, the estimated curve becomes smoother.

Using the Bayes' theorem, the posterior distribution of $\bar{\mathbf{z}}$ can be analytically derived as

$$\bar{\mathbf{z}}|\bar{\mathbf{y}}, \lambda, \bar{\tau} \sim \mathcal{N}(\boldsymbol{\mu}_{\bar{\mathbf{z}}}, \lambda_{\bar{\mathbf{z}}}), \tag{A.6}$$

where

$$\boldsymbol{\mu}_{\bar{\mathbf{z}}} = \lambda_{\bar{\mathbf{z}}} E^T \bar{\mathbf{y}}, \tag{A.7}$$

$$\lambda_{\bar{\mathbf{z}}} = (E^T E + \lambda^2 \bar{\tau}^2 D^T D)^{-1}. \tag{A.8}$$

As a result, the estimate of the transformed PRC $\bar{Z}(\bar{x})$ from the transformed data is gotten by the calculation of Eq. (A.7).

In the above discussion, the tuning parameters λ and $\bar{\tau}$, which is called "hyperparameters", are fixed. We estimate the hyperparameters to maximize the log marginal likelihood defined by Eq. (8.17).

When the hyperparameters λ and $\bar{\tau}$ are changed to new hyperparameters λ and $\bar{\alpha}$, where $\bar{\alpha} = \lambda\bar{\tau}$, a zero point of a derivative of the log marginal likelihood with respect to λ can be derived analytically. As a result, the estimate of λ is expressed as

$$\hat{\lambda} = \sqrt{\frac{1}{n}(||\bar{\mathbf{y}} - E\boldsymbol{\mu}_{\bar{\mathbf{z}}}||^2 + \bar{\alpha}^2||D\boldsymbol{\mu}_{\bar{\mathbf{z}}}||^2)}. \tag{A.9}$$

Substituting $\hat{\lambda}$ to the log marginal likelihood, we only consider a maximization of a log marginal likelihood defined below

$$\ln p(\bar{\mathbf{y}}|\bar{\alpha}, \hat{\lambda}) = \ln|\det \lambda_{\bar{\mathbf{z}}}| - 2m \ln \bar{\alpha} + 2n \ln \hat{\lambda} + \text{const}, \tag{A.10}$$

over the hyperparameters $\bar{\alpha}$.

In Sec. 8.6, the additional hyperparameter ζ is contained in the log marginal likelihood. However, the above derivation is valid, and we can use Eqs.(A.9) and (A.10) without modification.

Appendix B

Conductance based neuron models

B.1 Morris-Lecar equations

In this section, we explain how to generate artificial data used in part II and III. Here we employ the noisy Morris-Lecar equations [Morris and Lecar, 1981] as a source of artificial data; this is a bivariate stochastic differential equation widely used in neural science. This neuron model is defined by a set of equations

$$\begin{aligned} \frac{dv}{dt} =& - g_{\mathrm{Ca}^{2+}} m_{\infty}(v)(v - v_{\mathrm{Ca}^{2+}}) - g_{\mathrm{K}^{+}} n(v - v_{\mathrm{K}^{+}}) - g_{\mathrm{leak}}(v - v_{\mathrm{leak}}) + \xi(t) + i(t), \\ \frac{dn}{dt} =& \frac{n_{\infty}(v) - n}{\bar{\tau}_n(v)}, \end{aligned} \tag{B.1}$$

where the variables v and n represent the voltage of the neuron and the ratio of open K^{+} channels, respectively. The functions $m_{\infty}(v), n_{\infty}(v)$ and $\bar{\tau}_n(v)$ are defined by

$$\begin{aligned} m_{\infty}(v) = \frac{1 + \tanh\{(v - v_1)/v_2\}}{2},\ n_{\infty}(v) = \frac{1 + \tanh\{(v - v_3)/v_4\}}{2}, \\ \bar{\tau}_n(v) = \frac{1}{\cosh\{(v - v_3)/(2v_4)\}}. \end{aligned} \tag{B.2}$$

The values of parameters used in this study are as follows: $g_{\mathrm{Ca}^{2+}} = 1.1$, $g_{\mathrm{K}^{+}} = 2.0$, $g_{\mathrm{leak}} = 0.5$, $v_{\mathrm{Ca}^{2+}} = 100$, $v_{\mathrm{K}^{+}} = -70$, $v_{\mathrm{leak}} = -50$, $v_1 = -1.0$, $v_2 = 15.0$, $v_3 = 10.0$, and $v_4 = 14.5$.

The term $\xi(t)$ represents white noise added to the voltage component, which satisfies the relations

$$\mathbb{E}[\xi(t)] = 0, \qquad \mathbb{E}[\xi(t)\xi(t')] = s^2\delta(t-t'), \tag{B.3}$$

where δ denotes the Dirac's δ-function. The current $i(t)$, which comes from the outside of a neuron, is assumed to be given by

$$i(t) = i_c + i_p\delta(t-t_i), \tag{B.4}$$

where the values of i_c and i_p are 8 and 2 respectively.

To solve the stochastic differential equation and generate artificial data, we use the Euler-Maruyama method [Kloeden and Platen, 2000]. The "true" PRCs shown in the following section are calculated by linear interpolation of points given by simulations of the noiseless Morris-Lecar equations $(s = 0)$.

B.2 Hodgkin-Huxley equations

In this section, we explain the details of Hodgkin-Huxley equations, which are used for showing the example of the PRC $\mathbf{Z}(\phi)$ in Chap. 1. The Hodgkin-Huxley equations is described as

$$\begin{aligned}
\frac{dv}{dt} =& -g_{\mathrm{Na}^+}m^3h(v-v_{\mathrm{Na}^+}) - g_{\mathrm{K}^+}n^4(v-v_{\mathrm{K}^+}) - g_{\mathrm{leak}}(v-v_{\mathrm{leak}}) + i(t),\\
\frac{dm}{dt} =& \alpha_m(v)(1-m) - \beta_m(v)m,\\
\frac{dh}{dt} =& \alpha_h(v)(1-h) - \beta_h(v)h,\\
\frac{dn}{dt} =& \alpha_n(v)(1-n) - \beta_n(v)n,
\end{aligned} \tag{B.5}$$

where the variables v, m^3h and n represent the voltage of the neuron, the open probability of the Na^+ channel, and the open probability of the K^+ channels, respectively. The functions in Eqs. (B.5) are defined by

$$
\begin{aligned}
\alpha_m(v) &= \frac{0.1(25-v)}{\exp\{(25-v)/10\}-1}, & \beta_m(v) &= 4\exp\left\{-\frac{v}{18}\right\}, \\
\alpha_h(v) &= 0.07\exp\left\{\frac{-v}{20}\right\}, & \beta_h(v) &= \frac{1}{\exp\{(30-v)/10\}+1}, \\
\alpha_n(v) &= \frac{0.01(10-v)}{\exp\{(10-v)/10\}-1}, & \beta_n(v) &= 0.125\exp\left\{-\frac{v}{80}\right\}.
\end{aligned}
$$

The values of parameters used in this study are as follows: $g_{\mathrm{Na}^+} = 120$, $g_{\mathrm{K}^+} = 36$, $g_{\mathrm{leak}} = 0.3$, $v_{\mathrm{Na}^+} = 55$, $v_{\mathrm{K}^+} = -72$, and $v_{\mathrm{leak}} = -49.387$. The term $i(t) = 8$ is a constant for the periodic activity of the neuron.

Bibliography

A. Abouzeid and B. Ermentrout. Type-II phase resetting curve is optimal for stochastic synchrony. *Physical Review E*, 80(1):11911, 2009.

J.A. Acebron, L.L. Bonilla, C.J.P. Vicente, F. Ritort, and R. Spigler. The Kuramoto model: A simple paradigm for synchronization phenomena. *Reviews of modern physics*, 77(1): 137–185, 2005.

E. D. Adrian. The electrical activity of the mammalian olfactory bulb. *Electroencephalography and clinical Neurophysiology*, 2(1-4):377–388, 1950.

I. Aihara. Modeling synchronized calling behavior of Japanese tree frogs. *Physical Review E*, 80(1):11918, 2009.

I. Aihara, S. Horai, H. Kitahata, K. Aihara, and K. Yoshikawa. Dynamical Calling Behavior Experimentally Observed in Japanese Tree Frogs (Hyla japonica). *IEICE Transactions on Fundamentals of Electronics, Communications and Computer Sciences*, 90(10):2154, 2007.

H. Akaike. Likelihood and the Bayesian procedure. In J.M. Bernardo, M.H. Degroot, D.V. Lindley, and A.F.M. Smith, editors, *Bayesian statistics*, pages 141–166. Valencia, Spain: University Press., 1980.

S. Amari and M. Kawanabe. Information geometry of estimating functions in semi-parametric statistical models. *Bernoulli*, 3(1):29–54, 1997.

T. Aoki and T. Aoyagi. Synchrony-induced switching behavior of spike pattern attractors created by spike-timing-dependent plasticity. *Neural computation*, 19(10):2720–2738, 2007.

T. Aonishi and K. Ota. Statistical estimation algorithm for phase response curves. *Journal of the Physical Society of Japan*, 75(11):114802, 2006.

J. Aschoff, S. Daan, and G.A. Groos. *Vertebrate circadian systems: structure and physiology*. Springer, 1982.

S.N. Baker, R. Spinks, A. Jackson, and R.N. Lemon. Synchronization in monkey motor cortex during a precision grip task. I. Task-dependent modulation in single-unit synchrony. *Journal of Neurophysiology*, 85(2):869, 2001.

A. Bartels and S. Zeki. The temporal order of binding visual attributes. *Vision research*, 46 (14):2280–2286, 2006.

S.M. Berry, R.J. Carroll, and D. Ruppert. Bayesian smoothing and regression splines for measurement error problems. *Journal of the American Statistical Association*, 97(457): 160–170, 2002.

J. Buck and E. Buck. Mechanism of rhythmic synchronous flashing of fireflies: Fireflies of southeast Asia may use anticipatory time-measuring in synchronizing their flashing. *Science*, 159(3821):1319, 1968.

G. Buzsáki. *Rhythms of the Brain*. Oxford University Press, USA, 2006.

R.J. Caroll, D. Ruppert, L. A. Stefanski, and C. M. Crainiceanu. *Measurement error in nonlinear models: A modern perspective*. Chapman and Hall, 2006.

C. Cheng and J.W.V. Ness. *Statistical regression with measurement error*. Wiley, 1999.

R.S. Chhikara and L. Folks. *The inverse Gaussian distribution: theory, methodology, and applications*. CRC, 1989.

E.A. Coddington and N. Levinson. *Theory of ordinary differential equations*. McGraw-Hill, 1955.

L.B. Cohen and B.M. Salzberg. Optical measurement of membrane potential. *Ergebnisse der Physiologie, biologischen Chemie und experimentellen Pharmakologie*, 83(-1):35–88, 1978.

J.D. Crawford. Scaling and singularities in the entrainment of globally coupled oscillators. *Physical review letters*, 74(21):4341–4344, 1995.

H. Daido. Generic scaling at the onset of macroscopic mutual entrainment in limit-cycle oscillators with uniform all-to-all coupling. *Physical review letters*, 73(5):760–763, 1994.

H. Daido. Multibranch entrainment and scaling in large populations of coupled oscillators. *Physical review letters*, 77(7):1406–1409, 1996.

S. Dano, PG Sorensen, and F. Hynne. Sustained oscillations in living cells. *Nature*, 402 (18):320–322, 1999.

P. Dayan and L.F. Abbott. *Theoretical neuroscience: Computational and mathematical modeling of neural systems*, volume 39. MIT press Cambridge, MA:, 2001.

Y. Dong, S. Mihalas, F. Qiu, R. von der Heydt, and E. Niebur. Synchrony and the binding problem in macaque visual cortex. *Journal of vision*, 8(7), 2008.

A.D. Dorval, D.J. Christini, and J.A. White. Real-time linux dynamic clamp: a fast and flexible way to construct virtual ion channels in living cells. *Annals of biomedical engineering*, 29(10):897–907, 2001.

JC Eccles. Interpretation of action potentials evoked in the cerebral cortex. *Electroencephalography and clinical neurophysiology*, 3(4):449, 1951.

B. Eckhardt, E. Ott, S.H. Strogatz, D.M. Abrams, and A. McRobie. Modeling walker synchronization on the Millennium Bridge. *Physical Review E*, 75(2):21110, 2007.

M.B. Elowitz and S. Leibler. A synthetic oscillatory network of transcriptional regulators. *Nature*, 403(6767):335–338, 2000.

A.K. Engel, P. Fries, and W. Singer. Dynamic predictions: oscillations and synchrony in top–down processing. *Nature Reviews Neuroscience*, 2(10):704–716, 2001.

J. Engel, T.A. Pedley, J. Aicardi, and M.A. Dichter. *Epilepsy: a comprehensive textbook*. Lippincott Williams & Wilkins, 2007.

G.B. Ermentrout. Type I membranes, phase resetting curves, and synchrony. *Neural computation*, 8(5):979–1001, 1996.

G.B. Ermentrout and J. Rinzel. Beyond a pacemaker's entrainment limit: phase walk-through. *American Journal of Physiology- Regulatory, Integrative and Comparative Physiology*, 246(1):102, 1984.

G.B. Ermentrout and D. Saunders. Phase resetting and coupling of noisy neural oscillators. *Journal of Computational Neuroscience*, 20(2):179–190, 2006.

G.B. Ermentrout, R.F. Galán, and N.N. Urban. Relating neural dynamics to neural coding. *Physical Review Letters*, 99(24):248103, 2007. doi: 10.1103/PhysRevLett.99.248103.

W.J. Freeman. Measurement of oscillatory responses to electrical stimulation in olfactory bulb of cat. *Journal of Neurophysiology*, 35(6):762, 1972.

W.A. Freiwald, A.K. Kreiter, and W. Singer. Synchronization and assembly formation in the visual cortex. *Progress in brain research*, 130:111–140, 2001.

P. Fries. A mechanism for cognitive dynamics: Neuronal communication through neuronal coherence. *Trends in Cognitive Sciences*, 9(10):474–480, 2005.

P. Fries, S. Neuenschwander, A.K. Engel, R. Goebel, and W. Singer. Rapid feature selective neuronal synchronization through correlated latency shifting. *Nature Neuroscience*, 4(2): 194–200, 2001.

W. A. Fuller. *Measurement error models*. Wiley–Blackwell, 2006.

R. F. Galán, G. B. Ermentrout, and N. N. Urban. Efficient estimation of phase-resetting curves in real neurons and its significance for neural-network modeling. *Phys. Rev. Lett.*, 94(15):158101, 2005.

R.F. Galán, G.B. Ermentrout, and N.N. Urban. Predicting synchronized neural assemblies from experimentally estimated phase-resetting curves. *Neurocomputing*, 69(10-12): 1112–1115, 2006.

R.F. Galán, G.B. Ermentrout, and N.N. Urban. Reliability and stochastic synchronization in type I vs. type II neural oscillators. *Neurocomputing*, 70(10-12):2102–2106, 2007a.

R.F. Galán, G.B. Ermentrout, and N.N. Urban. Stochastic dynamics of uncoupled neural oscillators: Fokker-Planck studies with the finite element method. *Physical Review E*, 76(5):56110, 2007b.

D. García-Álvarez, A. Bahraminasab, A. Stefanovska, and PVE McClintock. Competition between noise and coupling in the induction of synchronisation. *EPL (Europhysics Letters)*, 88:30005, 2009.

M.S. Gazzaniga. *The cognitive neurosciences*. The MIT Press, 2004.

A Gelman, J. B. Carlin, H. S. Stern, and D. B. Rubin, editors. *Bayesian data analysis*. Chapman & Hall, 2nd edition, 2003.

C. J. Geyer. Markov chain Monte Carlo maximum likelihood. In E.M. Keramidas, editor, *Computing science and statistics: Proceedings of 23rd symposium on the interface interface foundation*, pages 156–163. Fairfax Station, 1991.

C.J. Geyer and E.A. Thompson. Annealing Markov chain Monte Carlo with applications to ancestral inference. *Journal of the American Statistical Association*, 90(431):909–920, 1995.

W. R. Gilks, S. Richardson, and D. J. Spiegelhalter, editors. *Markov chain Monte Carlo in practice*. Chapman & Hall, 1995.

J.A. Goldberg, U. Rokni, T. Boraud, E. Vaadia, and H. Bergman. Spike synchronization in the cortex-basal ganglia networks of parkinsonian primates reflects global dynamics of the local field potentials. *Journal of Neuroscience*, 24(26):6003, 2004.

J.A. Goldberg, C.A. Deister, and C.J. Wilson. Response properties and synchronization of rhythmically firing dendritic neurons. *Journal of Neurophysiology*, 97(1):208–219, 2007.

I.J. Good. *The estimation of probabilities: An essay on modern Bayesian methods*. The MIT Press, 1965.

C.M. Gray and W. Singer. Stimulus-specific neuronal oscillations in orientation columns of cat visual cortex. *Proceedings of the National Academy of Sciences*, 86(5):1698–1702, 1989.

G. Grynkiewicz, M. Poenie, and R.Y. Tsien. A new generation of Ca2+ indicators with greatly improved fluorescence properties. *Journal of Biological Chemistry*, 260(6):3440, 1985.

J. Guckenheimer. Isochrons and phaseless sets. *Journal of Mathematical Biology*, 1(3): 259–273, 1975.

B.S. Gutkin, G.B. Ermentrout, and A.D. Reyes. Phase-response curves give the responses of neurons to transient inputs. *Journal of Neurophysiology*, 94(2):1623–1635, 2005.

D. Hansel, G. Mato, and C. Meunier. Clustering and slow switching in globally coupled phase oscillators. *Physical Review E*, 48(5):3470–3477, 1993.

D. Hansel, G. Mato, and C. Meunier. Synchrony in excitatory neural networks. *Neural Computation*, 7(2):307–337, 1995.

W.K. Hastings. Monte Carlo sampling methods using Markov chains and their applications. *Biometrika*, 57(1):97, 1970.

A.L. Hodgkin and A.F. Huxley. A quantitative description of membrane current and its application to conduction and excitation in nerve. *The Journal of physiology*, 117(4): 500, 1952.

H. Hong, H. Park, and M.Y. Choi. Collective synchronization in spatially extended systems of coupled oscillators with random frequencies. *Physical Review E*, 72(3):36217, 2005.

J.J. Hopfield and C.D. Brody. What is a moment? Transient synchrony as a collective mechanism for spatiotemporal integration. *Proceedings of the National Academy of Sciences of the United States of America*, 98(3):1282, 2001.

J.P. Huelsenbeck and F. Ronquist. MRBAYES: Bayesian inference of phylogenetic trees. *Bioinformatics*, 17(8):754–755, 2001.

K. Hukushima and K. Nemoto. Exchange Monte Carlo method and application to spin glass simulations. *Journal of the Physical Society of Japan*, 65(6):1604–1608, 1996.

Y. Iba. Extended ensemble Monte Carlo. *International Journal of Modern Physics C*, 12 (5):623–656, 2001.

T. Ichinomiya. Frequency synchronization in a random oscillator network. *Physical Review E*, 70(2):26116, 2004.

E. M. Izhikevich. *Dynamical systems in neuroscience: The geometry of excitability and bursting*. The MIT Press, 2007.

A. Jasra, D.A. Stephens, and C.C. Holmes. On population-based simulation for static inference. *Statistics and Computing*, 17(3):263–279, 2007.

I.Z. Kiss, Y. Zhai, and J.L. Hudson. Emerging coherence in a population of chemical oscillators. *Science*, 296(5573):1676, 2002.

G. Kitagawa and W. Gersch. *Smoothness priors analysis of time series*. Springer, 1996.

H. Kitahata, J. Taguchi, M. Nagayama, T. Sakurai, Y. Ikura, A. Osa, Y. Sumino, M. Tanaka, E. Yokoyama, and H. Miike. Oscillation and Synchronization in the Combustion of Candles. *J. Phys. Chem. A*, 113(29):8164–8168, 2009.

P. E. Kloeden and E. Platen. *Numerical solution of stochastic differential equations*. Springer, 3rd edition, 2000.

C. Koch and E. Schutter. *Biophysics of computation: information processing in single neurons*. Oxford University Press New York, 1999.

R. Koenker. *Quantile regression*. Cambridge Univ Pr, 2005.

N. Kopell and G.B. Ermentrout. Phase transitions and other phenomena in chains of coupled oscillators. *SIAM Journal on Applied Mathematics*, 50(4):1014–1052, 1990.

H. Kori and Y. Kuramoto. Slow switching in globally coupled oscillators: robustness and occurrence through delayed coupling. *Physical Review E*, 63(4):46214, 2001.

SW Kuffler, R. Fitzhugh, and HB Barlow. Maintained activity in the cat's retina in light and darkness. *The Journal of General Physiology*, 40(5):683, 1957.

Y. Kuramoto. Self-entrainment of a population of coupled non-linear oscillators. In *International symposium on mathematical problems in theoretical physics*, pages 420–422. Springer, 1975.

Y. Kuramoto. *Chemical oscillations, waves, and turbulence*. Springer-Verlag, 1984.

Y. Kuramoto and D. Battogtokh. Coexistence of coherence and incoherence in nonlocally coupled phase oscillators. *Arxiv preprint cond-mat/0210694*, 2002.

Y. Kuramoto and Y. Kawamura. *[in japanease]*. Baifukan, 2010.

K. Lehnertz, S. Bialonski, M.T. Horstmann, D. Krug, A. Rothkegel, M. Staniek, and T. Wagner. Synchronization phenomena in human epileptic brain networks. *Journal of Neuroscience Methods*, 183(1):42–48, 2009.

M. Lengyel, J. Kwag, O. Paulsen, and P. Dayan. Matching storage and recall: hippocampal spike timing–dependent plasticity and phase response curves. *Nature neuroscience*, 8 (12):1677–1683, 2005.

K.K. Lin, E. Shea-Brown, and L.S. Young. Reliability of coupled oscillators. *Journal of Nonlinear Science*, 19(5):497–545, 2009.

D. J. C. MacKay. *Information theory, inference and learning algorithms*. Cambridge University Press, 2003.

D.J.C. MacKay. Bayesian interpolation. *Neural computation*, 4(3):415–447, 1992.

Z. F. Mainen and T. J. Sejnowski. Reliability of spike timing in neocortical neurons. *Science*, 268(5216):1503–1506, 1995.

I.G. Malkin. The Methods of Lyapunov and Poincare in the Theory of Nonlinear Oscillations. *Gostekhizdat, Moscow-Leningrad*, 1949.

I.G. Malkin. *Some problems in the theory of nonlinear oscillations*. US Atomic Energy Commission, Technical Information Service, 1959.

C. Malsburg and W. Schneider. A neural cocktail-party processor. *Biological Cybernetics*, 54(1):29–40, 1986.

J.G. Mancilla, T.J. Lewis, D.J. Pinto, J. Rinzel, and B.W. Connors. Synchronization of electrically coupled pairs of inhibitory interneurons in neocortex. *Journal of Neuroscience*, 27(8):2058, 2007.

S. Marella and G.B. Ermentrout. Class-II neurons display a higher degree of stochastic synchronization than class-I neurons. *Physical Review E*, 77(4):41918, 2008.

H. Markram. The blue brain project. *Nature Reviews Neuroscience*, 7(2):153–160, 2006.

N. Metropolis, A.W. Rosenbluth, M.N. Rosenbluth, A.H. Teller, E. Teller, et al. Equation of state calculations by fast computing machines. *The journal of chemical physics*, 21 (6):1087, 1953.

A.S. Mikhailov and K. Showalter. Control of waves, patterns and turbulence in chemical systems. *Physics Reports*, 425(2-3):79–194, 2006.

C. Morris and H. Lecar. Voltage oscillations in the barnacle giant muscle fiber. *Biophysical Journal*, 35(1):193–213, 1981.

K. Nakae. Stastical estimation of phase response curves with consideration of fluctuations of periods [in japanease]. Master's thesis, Kyoto University, 2008.

K. Nakae, Y. Iba, Y. Tsubo, T. Fukai, and T. Aoyagi. Bayesian estimation of phase response curves. *Neural Networks*, 23(6):752–763, 2010.

T.I. Netoff, C.D. Acker, J.C. Bettencourt, and J.A. White. Beyond two-cell networks: experimental measurement of neuronal responses to multiple synaptic inputs. *Journal of Computational Neuroscience*, 18(3):287–295, 2005a.

T.I. Netoff, M.I. Banks, A.D. Dorval, C.D. Acker, J.S. Haas, N. Kopell, and J.A. White. Synchronization in hybrid neuronal networks of the hippocampal formation. *J. Neurophysiol.*, 93(3):1197–1208, 2005b.

M.A.L. Nicolelis, C.R. Stambaugh, A. Brisben, and M. Laubach. Methods for simultaneous multisite neural ensemble recordings in behaving primates. *Methods for Neural Ensemble Recordings*, 7:121–56, 1999.

M. Nomura and T. Aoyagi. Stability of Synchronous Solutions in Weakly Coupled Neuron Networks. *Progress of Theoretical Physics*, 113(5), 2005.

SA Oprisan, V. Thirumalai, and CC Canavier. Dynamics from a time series: can we extract the phase resetting curve from a time series? *Biophysical journal*, 84(5):2919–2928, 2003.

SA Oprisan, AA Prinz, and CC Canavier. Phase resetting and phase locking in hybrid circuits of one model and one biological neuron. *Biophysical journal*, 87(4):2283–2298, 2004.

K. Ota. *Statistical estimation for phase response curves based on Bayesian theory and derivation of feature space in rat hippocampal CA1 pyramidal neurons [in japanease*. PhD thesis, Tokyo Institute of Technology, 2010.

K. Ota, M. Nomura, and T. Aoyagi. A weighted spike-triggered average of a fluctuating stimulus yielding the phase response curve. *Physical Review Letters*, 103(2):024101, 2009a.

K. Ota, T. Omori, and T. Aonishi. MAP estimation algorithm for phase response curves based on analysis of the observation process. *Journal of Computational Neuroscience*, 26(2):1–18, 2009b.

J. Pantaleone. Synchronization of metronomes. *American Journal of Physics*, 70:992, 2002.

E. Parzen. On estimation of a probability density function and mode. *The annals of mathematical statistics*, 33(3):1065–1076, 1962.

E. Phoka, H. Cuntz, A. Roth, and M. Häusser. A New Approach for Determining Phase Response Curves Reveals that Purkinje Cells Can Act as Perfect Integrators. *PLoS Computational Biology*, 6(4):665–678, 2010.

A. Pikovsky, M. Rosenblum, J. Kurths, and R.C. Hilborn. Synchronization: A universal concept in nonlinear science. *American Journal of Physics*, 70:655, 2002.

W.H. Press, B.P. Flannery, S.A. Teukolsky, W.T. Vetterling, et al. *Numerical recipes*. Cambridge university press Cambridge, 2007.

A.J. Preyer and R.J. Butera. Neuronal oscillators in aplysia californica that demonstrate weak coupling in vitro. *Physical Review Letters*, 95(13):138103, 2005.

R. Reemtsen and J. Rueckmann, editors. *Human physilogy*. Springer, 1983.

A. Revonsuo and J. Newman. Binding and consciousness. *Consciousness and Cognition*, 8(2):123, 1999.

A.D. Reyes and E.E. Fetz. Effects of transient depolarizing potentials on the firing rate of cat neocortical neurons. *Journal of neurophysiology*, 69(5):1673, 1993a.

A.D. Reyes and E.E. Fetz. Two modes of interspike interval shortening by brief transient depolarizations in cat neocortical neurons. *Journal of neurophysiology*, 69(5):1661, 1993b.

A. Riehle, S. Grun, M. Diesmann, and A. Aertsen. Spike synchronization and rate modulation differentially involved in motor cortical function. *Science*, 278(5345):1950, 1997.

F. Rieke and D. Warland. *Spikes: exploring the neural code*. The MIT Press, 1999.

C. P. Robert and G. Casella. *Monte Carlo statistical methods*. Springer, 2nd edition, 2004.

S.A. Roy, S.P. Dear, and K.D. Alloway. Long-range cortical synchronization without concomitant oscillations in the somatosensory system of anesthetized cats. *Journal of Neuroscience*, 21(5):1795, 2001.

H. Sakaguchi, S. Shinomoto, and Y. Kuramoto. Local and global self-entrainments in oscillator lattices. *Prog. Theor. Phys*, 77(5):1005–1010, 1987.

E. Salinas and T.J. Sejnowski. Correlated neuronal activity and the flow of neural information. *Nature Reviews Neuroscience*, 2(8):539–550, 2001.

N.E. Schoppa. Synchronization of olfactory bulb mitral cells by precisely timed inhibitory inputs. *Neuron*, 49(2):271–283, 2006.

T. Shimokawa and S. Shinomoto. Estimating instantaneous irregularity of neuronal firing. *Neural computation*, 21(7):1931–1951, 2009.

B.W. Silverman. *Density estimation for statistics and data analysis*. Chapman & Hall/CRC, 1998.

J. Simonet, M. Warden, and E. Brun. Locking and Arnold tongues in an infinite-dimensional system: The nuclear magnetic resonance laser with delayed feedback. *Physical Review E*, 50(5):3383–3391, 1994.

W. Singer. Striving for coherence. *Nature*, 397(4):391–393, 1999.

H.M. Smith. Synchronous flashing of fireflies. *Science*, 82:151–152, 1935.

P. N. Steinmetz, A. Roy, P. J. Fitzgerald, S. S. Hsiao, K. O. Johnson, and E. Niebur. Attention modulates synchronized neuronal firing in primate somatosensory cortex. *Nature*, 404(6774):187–190, 2000.

C. Stosiek, O. Garaschuk, K. Holthoff, and A. Konnerth. In vivo two-photon calcium imaging of neuronal networks. *Proceedings of the National Academy of Sciences of the United States of America*, 100(12):7319, 2003.

S. H. Strogatz. *Sync: How order emerges from chaos in the universe, nature, and daily life*. Hyperion, 4 2004.

S.H. Strogatz. From Kuramoto to Crawford: exploring the onset of synchronization in populations of coupled oscillators. *Physica D: Nonlinear Phenomena*, 143(1-4):1–20, 2000.

S.H. Strogatz and R.E. Mirollo. Stability of incoherence in a population of coupled oscillators. *Journal of Statistical Physics*, 63(3):613–635, 1991.

S.H. Strogatz, D.M. Abrams, A. McRobie, B. Eckhardt, and E. Ott. Theoretical mechanics: Crowd synchrony on the Millennium Bridge. *Nature*, 438(7064):43–44, 2005.

M. Taketani, M. Baudry, and Inc NetLibrary. *Advances in network electrophysiology: using multi-electrode arrays*. Springer, 2006.

T. Tanabe and T. Tanaka. [in Japnaease]. *Gekkan Chikyu*, 5(3):179–186, 1983.

T. Tateno and HPC Robinson. Phase resetting curves and oscillatory stability in interneurons of rat somatosensory cortex. *Biophysical journal*, 92(2):683–695, 2007.

J. Teramae and T. Fukai. Temporal precision of spike response to fluctuating input in pulse-coupled networks of oscillating neurons. *Physical review letters*, 101(24):248105, 2008.

A. Thiele and G. Stoner. Neuronal synchrony does not correlate with motion coherence in cortical area MT. *Nature*, 421(6921):366–370, 2003.

C. A Thomas et al. A miniature microelectrode array to monitor the bioelectric activity of cultured cells. *Experimental cell research*, 74(1):61–66, 1972.

D. M. Titterington. Common structure of smoothing techniques in statistics. *International Statistical Review/Revue Internationale de Statistique*, 53(2):141–170, 1985.

R. Toth, A.F. Taylor, and M.R. Tinsley. Collective behavior of a population of chemically coupled oscillators. *J. Phys. Chem. B*, 110(20):10170–10176, 2006.

Y. Tsubo, M. Takada, A.D. Reyes, and T. Fukai. Layer and frequency dependencies of phase response properties of pyramidal neurons in rat motor cortex. *European Journal of Neuroscience*, 25(11):3429–3441, 2007a.

Y. Tsubo, J. Teramae, and T. Fukai. Synchronization of excitatory neurons with strongly heterogeneous phase responses. *Physical review letters*, 99(22):228101, 2007b.

H.C. Tuckwell. *Introduction to theoretical neurobiology: Linear cable theory and dendritic structure*. Cambridge Univ Pr, 1988.

J.W. Tukey. *Exploratory data analysis*. Addison-Wesley, 1977.

F. Varela, J.P. Lachaux, E. Rodriguez, and J. Martinerie. The brainweb: Phase synchronization and large-scale integration. *Nature Reviews Neuroscience*, 2(4):229–239, 2001.

C. Vreeswijk, LF Abbott, and G. Bard Ermentrout. When inhibition not excitation synchronizes neural firing. *Journal of Computational Neuroscience*, 1(4):313–321, 1994.

G. Wahba. *Spline models for observational data*. Society for Industrial Mathematics, 1990.

T.J. Walker. Acoustic synchrony: two mechanisms in the snowy tree cricket. *Science*, 166 (3907):891–894, 1969.

K. Whittingstall and N.K. Logothetis. Frequency-band coupling in surface EEG reflects spiking activity in monkey visual cortex. *Neuron*, 64(2):281–289, 2009.

K. Wiesenfeld, P. Colet, and S.H. Strogatz. Synchronization transitions in a disordered Josephson series array. *Physical review letters*, 76(3):404–407, 1996.

A. T. Winfree. *The geometry of biological time*. Springer, 2001.

A.T. Winfree. Biological rhythms and the behavior of populations of coupled oscillators. *Journal of theoretical biology*, 16(1):15–42, 1967.

Y. Zhai, I.Z. Kiss, and J.L. Hudson. Amplitude death through a Hopf bifurcation in coupled electrochemical oscillators: Experiments and simulations. *Physical Review E*, 69(2): 26208, 2004.

M. Zochowski, M. Wachowiak, C.X. Falk, L.B. Cohen, Y.W. Lam, S. Antic, and D. Zecevic. Imaging membrane potential with voltage-sensitive dyes. *The Biological Bulletin*, 198(1):1, 2000.